Alpha Particle Energetics and Neutral Beam Heating in Tokamak Plasmas

David G. McAlees

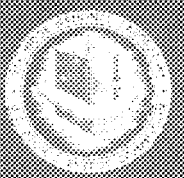

OAK RIDGE NATIONAL LABORATORY
OPERATED BY UNION CARBIDE CORPORATION • FOR THE U.S. ATOMIC ENERGY COMMISSION

ORNL-TM-4661

Contract No. W-7405-eng-26

Thermonuclear Division

ALPHA PARTICLE ENERGETICS AND NEUTRAL BEAM HEATING IN TOKAMAK PLASMAS

David G. McAlees

Submitted as a dissertation to the Graduate School of
The University of Wisconsin in partial fulfillment of
the requirements for the degree of Doctor of Philosophy
in Nuclear Engineering

NOVEMBER 1974

OAK RIDGE NATIONAL LABORATORY
Oak Ridge, Tennessee 37830
operated by
UNION CARBIDE CORPORATION
for the
U.S. ATOMIC ENERGY COMMISSION

TABLE OF CONTENTS

TABLE OF CONTENTS (Continued)

ABSTRACT

ALPHA PARTICLE ENERGETICS AND NEUTRAL BEAM HEATING

IN TOKAMAK PLASMAS

David George McAlees

Under the Supervision of Professor H. K. Forsen

In this work two key physics areas fundamental to tokamak plasmas have been analyzed in detail. Both center around plasma and particle dynamics and are critical to the success of deuterium-tritium fueled fusion power systems as they are presently envisioned.

The energetic aspects of the 3.5 MeV alpha particles produced in D-T fusion events are examined and physical phenomena which can be expected to occur in future devices containing alphas are predicted. The model of the alpha particle dynamics includes toroidal magnetic field gradient and curvature drifts and motion along the magnetic field lines. Guiding center motion of alpha particles in various size plasma systems is analyzed. It is shown that finite gyro-radius effects play a basic role in determining alpha particle behavior for feasibility size plasmas (I = 2-5 MA). The alpha particle containment properties for feasibility and reactor size devices are computed. For devices with $I > 2$ MA, greater than 75 percent of the alpha particles produced in the plasma are contained, i.e., are on orbits which do not intersect the plasma boundary. From a plasma heating point of view, such containment is acceptable.

Fast alpha particle distribution functions for the contained alphas are calculated by integrating the source function along the appropriate orbit characteristics numerically. The alpha particle

energy density deposition rate profiles, momentum input profiles and the magnitude of electrostatic charging in the background plasma due to alpha particle losses, are determined using the distribution functions constructed. Relative to the resulting heating profiles, in lower current devices ($I \approx 2$ MA) the profile is broadened radially and reduced in magnitude compared to the alpha production profile. These results are due to large orbit excursions and particle losses from the system. These effects are found to diminish for larger values of plasma current so that for $I \geq 10$ MA the heating and production profiles can be assumed equal to a high degree of accuracy.

Potentially deleterious effects including toroidal flow velocity inhomogeneities induced by the momentum input of the alpha particles, plasma rotation, and electrostatic charging of the background plasma due to alpha particle losses are examined.

It is concluded that the energetic effects of alpha particles present no apparent problems for reactor size ($I \geq 10$ MA) plasmas. In feasibility size devices ($I = 2$-5 MA), electrostatic charging in the background plasma requires further self-consistent consideration.

A model is developed to determine the energy density deposition rate profiles for neutral beam injection into a tokamak. The heating profiles in the background plasma due to neutral beam injection and alpha particle production are coupled to study the startup of a large CTR reactor. A two-fluid space time computer model is used to simulate the overall plasma behavior. The simulation model includes neoclassical ion conduction, pseudoclassical electron conduction, electron-ion rethermalization, bremsstrahlung and synchrotron radiation, ohmic

heating, alpha particle and neutral beam heating terms. Questions of beam energy deposition profiles, energy requirements for neutral penetration into the plasma, and beam power required to achieve ignition or prescribed heatup rates are examined. The analysis is primarily for the 5000 MW(th) conceptual fusion reactor UWMAK-I studied by the University of Wisconsin. Typically, beam energies of several hundred kilovolts and powers of $\sim$ 50 MW provide adequate penetration and ignition times in the range of 2 to 10 seconds. The sensitivities of the time required to achieve ignition and resulting heatup rates to changes in injection energy (100 to 500 keV) and beam power (10 to 75 MW) are also determined.

ACKNOWLEDGMENTS

Foremost the author expresses his sincere gratitude to Professor H. K. Forsen who first introduced him to the thermonuclear field and whose continuing encouragement, enthusiasm and advice have been invaluable.

The support of the faculty members of the Nuclear Engineering Department of the University of Wisconsin is gratefully acknowledged. In particular, Professor R. W. Conn provided insight and suggestions which were fundamental to this work.

Participation of many members of the Thermonuclear Division of the Oak Ridge National Laboratory is acknowledged. Specifically, discussions with Drs. J. D. Callen , C. L. Hedrick, J. T. Hogan and J. A. Rome were extremely useful.

The interest and patience of my wife, Penelope, were helpful and deeply appreciated throughout the course of this research.

It was a pleasure to have the assistance of Mrs. Caila Cox in coordinating the preparation of the thesis.

This research was supported by the Wisconsin Electric Utilities Research Foundation and performed at the Oak Ridge National Laboratory where computer costs and other support functions were funded by the U. S. Atomic Energy Commission under contract with Union Carbide Corporation.

LIST OF FIGURES

LIST OF FIGURES (Continued)

I. INTRODUCTION

Many problems will be encountered in the process of developing present day plasma confinement devices into future fusion power systems. For example, relative to toroidally confined plasmas, neutral beam heating techniques are in the early stage of investigation and will continuously demand technological advances as power and energy level requirements increase. Larger plasma currents and higher magnetic fields will require auxiliary systems capable of handling enormous amounts of energy. Radioactive systems and structure also will place new demands on remote maintenance methods, accessibility requirements and shielding considerations. In addition, fundamental uncertainties in several areas including the plasma physics details of reactor type plasmas suggest that unforeseen problems will arise.

The need for a series of experiments which will provide the relevant information along the path to a power reactor is clear. Also, theoretical analyses and conceptual designs of all aspects of future systems are needed to uncover problems a priori and allow some of them to be circumvented by timely innovative design efforts.

In this work an attempt has been made to anticipate two key physics areas fundamental to tokamak plasmas and to analyze them in detail. Both center around plasma and particle dynamics and both are critical to the eventual success of deuterium-tritium (D-T) fueled fusion power systems as they are presently envisioned.

A fission system becomes self-sustaining or critical when a particle balance between neutron sources and losses is attained. The equivalent self-sustaining condition in a fusion system is defined from an

energetic point of view. This concept of ignition is developed in detail later but essentially ignition refers to an instantaneous balance between the energy delivered to the plasma as a result of fusion events and the energy lost from the plasma by all loss mechanisms. In the case of a magnetically confined D-T plasma, the energy input into the plasma due to fusion can come only from the $\sim$ 3.5 MeV alpha particle produced since the 14.1 MeV neutron is not confined. Existing experiments do not operate in the regime where the alpha particle component of the plasma is present. Such operation is the goal of future devices. Thus, it is of interest to analyze the energetic aspects of alpha particle behavior and predict what physical phenomena can be expected to occur in future devices containing alpha particles. To do so the effort here has been focused on a particular alpha particle model. The dynamic model reflects the necessary orbit details to permit a determination of the distribution function of fast alpha particles resulting from a given radially dependent source rate. From the fast alpha distribution function, estimates of the density of fast alpha particles, their radially dependent energy deposition rate profiles, specific momentum profiles (both on a flux surface and averaged over a flux surface) and the magnitude of electrostatic charging in the plasma are made. Some of these results are manifestations of finite gyro-radius effects which are included in the analyses. Potentially deleterious effects of alpha particles on the background plasma in a feasibility size device (plasma current between 2-5 MA) are suggested. It can be concluded that, generally, alpha particles and their associated effects should present no problems in reactor size ($I \geqslant 10$ MA) devices.

In order to achieve ignition, a supplemental means of heating the plasma is necessary since ohmic heating alone is insufficient. The prospect of heating toroidally confined plasmas by energetic neutral beam injection has stimulated much interest and optimism in this technique. Predictions for present day experiments[1-4] lend support to the optimism. Although the tokamak injection experimental program is still in an early stage, recent results from ATC,[5] CLEO,[6] and ORMAK[7] devices indicate progress in beam heating techniques and show no apparent adverse effects on plasma confinement. Further, technological developments toward higher energy and power neutral beam systems are anticipated in support of next generation experiments.[8,9]

To assess the feasibility of developing large, power producing plasmas which are heated by neutral beam injection, the energy and power requirements have been determined for compatible neutral beam injection systems. Questions of beam energy deposition profiles, beam energies needed to obtain adequate neutral penetration into the plasma and power requirements to achieve ignition or prescribed plasma heatup rates, are examined. The analysis is primarily for the 5000 MW (th) conceptual fusion reactor system recently studied by the University of Wisconsin.[10] However, the results are generally applicable to toroidal systems and, wherever possible, the implications of the results for other, in particular, smaller size plasmas are indicated.

The work which follows then centers around alpha particle dynamics and their implications on both feasibility and reactor size plasmas and the response of toroidally confined plasmas to neutral beam injection during the ignition phase of startup. In both cases the model used in

the analysis is first developed, then the details of the analysis itself and, finally, the results and conclusions.

II. CHARGED PARTICLE ORBIT MODEL

A. Model Development

The model developed to describe the motion of charged particles in a toroidal device must satisfy two guidelines. First, it must be fundamental so as to retain the essential features of the orbit physics such as trapped particles, dominant drift motions and so on. In addition, however, it must be simplified so as to permit many single particle orbit calculations to be used efficiently to construct results in the form of distribution functions. Integration of the basic equations of motion for single particles would be prohibitive.

The geometry referred to throughout this paper is shown on Fig. 1. The quasi-toroidal coordinates (r,θ,ϕ), the major radius (R), and the local cartesian coordinates (x,y), taken in a ϕ = constant plane, are all used below. Definite directions for the toroidal magnetic field (B_ϕ), plasma current density (J), and as a consequence the poloidal magnetic field (B_θ) are assumed. Since the physical results are independent of the direction of these quantities, they are directed as shown on Fig. 2 to facilitate later discussions. Thus, "costreaming" always refers to particles following drift orbits away from the reader as shown on Fig. 2 such that $\vec{v}_{||} \cdot \vec{J} > 0$ in general. Also, drift motion due to the toroidal gradient and curvature is in the +y direction and field lines rotate clockwise when the observer moves in the same direction as the plasma current.

Guiding center orbit equations are used throughout to compute particle motion. For alpha particles, due to their mass and high velocity,

gyro-radii of several centimeters are typical for field strengths of about 50 kG as anticipated. However, since devices containing alphas also typically are visualized to have scale lengths on the order of meters, the guiding center approximation is adequate as will be shown below.

The toroidal system is assumed to be axisymmetric relative to the vertical central axis. Thus, the guiding center equations of motion are cyclic in the toroidal coordinate (ϕ) and the canonical angular momentum (p_ϕ) in this direction is conserved.[11] Further, the analysis is restricted to monoenergetic alpha particles (3.5 MeV) and spatial orbit effects are taken into detailed account. The interest here is to determine the characteristics of the fast alpha particle species which will be present in all devices that burn deuterium fuel. Also, from a heat input point of view, the containment properties for fast alpha particles are of foremost importance. That is, the time scale of interest is

$$\tau_b < t < \tau_f \quad ,$$

where τ_b is the bounce time required for a particle to execute one bounce orbit and τ_f is the slowing down time. (It is shown in a later chapter that the time scale restrictions are of little consequence in reactor size devices.)

The adiabatic invariant,

$$\mu = \frac{1}{2} m v_\perp^2 / B \quad ,$$

is also a constant of the alpha particle motion. Since only static magnetic fields are considered, the criterion for conservation of μ is that,

$$\frac{\Delta B}{B} \ll 1$$

during one gyro-orbit. For a 3.5 MeV alpha particle, the gyro-frequency is

$$\omega_c = 2.4 \times 10^8 \left(\frac{B}{50}\right) \frac{\text{rad.}}{\text{sec.}} \quad , \qquad (B \text{ in kG})$$

so that in the case of $v_\perp \gg v_\parallel$ the gyro-radius is

$$\rho = 5.4 \left(\frac{50}{B}\right) \text{cm.}$$

Taking the toroidal field approximately equal to the total magnetic field

$$B = \frac{B_0 R_0}{R}$$

and

$$\frac{\Delta B}{B} = \frac{\Delta R}{R} \approx \frac{2\rho}{R}$$

as the particle orbits in the gradient of the toroidal field. For typical parameters it is assumed that $B \sim 50$ kG and that $R \sim 4$ m. Then

$$\frac{\Delta B}{B} \approx \frac{1}{40} \ll 1 \quad .$$

The other case, $v_\parallel \gg v_\perp$, must also be considered since in the frame of reference of the particle a different ΔB occurs during a gyro-orbit due to particle motion in the magnetic field gradient.[12] In one gyro-period a 3.5 MeV alpha particle moves a distance $\Delta s \approx 34$ cm along a field line. Conservatively it is assumed that $q = 1$ in order to

consider the case of maximum rotational transform. In this case the corresponding excursion in the direction defined by the gradient is approximately

$$\Delta R \approx \frac{\Delta s}{2\pi R} (2\pi r)$$

and

$$\frac{\Delta B}{B} \approx \frac{\Delta s}{RA} \quad .$$

For an aspect ratio A = 3 and the parameters assumed above,

$$\frac{\Delta B}{B} \approx \frac{1}{36} \ll 1 \quad .$$

Under the assumptions of toroidal axisymmetry, a collisionless time scale and device sizes typical of those expected to contain alpha particles, the adiabatic invariant, (μ), the alpha particle energy, (E_α), and the toroidal component of canonical angular momentum, (p_ϕ), are constants of the motion. The orbit equation can be obtained from these constants.

From the definition of the toroidal component of angular momentum,

$$p_\phi = (ze)\ RA_\phi + mv_\phi R \quad . \qquad (1)$$

The poloidal flux function can be defined as

$$\psi = -\ RA_\phi \ .$$

Also,

$$v_\phi = + \frac{v_\parallel B_\phi}{B} = \frac{v_\parallel}{[1 + B_\theta^2/B_\phi^2]^{1/2}}$$

$$\approx + v_\parallel \left[1 - 1/2q^2A^2\right]$$

and thus in the usual cases where $q > 1$ and $A \geq 3$,

$$v_\phi \approx + v_\parallel \ .$$

Similarly,

$$B \approx B_\phi \ .$$

The following form of the orbit equation results,

$$p_\phi = ze\psi(r) + mv_\parallel R \ .$$

It is important to note here that $\psi(r)$ is assumed to be a function of minor radius only. This is equivalent to assuming circular, concentric flux surfaces. Actual flux surface shape determination from equilibrium considerations is somewhat of an art and depends on an assumed pressure profile, current profile and system boundary conditions.[13] To lowest order in the expansion parameter r/R, Shafranov[14] has shown that circular flux surfaces result and

$$\Delta(r) = \frac{C_1 r^2}{2R}$$

for the case of a parabolic pressure profile and approximately uniform current density. C_1 is a constant and Δ is the displacement between the flux surface centers and the cross section center. By assuming that the flux surfaces are concentric, a displacement of order $r^2/2R$ is neglected. The alpha particle containment results discussed below show that the assumption of a uniform current density is conservative in the sense that containment properties improve with more peaked current distributions. The flat profile shape is used here due to the uncertainty in the current profile to be anticipated for future devices.

The simple magnetic field configuration,[15]

$$B_r = 0$$

$$B_\theta = \beta(r)\,\frac{R_0}{R} \approx \frac{\mu_0 J r}{2}\left(\frac{R_0}{R}\right)$$

$$B_\phi = B_{\phi_0}\,\frac{R_0}{R} \quad ,$$

results in the desired magnetic surface configuration. In this formulation the current density is uniform to zeroth order in the parameter r/R. Since

$$\psi = \int B_\theta R\, dr$$

$$\psi(r) = \int_0^r \left(\frac{\mu_0 J\, r'}{2}\right)\frac{R_0}{R}\, R\, dr'$$

it follows that

$$\psi(r) = \left(\frac{\mu_0 J\, R_0}{4}\right) r^2 \quad .$$

Combining these terms with signs consistent with directions shown on Fig. 2, the orbit equation obtained is

$$(ze) \cdot \left(\frac{\mu_0 J\, R_0}{4}\right) r^2 \mp m v_{\|} R = p_\phi \qquad (2)$$

where the minus sign is taken when $\vec{v}_{\|} \cdot \vec{J} > 0$.

To illustrate clearly the orbit model implicit in this equation, consider an alternate derivation. In terms of the local cartesian coordinates (x,y), the dominant guiding center drift motion is due to the toroidal magnetic field gradient and curvature,[16,17] i.e.,

$$v_y = \frac{m}{(ze)BR}\left(v_{\|}^2 + v_{\perp}^2/2\right) \quad . \qquad (3)$$

Due to the particle motion along a field line, there are two additional velocities in the x-y reference frame given by

$$v_y = - v_{\|}\left(\frac{B_\theta}{B_\phi}\right)\text{Cos }\theta \approx - v_{\|}\left(\frac{\mu_0 J\ r}{2}\right)\frac{1}{B_{\phi_0}}\left(\frac{x}{r}\right) \tag{4}$$

$$v_x = v_{\|}\left(\frac{B_\theta}{B_\phi}\right)\text{Sin }\theta \approx + v_{\|}\left(\frac{\mu_0 J\ r}{2}\right)\frac{1}{B_{\phi_0}}\left(\frac{y}{r}\right). \tag{5}$$

Assuming $B \approx B_\phi$ and combining equations (3), (4) and (5) yields

$$\frac{(dy/dt)}{(dx/dt)} = \frac{\frac{m}{(ze)B_{\phi_0}R_0}\left(v_{\|}^2 + \frac{v_\perp^2}{2}\right) - v_{\|}\left(\frac{\mu_0 J\ r}{2}\right)\frac{1}{B_{\phi_0}}\left(\frac{x}{r}\right)}{v_{\|}\left(\frac{\mu_0 J\ r}{2}\right)\frac{1}{B_{\phi_0}}\left(\frac{y}{r}\right)}$$

$$ydy + xdx = \frac{2m}{(ze)R_0\mu_0 J}\ \frac{v_{\|}^2 + v_\perp^2/2}{v_{\|}}\ dx\ .$$

Using the definitions,

$$v_{\|}^2 = \frac{2}{m}\ (E - \mu B_\phi)$$

$$v_\perp^2 = \frac{2}{m}\ (\mu B_\phi)$$

results in

$$(ze)\ \frac{\mu_0 J\ R_0}{4m}\ r^2 = \left(\frac{2}{m}\right)^{1/2} \int \frac{E - 1/2\ \mu B_\phi}{\sqrt{E - \mu B_\phi}}\ dx\ .$$

Note

$$\frac{d}{dx}\left[R\sqrt{E - \mu B_\phi}\right] = \sqrt{E - \mu B_\phi} + \frac{R}{2}\frac{\mu}{\sqrt{E - \mu B_\phi}}\left(-\frac{dB_\phi}{dx}\right)$$

$$= \frac{E - 1/2\ \mu B_\phi}{\sqrt{E - \mu B_\phi}}\ .$$

The integrand is a perfect differential and the final form of the orbit equation is obtained as

$$(ze)\left(\frac{\mu_0 J\ R_0}{4}\right) r^2 \mp m v_{\|} R = p_\phi \tag{6}$$

as before. Again the minus sign is taken when $\vec{v}_{\|} \cdot \vec{J} > 0$. Also, the constant of integration has been written as p_ϕ.

The physics of both derivations are the same in that the spatial expression of p_ϕ conservation is the first integral of the guiding center motion equations. The motivation for this exercise was to demonstrate that the orbits, under the present assumptions, result from two distinct motions. First, the guiding center motion due to the toroidal magnetic field gradient and curvature drifts and second, motion along a field line. This physical interpretation of the particle motion will be useful in understanding the orbit effects described below.

The constant p_ϕ depends on the initial conditions of the specific particle orbit being computed. The initial pitch angle, χ, is defined as the angle between the particle velocity vector $\vec{v}$ and the magnetic field vector $\vec{B}$. With the initial spatial conditions denoted by subscript B, lengths normalized to the plasma radius a, and C a constant, Equation (6) can be written as

$$r^2 \mp P[(x - x_T)(x + A)]^{1/2} = C \tag{7}$$

where

$$x_T = x_B - (x_B + A)\ \mathrm{Cos}^2\ \chi \tag{8}$$

$$P = \frac{2qv}{\Omega a} \tag{9}$$

$$\Omega = \frac{zeB_{\phi_0}}{m} \quad . \tag{10}$$

The sign choice as before distinguishes between particles which are initially costreaming ($\vec{v}_{||} \cdot \vec{J} > 0$) versus counterstreaming. Thus, $\chi \leq \pi/2$ always. x_T is computed from the initial conditions and determines the maximum penetration into the magnetic field gradient possible for a given particle. At $x = x_T$, $v_{||} = 0$ and the particle is on a trapped or banana orbit.

As an example, consider a costreaming particle initially at $x_B = 0.5$, $y_B = 0.0$ with initial pitch angle $\chi = 0$. For A = 4, Equation (7) yields

$$(x - P/2)^2 + y^2 = (0.5 - P/2)^2 \quad ,$$

which describes a circular orbit with the center of the circle at $x = P/2$. The flux surface corresponding to the initial position of the particle is given by r = 0.5 and is a circle centered at r = 0.0. The shift between the centers of the circles demonstrates the important difference between a flux surface and a particle drift surface. In the special case

$$\underset{P \to 0}{\text{Limit}} \quad \delta = 0 \quad ,$$

that is, the deviation between a particle orbit and its corresponding flux surface diminishes as P goes to zero. Since P may also be written as[18]

$$P = \frac{\rho_\theta}{a}\,\frac{2}{A} = \frac{2}{A} \cdot \frac{\text{gyro-radius in the poloidal field}}{\text{plasma radius}} \quad ,$$

cases where the parameter P approaches zero are equivalent to cases where the poloidal gyro-radius of the particle approaches zero. Small gyro-radius expansions are popular with plasma theorists and it is well known that in such cases particle deviations from their initial flux surfaces are small. However, except in reactor size, high current devices, typical alpha particle gyro-radii are larger than acceptable in the expansion procedure and here the more general orbit equation is used. The unusual alpha particle trapping characteristics discussed below are also a consequence of the large gyro-radii conditions.

One further comment should be made on the parameter P. From Equation (7), it is apparent that the orbit characteristics of a particle depend on its initial conditions, P and A. This suggests that the behavior of alpha particles in a reactor size device can be simulated in a smaller machine with the same aspect ratio using injected protons if

$$P_\alpha = P_{EXP}$$

where

$$P_\alpha = \frac{2qv}{\Omega a} = \frac{2.7}{IA} \quad (I \text{ in MA})$$

$$P_{EXP} = \frac{2qv}{\Omega a} = \frac{0.045\sqrt{T}}{IA} \quad (T \text{ in keV})$$

and T is the energy of the proton used in the simulation. Assuming the protons are to be injected into the device as neutrals, the required injection energy is given by

$$T = \left[\left(\frac{I}{.045}\right)_{EXP} \cdot \left(\frac{2.7}{I}\right)_\alpha\right]^2 \text{ keV} \quad .$$

Therefore, the orbits of 3.5 MeV alpha particles in a device with a

plasma current of 10 MA can be simulated by injecting 36 keV hydrogen atoms into a device with a 1 MA current. There seems to be agreement that single particle orbit simulation in this way is viable. However, in the case of thermonuclear produced alpha particle simulation, the importance of synergistic effects, the inability to model the isotropic velocity space distribution and spatial profiles with a finite number of injection units and other considerations have led to varied opinions as to the adequacy of the simulation technique.[19,20]

B. Alpha Particle Orbit Characteristics

Recall that the directions of B_ϕ, J and B_θ are as shown on Fig. 2. To describe the single particle orbit characteristics typical of alpha particles in a tokamak field, a device with I = 5 MA, A = 4, x_B = 0.5 and y_B = 0.0 is considered. It is assumed that in the D-T fusion reaction, the alpha particles are produced isotropically in velocity space. Here specific pitch angles for both costreaming and counterstreaming particles are chosen to illustrate orbit details of interest. The reason for the pitch angles used will become clear later.

Figure 3 shows the orbits for costreaming alpha particles produced under the conditions outlined above and initial pitch angles such that Cos χ = 1.0, 0.6, 0.37, 0.2, 0.07, 0.02 and 0.0. Due to the directions of B_ϕ and B_θ chosen, particles which closely follow their initial flux surface rotate in a clockwise direction as visualized in the cross-section view of Fig. 3. This is the case for orbit (a) and orbit (b) shown on the figure. The orbits are symmetric about the horizontal axis and the orbit in the lower half of the cross section only is shown for clarity. Recall also that the toroidal drift, although a small effect

on orbits (a) and (b), is in the +y or upward direction and causes the particles to drift to the inside of their initial flux surface.

The next two orbits shown, (c) and (d), are trapped particle orbits. The corresponding initial pitch angles are Cos χ = 0.37 and 0.2, respectively. Since the initial pitch angles are successively larger than those for the first two orbits described, the upward drift component of the motion causes larger deviations from the particles' initial flux surface. Motion along a field line is proportional to $v_{||}$ so that on an orbit where $v_{||} \approx 0$ the drift motion becomes dominant so that the particles are virtually on a vertical trajectory. In the region where $v_{||} \approx 0$, the drift velocity

$$v_y \approx \frac{m}{(ze)B_\phi R} \frac{v^2}{2} ,$$

component of the motion continues to govern the particle trajectories and unusually "fat" banana thicknesses occur. This effect is a manifestation of finite gyro-radius conditions and consequently large drift velocities.

Increasing the initial pitch angle further, orbit (e) where Cos χ = 0.07, results in the degenerate or stagnation orbit shown as a point on Fig. 3. At this specific pitch angle, the toroidal drift velocity in the +y direction and the motion along the field line in the -y direction cancel precisely. Such a particle traverses the device in the toroidal direction with no apparent motion in the cross section view.

The final two orbits in the sequence, Cos χ = 0.02 and 0.0, (f) and (g), follow directly. Initially, the particle motion is governed

by the drift velocity component and the particles move approximately vertically. The particles are costreaming so that motion along a field line causes a clockwise rotation in the cross section view. This poloidal motion increases as $v_{||}$ increases due to the decreased magnetic field experienced by the particles, and the orbits close as shown. Note that these particles are untrapped since $\vec{v}_{||} \cdot \vec{J} \geq 0$ everywhere along the orbits. Also, the orbits occupy a region of space in which $R > R_B$ unlike the preceding costreaming examples.

In summary, charged particle guiding center orbits where finite gyro-orbit effects cannot be neglected can best be understood by considering the orbits as a summation of motion along a field line and, for the field directions assumed, an upward drift motion. Results depend strongly on the initial conditions chosen. For costreaming particles and the initial spatial conditions described above, the two component motions can be oppositely directed, as in the small pitch angle examples, or in the same direction, as in the large ($\chi \approx \pi/2$) pitch angle examples. The stagnation orbit separates these two distinct regions of pitch angle space. Finally, it is the fact that the two component motions can be in opposite directions, depending on the pitch angle, that leads to untrapped orbits shown in Fig. 3 for χ near $\pi/2$ and the overall trapped particle differences between costreaming and counterstreaming particles.

Figure 4 shows the orbits of counterstreaming particles for the same initial conditions and sequence of pitch angles described above in the costreaming cases. For counterstreaming particles, $\chi = 0$ refers to a particle with velocity antiparallel to the direction determined by

$\vec{J}$. Thus, due to the chosen directions of B_ϕ, J and B_θ, motion along a field line results in a counterclockwise poloidal rotation in the cross section view. As a result, for the initial conditions being considered, typical counterstreaming orbits on Fig. 4 are shown in the upper half of the cross section. However, the toroidal drift velocity is in the +y direction as in the costreaming particle case. Thus, the drift motion results in deviations radially outward relative to the particles' initial flux surface. The first two examples, Cos χ = 1.0 and 0.6, (a) and (b), represent untrapped particle orbits, are approximately circular, and deviate outside of their corresponding flux surface r = 0.5. For all higher pitch angles shown, orbits (c)-(g), trapped particle orbits result. This behavior is not consistent with the costreaming particle results. Physically, the initial direction of both the drift motion and the motion along a field line is always +y for counterstreaming particles causing the difference from the costreaming cases. Here, whether the orbit motion is dominated by motion along a field line or drift motion, the particle moves initially upward. Further, the counterclockwise poloidal motion <u>always</u> causes the particle to orbit into a region of increased magnetic field, again unlike the special cases described for $\chi > \chi_{stagnation}$ in the costreaming examples. As shown by the counterstreaming orbits on Fig. 4, once the initial pitch angle required for trapping is exceeded, only trapped orbits occur for increased χ, including $\chi = \pi/2$.

It is clear that $\chi = \pi/2$ is neither a costreaming nor a counterstreaming particle, but rather separates the two classes of particles. Then, as χ approaches $\pi/2$ from the costreaming or counterstreaming side

of pitch angle space, the physical orbits must converge to a common $\chi = \pi/2$ case. The two closed orbits shown on both Figs. 3 and 4, (f) and (g), illustrate that this occurs. In the costreaming case, Fig. 3, the orbits for χ near $\pi/2$ approach the $\chi = \pi/2$ orbit shown from the inside and in the counterstreaming case, Fig. 4, from the outside. Nevertheless, in both cases the orbits converge to a common $\chi = \pi/2$ orbit, orbit (g), and the progression from costreaming to counterstreaming particle orbits is continuous.

Figure 5 shows the velocity space boundaries between trapped and untrapped particle space for the initial conditions given previously. Since

$$P = \frac{2qv}{\Omega a} \equiv \tilde{v}$$

$$P \cos \chi = \tilde{v}_{\|}$$

$$P \sin \chi = \tilde{v}_{\perp}$$

$$P = [\tilde{v}_{\|}^2 + \tilde{v}_{\perp}^2]^{1/2} ,$$

a specified value of P determines a semicircle on Fig. 5 and locations along the arc are determined by the initial pitch angle of the particle of interest. For example, 3.5 MeV alpha particles in an I = 5 MA device correspond to P = 0.135 and the $\tilde{v} = 0.135$ arc shown. Similarly, the marks along the arc show the initial pitch angles for the orbits in Figs. 3 and 4. The "lobe" region designating trapped particle space for the costreaming particles is consistent with the explanation given above since, as χ increases from $0 \rightarrow \pi/2$, particles progress from untrapped-trapped-untrapped orbits. Alternately, for the

counterstreaming particles, as χ increases from $0 \rightarrow \pi/2$, particles progress from untrapped-trapped orbits, i.e., particles with $\chi \geq \chi_{trap}$ are in trapped orbits without exception. Also, for the same initial spatial conditions, A = 4 and I $\leq$ 3.7 MA, note that no costreaming 3.5 MeV alpha particles are in trapped orbits. Finally, the trapping characteristics for $P = \tilde{v} = .06$ are shown. This case represents either 3.5 MeV alpha particles in an I $\approx$ 10 MA machine or 1 keV protons in an I $\approx$ 185 kA machine. In these cases, finite gyro-orbit effects are less pronounced. The region of pitch angle space near $\chi = \pi/2$, wherein co-streaming particles are untrapped, is small. The pitch angle where trapping first occurs is approximately the same for both costreaming ($\chi_{trap} \approx 66^{o}$) and counterstreaming particles ($\chi_{trap} \approx 60^{o}$) and compares favorably to that predicted in the limit of zero gyro-radius,

$$\chi_{trap} = \text{Cos}^{-1} \, (2r/R)^{1/2} \approx 62^{o} \quad .$$

Thus, as P decreases either due to increased plasma current or consideration of low energy particles, gyro-orbit effects diminish and trapping and orbit characteristics approach those normally shown.

The foregoing discussion was devoted to orbit details to emphasize the fundamental differences in the orbit and trapping characteristics of particles where small gyro-orbit approximations are and are not valid. Alpha particles ($\sim$ 3.5 MeV) in fields consistent with plasma currents $\leq$ 10 MA ($\rho_{\theta}/a \geq 0.1$) require detailed orbit considerations. In future devices which will contain alpha particles (I = 2-5 MA) orbit effects are not small, vary markedly between costreaming and counter-streaming particles and motivate careful analysis of alpha particle

losses due to orbit excursions, as well as the corresponding momentum and electrostatic charging effects.[21]

C. Alpha Particle Containment Properties

There are various concerns associated with alpha particle behavior in a tokamak. In the remainder of this chapter the alpha particle containment characteristics for several representative plasma sizes are considered. Size is used interchangeably with plasma current since for constant q, A and B_ϕ

$$q = \frac{1}{A}\frac{B_\phi}{B_\theta}$$

so that

$$a = \left(\frac{\mu_0\ q\ A}{B_\phi\ 2\pi}\right) I \quad ,$$

and size varies linearly with current. The interest here is in the fraction of alpha particles produced in the system on orbits which intersect the limiter, first wall, or an active divertor region and are lost from the plasma. For the present purpose, a particle produced on an orbit which makes an excursion outside of the plasma boundary r = a is defined as lost.

Alpha particles are produced with a spatial profile given by

$$S_\alpha(r) = n_D n_T \langle \sigma v \rangle_{DT} \quad ,$$

and isotropically in velocity space. It is assumed that the plasma density and temperature are constant on a flux surface; therefore, $S_\alpha = S_\alpha(r)$. However, the fraction of particles lost due to orbit effects from various poloidal locations on the same flux surface is not

constant. Thus, the fraction of alpha particles produced isotropically at a particular spatial point in the plasma that is lost from the system is computed. The orbit equation, [cf. Equation (7)], is solved numerically for given initial spatial conditions to determine a "loss cone" in pitch angle space. Particles produced with pitch angles in the range of the loss cone are lost from the system. The fraction of alpha particles lost follows directly. For example, consider the costreaming alpha particles produced at r_B,θ_B and assume the corresponding loss cone limits are found to be χ_1, χ_2. The fraction of alpha particles lost from r_B,θ_B is

$$f_L(r_B,\theta_B) = \frac{\int_{\chi_1}^{\chi_2} 2\pi \text{ Sin } \chi \, d\chi}{\int_0^{\pi/2} 2\pi \text{ Sin } \chi \, d\chi}$$

$$= \text{Cos } \chi_1 - \text{Cos } \chi_2 \quad .$$

Implications of the inhomogeneous losses on a particular flux surface are discussed in a later chapter of this thesis. Here, the losses are averaged poloidally to obtain loss fractions which are flux surface averages and, therefore, a function of minor radius only, i.e.,

$$\langle F_L \rangle = \frac{1}{\pi} \int_0^{\pi} f_L(r_B,\theta_B) \, d\theta_B \quad .$$

Note that $\langle F_L \rangle$ is a general result and depends parametrically on I and A. The results are used in conjunction with an assumed spatial dependence and magnitude for a particular alpha particle source. For the overall system, the fraction of alpha particles lost is

$$L_\alpha = \frac{\int S_\alpha(r)\ \langle F_L \rangle\ 2\pi r dr}{\int S_\alpha\ 2\pi r dr} \quad .$$

A general indication of the containment characteristics of various plasma sizes is shown on Fig. 6. The plasma current required to contain all alpha particles produced within a specified minor radius, as a function of aspect ratio, is shown. For example, in an A = 3 device, if $I \geq 5$ MA, all alpha particles produced in the region $0 \leq r/a \leq 0.4$ are contained. Figure 6 suggests that reactor size plasmas, ($I \geq 10$ MA), will provide good overall alpha particle containment whereas feasibility size devices, ($I = 2\text{-}5$ MA), may experience losses from virtually all regions of the plasma and require further consideration. Finally, note from Fig. 6 that as A increases, toroidal gradient and curvature effects are reduced resulting in smaller orbit excursions and improved containment for a given value of plasma current.

In terms of plasma current levels or size, the absolute containment of alpha particles discussed above is very demanding. For A = 3 and various currents, Fig. 7 shows the fraction of alpha particles produced isotropically at specified minor radii that is lost from the system due to orbit excursions. Although Fig. 6 showed that I = 5 MA was required for absolute confinement of alpha particles produced within $r/a \leq 0.4$, Fig. 7 shows that I = 3 MA confines greater than 90 percent.

The sensitivity of these results to aspect ratio changes can be determined from Figs. 7 and 8. The figures show the same information for aspect ratios of 3 and 4, respectively. As previously stated,

higher aspect ratio devices provide more efficient containment.

Before leaving the subject of loss fractions and analyzing the distributions of contained particles, the sensitivity of containment properties to the assumed plasma current profiles must be determined. The deviation of a drift orbit from its corresponding flux surface is proportional to the poloidal gyro-radius of the particle. Since,

$$\rho_\theta \propto 1/B_\theta \ ,$$

the poloidal gyro-radius of a particle at r_p is inversely proportional to the total plasma current within the region $r \leq r_p$, i.e.,

$$B_\theta(r_p) = \frac{\mu_0}{2\pi r_p} \int_0^{r_p} J(r) 2\pi r dr \ .$$

Thus, a total plasma current, I, distributed according to a peaked current density profile, provides better particle containment than a flat profile. Three cases are considered to determine the importance of the effect of current density profile. Figure 9 shows the three profiles assumed. In all cases the profiles are normalized so that

$$\frac{1}{\pi a^2} \int_0^a 2\pi r \, J(r) dr = 1 \ ,$$

and J(r) can be scaled to obtain a desired total current.

Figure 10 shows the resulting loss fractions computed for the three profiles and a total current of 1 MA. As the current density profiles become increasingly peaked, the most pronounced improvement in alpha containment occurs for particles produced near the center of the discharge. This is to be expected since the current within a small circle

of radius r is increased approximately in the ratio 1:2:3 for the three profiles considered. However, since I = 1 MA in all cases, the current within circles of large radii must approach 1 MA as r approaches a, independent of the current density profile examined. Relative to constant current profiles, if larger devices operate with parabolic or even more peaked profiles, alpha containment will be improved by about a factor of 2 or more in the central plasma regions and essentially unaffected in the peripheral plasma zones. Figure 11 shows the corresponding results for I = 3 MA. Both Figs. 10 and 11 show that the alpha containment characteristics are qualitatively similar as various plasma current profiles are considered. The fraction of particles contained improves as the profiles become more peaked. In view of the uncertainty as to what profile should realistically be assumed for future devices, the conservative constant current density case is used in the remainder of this work.

Finally, the alpha particle source radial dependence is obtained from

$$S_\alpha = n_D n_T \langle \sigma v \rangle_{DT} \quad ,$$

and as such is a function of both the ion temperature and density profiles. Thus, the details of S_α are machine dependent. Three representative profiles are examined here ranging from flat to relatively peaked, i.e.,

$$S_{\alpha 1} = S_0$$

$$S_{\alpha 2} = S_0 (1 - r^2/a^2)^2$$

$$S_{\alpha 3} = S_0 (1 - r^2/a^2)^5 \quad .$$

Table I reflects the total fraction of alpha particles contained for several systems and the three production profiles defined above. The fraction contained is obtained from

$$F_C = 1 - \frac{\int_0^a 2\pi r\, S_\alpha(r)\, \langle F_L \rangle dr}{\int_0^a 2\pi r\, S_\alpha(r) dr} \quad . \tag{11}$$

Similarly the limiting cases for I = 1 MA, A = 3 yield $F_C = 0.15$ for $S_{\alpha 1}$ and J(r) constant and $F_C = 0.80$ for $S_{\alpha 3}$ and $J(r) = 3(1-r^2/a^2)^2/\pi a^2$.

TABLE I

Fraction of Alpha Particles Contained for Specified Production Profiles

I (MA)	$S_{\alpha 1}$		$S_{\alpha 2}$		$S_{\alpha 3}$	
	A = 3	A = 4	A = 3	A = 4	A = 3	A = 4
1	0.15	0.26	0.21	0.38	0.23	0.46
2	0.41	0.51	0.60	0.73	0.69	0.80
3	0.56	0.66	0.79	0.88	0.87	0.94
5	0.73	0.79	0.94	0.97	0.99	~ 1.0

D. Conclusions

Alpha particle orbits in machines where I $\leq$ 5 MA were found to exhibit unusual characteristics compared to the orbits normally shown for present day plasmas. The differences result from high alpha particle energy and correspondingly large gyro-radii and drift velocities. Finite gyro-radii effects were found to be important in determining the trapped particle-untrapped particle boundaries in pitch angle space and

to lead to a preferential loss of counterstreaming ($\vec{v}_{\|} \cdot \vec{J} < 0$) particles from the system. The details of the latter effect are examined in the next chapter. The motivation for discussing the orbits here is to emphasize the necessity of considering the individual orbit characteristics since drift orbits deviate markedly from their corresponding flux surfaces and a small gyro-radius expansion procedure cannot be used in general.

With the orbit model developed, the results show that alpha particle containment properties improve as A increases, as the plasma current density profile becomes more peaked and when the total plasma current is increased. If future devices operate with parabolic or steeper current profiles, alpha particle containment will improve by about a factor of two for particles produced near the center of the discharge as compared to the results for flat current profiles. In addition, overall containment in a given system improves for more steeply peaked alpha particle source distributions simply because particles produced near the discharge center must undergo large orbit excursions to reach the plasma boundary. Conservatively assuming a constant current profile, Table I shows typical numerical results for the fraction of alpha particles contained by several systems. Reactor size devices ($I \gtrsim 10$ MA) will efficiently contain alphas. Feasibility size devices ($I \approx 2$-5 MA), depending on profiles, etc., will contain $\gtrsim 75$ percent of the alpha particles produced.

Due to the strong dependence of the alpha particle production rate on ion temperature, > 75 percent containment is adequate from a heating point of view since operation at a moderately higher temperature will

compensate for the alpha particles lost. However, the implication of a preferential loss of counterstreaming particles is a net momentum input to the plasma in addition to the distributed momentum which may exist due to finite gyro-orbit effects.

These considerations are analyzed in the next section of this thesis by determining the distribution function for alpha particles which are contained by the system.

III. ALPHA PARTICLE DISTRIBUTIONS AND EFFECTS

A. Motivation and Assumptions

In the preceding chapter a general analysis of the fraction of alpha particles lost from various size systems was given. For the most conservative assumptions, devices with plasma currents of several million amperes were found to have fractional losses less than 25 percent. Reactor size devices provide very efficient containment. However, where losses occur, initially counterstreaming particles are preferentially lost from the plasma. This unbalanced loss implies a net momentum input to the background plasma due to alpha particles. In addition to this effect, the associated electrostatic charging in the plasma and the distributed momenta profiles which occur must be considered.

In this chapter a model is developed and used to analyze the alpha particles which are contained. Specifically, the distribution function of uncollided 3.5 MeV alpha particles resulting from a particular alpha source profile will be determined. From the distribution function the energy density deposition rate profiles due to the alphas and the spatial dependence of their momentum input to the background plasma can be computed directly.

The orbit of a monoenergetic particle in the model used is periodic with a period defined as the bounce period, i.e., the time required to execute one closed orbit in the reference frame shown on Figs. 3 and 4. The orbits shown on the figures are defined as bounce orbits. It will be shown a posteriori that, in general, the bounce time scale, τ_b, is much less than the alpha particle slowing down time scale, τ_f.

Thus, the alpha particles execute many bounce orbits during one slowing down time. Further, a fast test ion in a background plasma slows down to the critical energy, E_{crit}, primarily due to collisions with the background electrons and, therefore, undergoes little pitch angle scattering at energies greater than E_{crit}.[22] The rate of loss of fast ion energy to the electrons and ions is equal at energy E_{crit} which is given by[1]

$$E_{crit} \approx 14.8\ T_e \left[\frac{A^{3/2}}{n_e} \sum_j \frac{n_j z_j^2}{A_j} \right]^{2/3}$$

where

$T_e \equiv$ electron temperature in eV;

$n_e \equiv$ electron density in cm^{-3};

$A \equiv$ fast ion atomic mass number;

and the summation includes all ion species. In a plasma consisting of 50%D-50%T, $n_e = 10^{14}$ cm^{-3} and $T_e = 10$ keV,

$$E_{crit} \approx 360 \text{ keV}$$

for an alpha particle. Thus, a 3.5 MeV alpha particle will transfer approximately 90 percent of its energy to the background plasma before appreciable pitch angle scattering occurs. The distribution function computed for fast alphas then will be used to estimate the alpha particle heat deposition profiles and other effects.

Detailed charged particle slowing down calculations have been performed by numerous authors.[23] Here, following Stix,[1] note that the approximate time required for a 3.5 MeV alpha particle to slow down to E_{crit} is

$$\tau_f = \frac{t_s}{3} \ell n \left[1 + \left(\frac{E_\alpha}{E_{crit}} \right)^{3/2} \right] - \frac{t_s}{3} \ell n\, 2 \quad ,$$

where

$$t_s = \frac{6.27 \times 10^8 \; A \; T_e^{3/2}}{z^2 \; n_e \; \ell n \; \Lambda} \quad .$$

Using the same assumptions as above in computing E_{crit} and taking $\ell n\, \Lambda \approx 17$,

$$t_s = 0.370 \text{ sec}$$

and, therefore,

$$\tau_f = 340 \text{ msec} \quad .$$

By comparison, in a reactor with a major radius $R_0 = 10$ meters and a safety factor $q = 3$, a 3.5 MeV alpha particle with $v_\parallel \gg v_\perp$ has a bounce time

$$\tau_b \approx q \left(\frac{2\pi R_0}{v} \right)$$

$$\tau_b = 15 \; \mu\text{sec} \quad .$$

In this typical example the alpha particle completes more than 20,000 bounce orbits in the time required to slow down to E_{crit}. Thus, the assumption $\tau_b \ll \tau_f$ is valid for cases where $v_\parallel \gg v_\perp$. Next, τ_b is calculated for alpha particles with all pitch angles and the validity

of the assumption is demonstrated in general.

B. Numerical Model of Alpha Particle Dynamics

1. Bounce Time, τ_b. The bounce period is defined as

$$\tau_b = \oint dt' \tag{12}$$

where the integration path is taken along the orbit of interest. Recall from the orbit model previously developed that the drift component of velocity is in the $\pm y$ direction. Therefore, a guiding center velocity in the $\pm x$ direction can occur only due to motion along a field line. The poloidal velocity which results from motion along a field line, in terms of the coordinates defined in Fig. 1, is

$$v_\theta = v_{\|} \frac{B_\theta}{B_\phi} ,$$

so that

$$v_x = (v \text{ Cos } \chi) \left(\frac{\mu_0 J r}{2}\right) \frac{1}{B_{\phi_0}} \left(\frac{y}{r}\right). \tag{13}$$

Rewriting Equation (12) as

$$\tau_b = 2 \int_{x_1}^{x_2} dx'/v_x' ,$$

and substituting Equation (13) yields

$$\tau_b = \frac{2qR_0}{v} \int_{x_1}^{x_2} \frac{dx'}{y(x') \text{ Cos } \chi'} \tag{14}$$

In Equation (14), χ' is the particle pitch angle which varies along the trajectory, $y(x')$ is the particle trajectory itself, and x_1, x_2 are the x-axis intercepts of the function $y(x)$.

The pitch angle χ' can also be expressed as a function of x' along the orbit. From the conservation of μ,

$$v_{\perp}^2 R = v_{\perp_B}^2 R_B$$

and

$$R = R_0 + x$$

so that,

$$\text{Cos}^2 \chi' = \left(\frac{x' - x_T}{x' + A} \right) \tag{15}$$

where x_T is defined by Equation (8) in terms of the initial conditions of the particle. All lengths have been normalized to the plasma radius. The bounce time now is given by

$$\tau_b = \frac{2qA}{v/a} \int_{x_1}^{x_2} \sqrt{\frac{x' + A}{x' - x_T}} \frac{dx'}{y(x')} \quad , \tag{16}$$

a function of x' only. Consider the orbit passing through $x_B = 0.5$, $y_B = 0.0$ with Cos $\chi = 1.0$ and $A = 4$. The orbit equation in this case was given previously as

$$y(x) = [(0.5 - P/2)^2 - (x - P/2)^2]^{1/2} \quad ,$$

from which

$$x_1 = P - 0.5$$

$$x_2 = 0.5$$

and

$$x_T = -A \quad .$$

From Equation (16),

$$\tau_b = \frac{2qA}{v/a} \int_{P-.5}^{.5} \frac{dx'}{[(.5-P/2)^2 - (x'-P/2)^2]^{1/2}} = \frac{2qa}{v/a} \text{Sin}^{-1} \left[\frac{x'}{(.5-P/2)} \right]_{P/2-.5}^{.5-P/2}$$

$$= q(2\pi R_0/v) \quad ,$$

which is the expected result for a particle with $v_{||} = v$. Due to the rotational transform, the particle must complete q toroidal transits around the machine to complete one closed orbit poloidally. Defining the bounce time for a particle with $v_{||} = v$ as τ_{b_0}

$$\tau_b/\tau_{b_0} = \frac{1}{\pi} \int_{x_1}^{x_2} \frac{dx'}{y(x') \text{ Cos } \chi'} \tag{17}$$

which must be integrated numerically except for the simple case just discussed.

Figure 12 shows typical trapped and untrapped orbits and the relevant integral limits in each case. Since the integrand in Equation (17) depends on the reciprocals of $y(x')$ and Cos χ', singularities exist at x_1 and x_2 in the case of an untrapped orbit and x_1, x_2 and x_T for a trapped orbit. The trapped orbit integral may be written as

$$\tau_b = \int_{x_1}^{x_T} \frac{dx'}{v'_x} + \int_{x_T}^{x_2} \frac{dx'}{v'_x} \quad ,$$

so that all integrals to be performed are similar in form and singular at the end points of the integration interval. Consider the general form of Equation (7) written for an initially costreaming, untrapped particle; that is,

$$y(x) = [C - x^2 + P\{(x - x_T)(x + A)\}^{1/2}]^{1/2} \quad .$$

In the region near intercept x_1,

$$x = x_1 + \Delta$$

where Δ is a small parameter. Therefore,

$$y(x) = [C - x_1^2 - 2x_1\Delta - \Delta^2 + P\{(\Delta + x_1 - x_T)(\Delta + x_1 + A)\}^{1/2}]^{1/2}$$

in this region. Expanding the inner square root in powers of Δ yields

$$y(x) \approx [C - x_1^2 - 2x_1\Delta + P\{(x_1 - x_T)(x_1 + A)\}^{1/2} + \frac{P\Delta}{2} \frac{2x_1 - x_T + A}{[(x_1 - x_T)(x_1 + A)]^{1/2}} + O(\Delta^2)]^{1/2} .$$

By definition,

$$y(x_1) = \left[C - x_1^2 + P\{(x_1 - x_T)(x_1 + A)\}^{1/2}\right]^{1/2} .$$

so that

$$y(x) = \sqrt{\Delta}\left[-2x_1 + \frac{P}{2} \frac{2x_1 - x_T + A}{\sqrt{(x_1 - x_T)(x_1 + A)}}\right]^{1/2} + O(\Delta) \quad . \qquad (18)$$

Provided that the coefficient of $\sqrt{\Delta}$ is not zero, the singularity due to $y(x_1) = 0$ is integrable because

$$1/y(x) \propto 1/\sqrt{x - x_1} \quad .$$

The other possible singularities are shown to be integrable in a similar manner. The tedious, but necessary, details to understand the precise conditions which result in a non-integrable singularity have been relegated to Appendix A. Particles which satisfy the precise conditions comprise a very small class and have been neglected here.

The general form of Equation (17) which must be integrated is

$$\tau_b/\tau_{b_0} = \frac{1}{\pi} \int_{x_1}^{x_2} \frac{g(x)\, dx}{\sqrt{x - x_1}\sqrt{x_2 - x}} \quad ,$$

where $g(x)$ is a well behaved function. This integral may efficiently

be computed numerically[24] using the Gaussian integration form,[25]

$$\int_{x_1}^{x_2} \frac{g(x)\,dx}{\sqrt{x - x_1}\,\sqrt{x_2 - x}} = \sum_{k=1}^{N} w_k\, g(x_k) \tag{19}$$

$$x_k = \frac{x_2 + x_1}{2} + \frac{x_2 - x_1}{2} \operatorname{Cos}\left(\frac{2k - 1}{2N}\,\pi\right)$$

$$w_k = \frac{\pi}{N} ,$$

where the related orthogonal polynomials are the Chebyshev Polynomials of the First Kind.

2. Distribution Function, f. The uncollided alpha particle distribution function, f, obeys the Vlasov equation,

$$\frac{\partial f}{\partial t} + \vec{v} \cdot \nabla f + \vec{a} \cdot \nabla_v f = S_\alpha , \tag{20}$$

where a source of alphas has been included. Using the method of characteristics,[26,27] Equation (20) may be written as,

$$\left[\frac{df}{dt'}\right]_{orbit} = S_\alpha(x',y',\chi', t') , \tag{21}$$

so that,

$$\int df(x',y',\chi',t') = \int S_\alpha(x',y',\chi',t')dt' . \tag{22}$$

Primed coordinates represent those measured along the orbit of interest. It is assumed that no alpha particles are present in the system at t = 0 and Equation (22) can be integrated to yield,

$$f(x,y,\chi,t) = \int_0^t S_\alpha(x',y',\chi',t')dt' , \tag{23}$$

since when $t = t'$,

$$x = x'$$

$$y = y'$$

$$\chi = \chi'.$$

Physically,[28] Equation (23) states that the distribution function for particles at x,y with pitch angle χ at time t is composed of particles which were produced at all possible $t' \leq t$, x', y' and χ' on orbits which subsequently pass through x,y with the desired pitch angle at time t. For example, specifying a particular coordinate and pitch angle of interest in the plasma is equivalent to fixing the initial conditions for a single particle orbit. Thus, only sources along that orbit can produce particles which pass through the coordinate of interest with the required pitch angle. The right hand side of Equation (23),

$$\int_0^t S_\alpha(x',y',\chi',t')dt' ,$$

expresses the sum of such sources over all previous time. S_α is the source per unit time per unit volume per steradian and dt' includes the precise orbit information and integration path. Also, $dt' = dx'/v_{x'}$ provides the appropriate weight factor to the integrand to account for the fact that both the source strength and the time interval over which it can contribute to the total distribution function are important.

In the present problem the bounce orbit is repeated many times in the time interval t. Then,

$$f(x,y,\chi,t) = \int_{t-\tau_b}^{t} S_\alpha dt' + \int_{t-2\tau_b}^{t-\tau_b} S_\alpha dt' \ldots \tag{24}$$

$$+ \int_{0}^{t-\tau[t/\tau]} S_\alpha \, dt' \ ,$$

where the last integral represents the transient part of the solution or particles in the process of completing their first bounce orbit. Thus, to lowest order in τ_b/t, the final form of Equation (23) is

$$f(x,y,\chi,t) = \frac{t}{\tau_b} \int_0^{\tau_b} S_\alpha(x',y',\chi',t')dt' \ . \tag{25}$$

The alpha particle source distribution, S_α, has a magnitude and spatial dependence determined by the ion temperature and density profiles and is assumed isotropic in velocity space, i.e.,

$$S_\alpha = n_D(r)\, n_T(r)\, \langle\sigma v\rangle_{DT} \left(\frac{1}{4\pi}\right)$$

$$S_\alpha = \frac{S_0}{4\pi}\, g(r) \ .$$

In the last equation $S_0 = n_D\, n_T\, \langle\sigma v\rangle_{DT}$ evaluated at $r = 0$ and $g(r)$ includes the radial dependences of these quantities.

In summary then, the equations which are integrated by the method outlined above, [cf. Equation (19)], are,

$$f(x,y,\chi,t) = \frac{2t}{\tau_b} \int_{x_1}^{x_2} \frac{S_\alpha(x')\, dx'}{v_x'} , \tag{26}$$

$$\tau_b/\tau_{b_0} = \frac{1}{\pi} \int_{x_1}^{x_2} \frac{dx'}{y(x')\ \mathrm{Cos}\ \chi'} . \tag{27}$$

C. Determination of Alpha Particle Bounce Times and Distribution Functions

In this section typical numerical results for τ_b and f obtained by exercising the procedures in Section III.B. are described.

Figure 13 shows the normalized bounce times for initially costreaming alpha particles produced at $x_B = 0.5$, $y_B = 0.0$ as a function of their initial pitch angle. The bounce times for various pitch angles are expressed as multiples of the the bounce time for the $v = v_{||}$ (Cos $\chi = 1.0$) particle. In this way the actual machine size differences in the three cases shown need not be considered in interpreting the relative times physically. For example, when Cos χ = 0.45 the particles in all three cases are on untrapped orbits. The particle in the I = 10 MA machine has a longer bounce time relative to τ_{b_0} (I = 10 MA) than the particle in the I = 5 MA machine relative to its τ_{b_0}. Recall that costreaming particles drift to the inside of their initial flux surface. Also, due to the larger Larmour radii, drift motion effects are more pronounced in the lower current machines. Therefore, the Cos χ = 0.45 particles deviate further to the inside of their flux surface when I = 5 MA than when I = 10 MA. As a result, the orbit in the I = 5 MA device does not penetrate as far into the

magnetic field gradient as the 10 MA orbit, maintains a larger average $v_{||}$ over the bounce orbit and has a shorter relative bounce time. The same argument applies to the I = 2 MA orbit compared to that in the I = 5 MA case.

In the case of trapped orbits, consider the I = 5 and 10 MA curves for Cos χ = 0.3. By definition, $v_{||} = 0$ at some point along a trapped orbit. The bounce time for a trapped particle is determined by the particle dynamics in the region of the orbit turning point, (cf. Appendix A). Again, the drift effects are more pronounced in the I = 5 MA vs. 10 MA machine. Thus, in regions where $v_{||} \approx 0$, motion is dominated by the drift velocity so that the time spent in such regions is reduced for low current devices relative to higher current devices. This explains the longer relative bounce times for trapped particles in the 10 MA machine compared to the 5 MA machine. Note from Fig. 5 that for the corresponding initial conditions, no costreaming particles are trapped for I = 2 MA so that no further comparison can be made.

Figure 14 shows the normalized bounce times for the same initial spatial conditions but counterstreaming alpha particles. For trapped orbits the arguments above apply as to why τ_b/τ_{b_0} (I = 10 MA) > τ_b/τ_{b_0} (I = 5 MA). However, for untrapped orbits, counterstreaming particles drift to the outside of their initial flux surface. Thus a particle on an untrapped orbit in a low current device will drift further into the magnetic field gradient and have a longer relative bounce time than the corresponding particle in a higher current device. This is the opposite of the result found for costreaming particles.

The difference occurs due to the drift effect and whether the drift orbit is inside or outside of the corresponding initial flux surface.

In all cases, relative bounce times greater than 10 occur for a very small class of particles as shown by Figs. 13 and 14. In the example computed previously,

$$(\tau_{b_0}/\tau_f) \approx 5 \times 10^{-5}$$

so that,

$$(\tau_b/\tau_{b_0}) = 10$$

yields,

$$(\tau_b/\tau_f) \approx 5 \times 10^{-4} \ .$$

The assumption that particles execute many bounce orbits in one slowing down time is therefore valid in general. In some cases, a small class of particles in the transition region between trapped and untrapped particle orbits have very long bounce times and they are neglected here.

Finally, Fig. 14 indicates that counterstreaming particles at $x_B = 0.5$, $y_B = 0.0$ in an I = 2 MA device with pitch angles between Cos $\chi = 0.11$ and Cos $\chi = 0.59$ are on orbits which make excursions outside of the plasma. The bounce time for such cases cannot be computed since the particles are lost from the system and the distribution function in this region of pitch angle space is zero.

A few further comments on the discontinuities shown on Figs. 13 and 14 should be made. Appendix A explains in detail how such discontinuities result from the analysis. It is important to recognize that the sharp discontinuities will not actually occur physically. For example, both higher order drift terms[29] and collisions, which have not been treated here, will affect the particles in this narrow range of pitch angle space. Since the time scales for these processes are long, the sharp "corners" shown on Figs. 13 and 14 (and Figs. 15, 17 and 18 discussed later) will be alleviated but the overall shape of the curves will not be affected.

Results in the remainder of this work rely on integrals of some distribution functions which have discontinuities in their slopes but are everywhere finite. (See Figs. 15, 17 and 18). As such the calculational model used here is adequate for the present purpose. Recognition is given to the fact that physical processes will prevent such sharp structures from occurring in nature.

Turning to the calculation of the alpha particle distribution function, f, Equation (26) is rewritten as,

$$f(x,y,\text{Cos }\chi,t) = t\,\frac{\int_{x_1}^{x_2} S_\alpha(x')\,\frac{dx'}{v_{x'}}}{\int_{x_1}^{x_2}\frac{dx'}{v_{x'}}} \,. \qquad (28)$$

The remaining computations depend on the source distribution of alpha particles. Assume that,

$$S_\alpha = \frac{S_0}{4\pi}(1 - r^2/a^2)^2$$
$$= \frac{S_0}{4\pi}\left(1 - \frac{x^2}{a^2} - \frac{y^2(x)}{a^2}\right)^2$$
$$= \frac{S_0}{4\pi}\, g(x') \ ,$$

which represents a system with a constant ion temperature and a parabolic density profile. Then,

$$f(x,y,\text{Cos}\ \chi,t) = \frac{S_0\, t}{4\pi} \frac{\int_{x_1}^{x_2} g(x')dx'/v_{x'}}{\int_{x_1}^{x_2} dx'/v_{x'}} \qquad (29)$$

is evaluated numerically to determine the distribution function at x,y as a function of Cos χ and time t.

Figure 15 shows the normalized fast alpha particle distribution functions which result at x/a = 0.5, y/a = 0.0 due to the source shape assumed for four plasma current levels. Each distribution is a function of pitch angle, $0 \leq \text{Cos}\ \chi \leq 1.0$, and includes costreaming ($\vec{v}_{\|} \cdot \vec{J} \geq 0$) particles only. The case I = ∞ represents zero Larmour radius so that particles are perfectly confined to their initial flux surface. Thus,

$$f(x,y,\text{Cos}\ \chi,t) = t \frac{\oint \frac{S_0}{4\pi}(1 - r'^2)^2\, dt'}{\oint dt'}$$

but $r = r' =$ constant since in this limiting case particle flux surfaces and drift orbits are coincident, and,

$$f(x,y,\text{Cos } \chi,t) = \frac{S_0}{4\pi} (1 - r^2)^2 \, t \ .$$

At $x/a = 0.5$, $y/a = 0.0$, $r/a = 0.5$ so that the last equation yields

$$\frac{4\pi}{S_0 t} f = 0.56 \ ,$$

which is shown on Fig. 15. Note that in this ideal case the distribution function is isotropic and has the same radial dependence as the source function. It stands to reason that since orbits are confined to a flux surface and the alpha particle source is constant on a flux surface, time weighting and averaging the source rate over a bounce orbit provides no new information.

However, consider the orbits shown on Fig. 16. The orbits represent the integration paths which must be followed to compute the distribution function at $x/a = 0.5$, $y/a = 0.0$ and a particular pitch angle given by $\text{Cos } \chi = 0.43$. The $I = \infty$ case has been discussed. A trapped particle orbit occurs in the $I = 10$ MA case. Thus the distribution function at $x/a = 0.5$, $y/a = 0.0$ for $\text{Cos } \chi = 0.43$ is expected to be composed primarily of particles which were actually produced near the turning point of the orbit. This is a result of the fact that the distribution is a function of both the source strength and time a particle spends in a particular source region. The turning point is shown on Fig. 16 at $r/a = 0.33$. Thus,

$$\frac{4\pi}{S_0 t} f = (1 - .33^2)^2 = 0.79 ,$$

which compares well with the value for the I = 10 MA distribution function at Cos χ = 0.43 on Fig. 15.

The untrapped particle orbit for the I = 2 MA case, Fig. 16, does not permit an intuitive interpretation of f. One conclusion can be drawn. Since the orbit is entirely within r/a = 0.5, it is in a region of higher source strength than the source strength on the flux surface r/a = 0.5. Thus, it is expected that

$$\frac{4\pi}{S_0 t} f_{2MA} > \frac{4\pi}{S_0 t} f_{\infty} ,$$

for the spatial point and pitch angle being considered. In fact the I = 2 MA and I = ∞ distribution functions are 0.78 and 0.56, respectively.

Figure 17 shows the normalized distribution functions for the same spatial point but for counterstreaming particles. It is noted again that the sharp discontinuities which result from the analysis would be smoothed out by physical processes in an actual system. Here the discontinuities in the slope of the distribution functions occur where the transition between trapped and untrapped particle orbits take place. The I = 2 MA distribution for counterstreaming particles is zero between Cos χ = 0.11 and 0.59. Counterstreaming particles which pass through x/a = 0.5, y/a = 0.0 with a pitch angle in this range make an excursion outside of the plasma radius and are considered lost.

A similar loss cone determination for fast ions produced in a system by neutral beam injection and the implications of the loss cone on injection heating are treated elsewhere.[30,31]

D. Determination of Alpha Particle Heating and Momentum Profiles

From the distribution functions computed as described above, estimates of the alpha particle heating and momentum profiles in a specific system can be determined. By definition,

$$n_\alpha = \int_{-\pi}^{+\pi} f \, 2\pi \, \mathrm{Sin}\, \chi \, d\chi \ ,$$

so that,

$$\frac{dn_\alpha}{dt} = \frac{S_0}{2} \int_{-1}^{1} h \ (\mathrm{Cos}\ \chi) \ d(\mathrm{Cos}\ \chi) \ , \qquad (30)$$

where,

$$h(\mathrm{Cos}\ \chi) = \frac{4\pi}{S_0 t} f \ (x,y,\mathrm{Cos}\ \chi,t) \ ,$$

which was discussed in the preceding section. Thus, assuming that the profile of fast alpha density production in the plasma is an indication of the energy density deposition rate, it follows that,

$$H(x,y,t) = \frac{S_0}{2} E_\alpha \int_{-1}^{+1} h(\mathrm{Cos}\ \chi) \ d(\mathrm{Cos}\ \chi) \ . \qquad (31)$$

Previously, for the limiting case of zero Larmour radius, $I = \infty$, it was shown that

$$h(\mathrm{Cos}\ \chi) = \frac{4\pi}{S_0 t} f = (1 - r^2)^2 \ .$$

Thus,

$$H(x,y,t) = S_0(1 - r^2)^2 E_\alpha$$

which simply states that making the assumption that alphas are confined to their initial flux surfaces results in an energy density deposition rate profile identical to the alpha production rate profile. For a finite Larmour radius case, Fig. 18 shows the costreaming and counterstreaming distribution functions for x/a = 0.5 and y/a = 0.0 in an I = 5 MA device. Performing the required integrals numerically yields

$$H(0.5,0,t) = S_0 E_\alpha \ (0.534)$$

which is approximately the same as the I = ∞ result,

$$H(0.5,0,t) = S_0 E_\alpha \ (0.562) \quad .$$

However, it is apparent from Fig. 18 that, although the total density is comparable to the zero Larmour radius result, the density is composed of more costreaming than counterstreaming particles. This orbit effect implies a net momentum input to the plasma and suggests that a net flow velocity may develop in the background fluid. This is considered in more detail below.

First, to complete the determination of the heating profiles in various size devices, I = 2, 5, 10 and ∞ MA cases are analyzed. H(x,y,t) is first computed at several points on a given flux surface. The results are then averaged over a flux surface, i.e.,

$$\langle H,(r,t)\rangle = \frac{1}{\pi}\int_0^{\pi} H(r,\theta,t)d\theta \quad , \qquad (32)$$

to obtain energy density deposition rate profiles which are a function of minor radius only.

Figure 19 shows the heating profiles for the four values of plasma current. In a feasibility size device, (I = 2-5 MA), the heating profiles are smaller in magnitude than the source profile because orbit effects have caused the loss of some particles. Also, the orbit effects tend to broaden the heating profile relative to the source shape of alphas. In reactor size devices (I ≥ 10 MA), the usual assumption that the heating profile and source profile are the same can be made with good accuracy. Since the I = ∞ curve represents perfect containment, an estimate of the fraction of alpha particles contained by other plasma currents can be obtained using Fig. 19. For I = 2 MA,

$$F_C = \frac{\int_0^a r\langle H(r,t)\rangle_{2MA}\, dr}{\int_0^a r\langle H(r,t)\rangle_{\infty}\, dr} \approx 73\% \quad .$$

Similarly, for the I = 5 MA case, $F_C \approx 97\%$. These results compare to $F_C(I = 2\ MA) = 73\%$ and $F_C(I = 5\ MA) = 97\%$ shown in Chapter II, Table I where the computations were based on loss fraction considerations.

Finally the alpha particle momentum profiles in the various cases are determined. There have been numerous discussions in the literature about toroidal flow velocities which may develop in the background plasma due to radial electric fields, neutral beam injection, and other sources. Possible relaxation mechanisms which will limit the toroidal flow velocity have also been examined to varying degrees of detail.[32] Figure 18 makes it clear that the alpha particles are a source of momentum to the plasma. Since

$$p_\alpha = \int_{-\pi}^{\pi} f\, m_\alpha v_{||}\, 2\pi \,\mathrm{Sin}\,\chi\, d\chi$$

$$\frac{dp_\alpha}{dt} = \frac{S_0 m_\alpha v_\alpha}{2} \int_{-1}^{+1} h(\mathrm{Cos}\,\chi)\,\mathrm{Cos}\,\chi\, d\,(\mathrm{Cos}\,\chi) \quad , \qquad (33)$$

$$= \dot{M}\,(x,y,t) \quad ,$$

the net momentum input at a point in the plasma can be calculated. For example, in the $I = \infty$ case,

$$h(\mathrm{Cos}\,\chi) = \frac{4\pi}{S_0 t} f = (1 - r^2)^2 \quad .$$

From Equation (33)

$$\dot{M}(x,y,t) = \frac{S_0 m_\alpha v_\alpha}{2} \int_{-1}^{+1} (1 - r^2)^2\,\mathrm{Cos}\,\chi\, d(\mathrm{Cos}\,\chi) = 0 \quad ,$$

and the costreaming and counterstreaming momentum cancel precisely at each point in the plasma. However, this is not the case for finite currents where orbit effects become important. The net momentum input to the plasma on the $r/a = 0.5$ flux surface for $I = 2$, 5, 10 and ∞ MA will be used as an example for discussion here. The results are shown on Fig. 20 where $\theta = 0$ when $x/a = 0.5$, $y/a = 0.0$ and $\theta = \pi$ when $x/a = -0.5$, $y/a = 0.0$. Thus, on a given flux surface, the alpha particle momentum input to the background plasma tends to drive the plasma near $\theta = 0$ and π in opposite directions and establish a toroidal flow velocity with a poloidal shear pattern. Such a toroidal flow velocity inhomogeneity on a flux surface will develop according to the parallel momentum equation

$$m_i n_i \frac{\partial U}{\partial t} = \dot{M} - m_i n_i \frac{U}{\tau_{||}} \tag{34}$$

where U is the toroidal flow velocity, $m_i n_i$ is the background plasma ion mass density; $m_i n_i \gg m_e n_e$ has also been assumed. In the collisionless regime[33]

$$\tau_{||} \approx \tau_{ii} = 6.6 \times 10^{-4} \left(\frac{10^{14}}{n_i}\right) T_i^{3/2} \quad . \tag{35}$$

That is, the characteristic time for parallel ion viscosity to relax the inhomogeneity in the flow velocity buildup on a flux surface is on the order of the ion-ion collision time in the background plasma. The maximum toroidal flow inhomogeneity attained at steady state is

$$\Delta U = \frac{S_0 m_\alpha v_\alpha \tau_{ii}}{m_i n_i} \left[\frac{\dot{M}}{S_0 m_\alpha v_\alpha}\right] \quad , \tag{36}$$

and the term in brackets is taken from Fig. 20. (Here, for conservatism, the maximum value ~ 0.14 has been assumed for the normalized momentum input.) If the flow velocity inhomogeneity exceeds the sound speed in the plasma, shocks may occur and produce deleterious effects on plasma confinement. Thus, Equation (36) is rewritten relative to the sound speed so that

$$\frac{\Delta U}{V_s} = 0.24 \frac{\langle \sigma v \rangle_{DT}}{10^{-16}} T_i(\text{keV}) \times 10^{-4} \quad , \tag{37}$$

$$\frac{\Delta U}{V_s} (5 \text{ keV}) = 1.6 \times 10^{-5} \quad , \tag{37a}$$

$$\frac{\Delta U}{V_s} (10 \text{ keV}) = 2.4 \times 10^{-4} \quad , \tag{37b}$$

$$\frac{\Delta U}{V_s}\ (15\ \text{keV}) = 9 \times 10^{-4}. \qquad (37c)$$

Even in the pessimistic case, Equations (37) show that the time scale for parallel ion viscosity to relax the inhomogeneity in the toroidal flow velocity buildup on a flux surface is sufficiently short to limit it to an acceptably low magnitude.

Due to the parallel ion viscosity action, the momentum may be assumed constant on a given flux surface. The momentum input flux surface averages were performed for the standard cases and the results are shown on Fig. 21. Note that the preferential loss of counter-streaming alpha particles results in a net momentum on <u>every</u> flux surface in the same direction as the plasma current. Again a toroidal flow velocity will develop, but with the sheared velocity pattern in the radial direction. Thus, if ion viscosity is relied on to relax the flow, it is the characteristic time for perpendicular ion viscosity which is of interest. In the collisionless regime[33]

$$\tau_\perp \approx \frac{10\ a^2\ \tau_{ii}}{\rho_i^2 q^2} = 3.7 \times 10^{-2}\ a^2(\text{cm})\ T_i^{1/2}(\text{keV}) \quad , \qquad (38)$$

so that for $a \geq 100$ cm and $T_i \geq 5$ keV, $\tau_\perp \geq 800$ seconds. Perpendicular ion viscosity is not a viable mechanism for relaxing the toroidal flow, therefore, since it would allow a buildup time of hundreds of seconds. Other relaxation mechanisms have been suggested but here the time, τ_B, required for development of an unacceptable flow velocity is computed to determine if the alpha momentum input is large enough to be of concern.

Catto, et al.,[34] describe the stability criterion which prevents a parallel Kelvin-Helmholtz instability from being excited. For $T_e = T_i$, the criterion is

$$U' |L_N| / \sqrt{2T_i/m_i} < 1 \quad , \tag{39}$$

where U' is the gradient of the velocity shear and L_N is the characteristic length associated with the plasma density profile. Assuming $L_N \approx a$ and, conservatively, using the numerical results for the I = 2 MA case from Fig. 21,

$$\Delta U = 1.7 \times 10^5 \frac{\langle \sigma v \rangle_{DT}}{10^{-16}} \left(\frac{\tau_B}{a}\right) = 4.3 \times 10^{+5} \left(\frac{\tau_B}{a}\right) . \tag{40}$$

In Equation (40) $n_i = 10^{14}$ cm^{-3} and $T_i = 15$ keV. With no relaxation mechanism against the toroidal flow buildup assumed, operation for

$$\tau_B \leq 250 \text{ sec}$$

will not excite the instability. The operation time permitted before exceeding the sound speed is different by the factor $\sqrt{T_e/T_i}$ which here is taken as unity.

The implications of the alpha particle momentum input profiles have not been computed in a detailed, rigorous way. Rather, the foregoing somewhat heuristic arguments were made and aimed at known velocity limits and shear flow instabilities to determine the magnitude of the possible problem. The results show that the momentum input is too small, even in cases computed using conservative assumptions, to be of concern. A buildup time of hundreds of seconds is required to develop toroidal velocities near the plasma sound speed and certainly such a

time scale suggests that some yet unknown relaxation mechanism may occur and influence the long term buildup.

There is one other alpha particle effect that must be mentioned. From a plasma heating point of view the loss of alpha particles from the plasma was found to be of little consequence. However, the loss of each alpha particle also causes the plasma to become negatively charged electrostatically. The associated electric fields and potentials in the plasma could greatly affect the dynamics and confinement characteristics of the background plasma depending on the charging rate and potentials attained. Here, as above, an estimate of the magnitude of this possible problem is made to assess its potential importance.

For each alpha particle lost from the system, a negative charge $Q = -2e$ accumulates in the plasma. Thus,

$$\frac{\dot{Q}}{V} = \frac{n_i^2 \langle \sigma v \rangle_{DT} 2e}{4} \quad (1 - F_C), \quad C/m^3\text{-sec} \tag{41}$$

is the electrostatic charging rate per unit volume and F_C is the fraction of alpha particles produced that are contained. The electric field and potential buildup are estimated from Gauss' Law as follows,

$$\frac{\partial}{\partial t} \int E \cdot dS = \frac{\partial}{\partial t} \int \left(\frac{Q}{V}\right) \frac{dV}{\epsilon_\perp}$$

$$\dot{E}_r 2\pi R_0 2\pi a = \frac{\dot{Q}}{\epsilon_\perp}$$

$$\dot{\varphi} \approx \frac{n_i^2 \langle \sigma v \rangle_{DT} 2e}{4} \quad (1 - F_C) \frac{a^2}{2\epsilon_\perp} \quad , \tag{42}$$

where $\dot{\varphi}$ is the rate of change of the potential and $\epsilon_\perp$ is the perpendicular dielectric constant $\approx \epsilon_0 \ (1 + \omega_{pi}^2/\Omega_i^2)$. Introducing the

definition of the safety factor,

$$q = \frac{1}{A}\frac{B_\phi}{B_\theta} = \frac{1}{A}\frac{B_\phi 2\pi a}{\mu_0 I} \quad ,$$

and evaluating the numerical constants in Equation (42) yields

$$\dot{\varphi} = 400\ n_i \langle\sigma v\rangle_{DT} q^2 A^2 I^2\ (MA)\ (1 - F_C)\ \ kV/sec \quad . \qquad (43)$$

Assuming an average ion density $\langle n_i \rangle = 5 \times 10^{13}\ cm^{-3}$, $\langle\sigma v\rangle_{DT}(T_i = 10\ keV) \approx 10^{16}\ cm^3\text{-}sec^{-1}$, $q = 3$ and $A = 4$ results in

$$\dot{\varphi} = 288\ I^2(1 - F_C)\ kV/sec \quad .$$

For the I = 2MA case, Table I in Chapter II shows that, depending on the alpha production profile,

$$0.8 \leq (I - F_C)I^2 \leq 1.9 \quad .$$

The optimistic case of 0.8 yields

$$\dot{\varphi} = 230\ kV/sec \quad .$$

This rate, unimpeded, would result in a plasma potential on the order of the electron temperature (assuming $T_e = 10$ keV) in about 40 milliseconds of operation. Similarly, for the 5 MA case from Table I,

$$0 \leq (1 - F_C)I^2 \leq 5.2 \quad ,$$

which results in a potential buildup ranging from approximately zero to hundreds of kilovolts per second again depending on the exact radial profiles which exist.

The electrostatic arguments were presented above for one reason. All other alpha particle considerations evaluated have produced seemingly tolerable effects. This is not the case with the electrostatic charging problem. Perhaps a rigorous analysis of the implications of and plasma response to this charging will prove it to be benign. However, recall that $E_\alpha \approx 3.5$ MeV and $T_e = T_i \approx 10$ keV so that in general the background plasma will respond to the "alpha driven potential" before the alpha particle orbits themselves are altered appreciably. This suggests that the plasma will adjust perhaps by attracting positive charges from the wall area or in some other way to limit the potential growth.

In any event, detailed research in this area seems warranted. Electric fields have not been included in this orbit analysis. A self-consistent treatment of the three component plasma, including the electric field effects, is not a simple task but, based on these results, one which demands further effort.

E. Conclusions

The distribution functions for 3.5 MeV alpha particles contained by various size systems were calculated in this chapter. The distribution function at a point in space was formed from single particle orbit considerations by integrating the alpha particle source function along the appropriate orbit characteristic numerically.

The alpha particle energy density deposition rate profiles and momentum profiles were calculated from the distribution functions. In the zero Larmour radius case, the alpha particle heating profile is identical to the alpha source distribution profile since, in this

limit, all particles are rigidly confined to their initial flux surface. In the finite Larmour radius cases the alpha heating profiles[35] were found to be reduced near the center of the discharge and increased slightly in the outer plasma regions relative to the source distribution. The I = 2 MA heating profile showed the most pronounced broadening effect relative to the source shape since large orbit excursions permit particles produced near the center of the discharge to heat plasma zones in the peripheral plasma regions. The large excursions also explain the overall decreased magnitude of the I = 2 MA heating profile where as many as 25 percent of the alphas produced are lost from the plasma. In a reactor size plasma, $I \geq 10$ MA, it is found that the heating profile can be taken equal to the alpha particle source profile to a high degree of accuracy.

Although the alpha particles are produced isotropically in velocity space, the toroidal drift affects initially costreaming and counterstreaming particles differently. Overall, counterstreaming particles are preferentially lost from the system due to orbit excursions. As a result, two alpha particle momentum input profiles must be considered. First, on a given flux surface, the fast alpha particle density produced near $\theta = 0$ tends to drive the background plasma in the same direction as the plasma current. When $\theta = \pi$, the momentum input tends to drive the plasma in the opposite direction. Thus, the alphas are directed, on a given flux surface, so as to create a shear flow pattern in the background plasma. However, parallel ion viscosity, which relaxes a toroidal flow velocity inhomogeneity on a flux surface, has a much faster time scale ($\sim \tau_{ii}$) than the buildup time

required for a significant shear flow. Therefore, the momentum input profile on each flux surface was averaged over that flux surface and another shear flow pattern was found. In this case, the toroidal velocity buildup rate is constant on a flux surface but varies from surface to surface. The shear length then is in the radial direction. Perpendicular ion viscosity was found to have a characteristic time too long to relax the buildup of the flow pattern. However, for typical systems with $I \geq 2$ MA, the alpha particle input momentum was shown to be small enough so that, even unimpeded, a buildup time of hundreds of seconds is required before the parallel Kelvin-Helmholtz instability or other known instability thresholds are exceeded. A problem which requires hundreds of seconds of plasma operation to occur should be recognized as a possible problem. Since such a time scale is at least two orders of magnitude longer than those in present day plasmas, the possible intervention of new and as yet unforeseen relaxation mechanisms must be acknowledged.

The alpha particle behavior discussed above poses no problem to plasma operation. However, there is one problem area that was not analyzed rigorously here, but is recommended for further research. The loss of alpha particles from the system due to excursions on orbits which intersect the plasma boundary was considered. Every alpha lost from the system results in an electrostatic charging of magnitude (-2e) to the background plasma. Since the alpha particle energy is about 3.5 MeV, the potential buildup will affect the background plasma before the alpha orbits are altered in general. For feasibility systems, (I = 2-5 MA), potential buildup rates of hundreds of kilovolts per second

are typical. In such cases, less than 100 milliseconds of operation are required to create a potential in excess of the plasma temperature, T_e. The importance of this effect is not predicted in the present work. Rather, it is noted that, except for the electrostatic charging phenomena, alpha particle behavior seems to pose no special concerns and it is recommended that further efforts be focused on this possible problem area.

IV. HEATING A LARGE CTR TOKAMAK BY NEUTRAL BEAM INJECTION*

A. Introductory Remarks

In the previous chapters of this thesis the details of thermonuclear alpha particle production and subsequent heating profiles were analyzed. For large reactor systems it was found that the radial dependence of the energy deposited in the plasma by alpha particles is about the same as that of the alpha production rate due to fusion. The production rate in turn depends on the background plasma characteristics in the system. To complete this work, the alpha particle results obtained thus far are coupled to the background plasma system using a two-fluid, space time numerical model to simulate the plasma behavior. A separate model for neutral beam injection heating of the plasma, described below, is incorporated in the overall simulation which includes neoclassical ion conduction, pseudoclassical electron conduction, radiation losses, ohmic heating, and alpha particle heating.

The startup of a large CTR tokamak plasma at low density is studied using this model. Questions of beam energy deposition profiles, beam energy requirements for neutral penetration into the plasma, and beam power requirements to achieve ignition or prescribed plasma heatup rates are examined. Finally, the energetic response of the background plasma to such injected power levels is determined.

The analysis is primarily for the 5000 MW(th) conceptual fusion reactor system studied at the University of Wisconsin.[10] However, the results are generally applicable to toroidal systems and, wherever possible, implications of the results for other, in particular, smaller reactor size plasmas are indicated. A summary of the characteristics

*[Published: D. G. McAlees, R. W. Conn, Nucl. Fusion 14, 419 (1974)]

of the conceptual reactor, UWMAK-I, pertinent here is given in Appendix B.

B. Plasma Simulation and Neutral Beam Injection Models

The plasma simulation model and method of solution are described in this section. Part of this discussion includes the neutral beam injection model. Several general assumptions applicable to the plasma model are the following: 1) the presence of background neutral gas and impurities in the plasma are not considered; 2) the possibility of a deleterious plasma response due to neutral injection is not included;[21] 3) neoclassical ion transport and pseudoclassical electron transport are the only transport effects examined.[36,37] Possible additional effects on transport, such as trapped particle instabilities, are not studied.[17]

To simulate the time evolution of the plasma parameters during heating, a two-fluid numerical model, accounting for electromagnetic field diffusion and energy flows within the plasma, is used.[38-40] The electron-ion fluid model accounts for diffusion, heat conduction, electron-ion rethermalization, bremsstrahlung and synchrotron radiation, ohmic heating, thermonuclear alpha particle heating and heating by means of injected power. The governing equations for the system are written in cylindrical coordinates and depend only on the minor radius, r, and the time, t. Toroidal transport coefficients, accurate to first order in $\varepsilon = 1/A$, the inverse aspect ratio, are used. The equations are as follows:

1) Particle Conservation:

$$\frac{\partial n}{\partial t} = - \frac{1}{r} \frac{\partial}{\partial r} (rnW_r) + \frac{P(r)}{E_b} \tag{44}$$

where W_r is the radial diffusion velocity, P(r) is the injected power density and E_b is the neutral beam particle energy.

2) Particle Diffusion:

$$nW_r = - D_\perp \frac{\partial n}{\partial r} \tag{45}$$

3) Ion Energy Conservation:

$$\frac{\partial}{\partial t}\left(\frac{3}{2} nT_i\right) = 4.77 \times 10^{-12}\left(\frac{T_e - T_i}{T_e^{3/2}}\right) n^2 Z_i^2 \frac{\ell n \Lambda}{A_i}$$

$$- \frac{1}{r} \frac{\partial}{\partial r} \left(r \left\{\frac{3}{2} nW_r T_i + Q_i\right\}\right)$$

$$+ \frac{n^2}{4} \langle \sigma v \rangle_{DT} E_\alpha f_{\alpha i} + P(r) f_{bi} \tag{46}$$

$$Q_i = - \kappa_i \frac{\partial T_i}{\partial r} \tag{47}$$

where Q_i is the ion heat flux and f_{bi} is the fraction of beam power absorbed by the ions.

4) Electron Energy Conservation:

$$\frac{\partial}{\partial t}\left(\frac{3}{2} nT_e\right) = - 4.77 \times 10^{-12} \frac{(T_e - T_i)}{T_e^{3/2}} \frac{n^2 Z_i^2 \ell n \Lambda}{A_i}$$

$$- \frac{1}{r} \frac{\partial}{\partial r} \left(r \left[\frac{3}{2} nW_r T_e + Q_e\right]\right) + \frac{n^2}{4} \langle \sigma v \rangle_{DT} E_\alpha f_{\alpha e} + 6.25 \times 10^{14} E_\phi J_\phi +$$

$$+ P(r)f_{be} - P_{brem} - P_{sync} \tag{48}$$

$$Q_e = - \kappa_e \frac{\partial T_e}{\partial r} \tag{49}$$

$$P_{brem} = 9.48 \times 10^{-17} Z_i^2 n^2 T_e^{1/2} \tag{50}$$

$$P_{sync} = 4.0 \times 10^{-12} B_\phi^{5/2} (1 - R)^{1/2} n^{1/2} T_e^2 \quad . \tag{51}$$

Q_e is the electron heat flow, f_{be} is the fraction of beam energy absorbed by the electrons and R is the wall reflectivity to the synchrotron radiation. Equations (45), (47), and (49) signify that a diagonal simulation model is being used. Cross flow terms, such as particle flow due to temperature gradients, which are expected on general grounds[41] are not included. P_{brem} and P_{sync} represent energy losses from bremsstrahlung[42] and synchrotron[43] radiation, respectively.

The first term on the right hand side of Equations (46) and (48) accounts for electron-ion rethermalization and $P(r)f_{bi}$ and $P(r)f_{be}$ are external sources of energy for the ions and electrons, respectively. Also E_α = 3.5 MeV is the energy of the alpha particle produced in a D-T fusion reaction, $f_{\alpha i}$ and $f_{\alpha e}$ are the fractions of the alpha energy deposited in the ions and electrons, respectively.[44] The form of the particle and energy source terms due to neutral beam injection will be developed below.

5) Electromagnetic Equations:

$$\frac{\partial B_\theta}{\partial t} = 10^5 \frac{\partial E_\phi}{\partial r} \tag{52}$$

$$\frac{\partial J_\phi}{\partial t} = 8 \times 10^4 \frac{1}{r} \frac{\partial}{\partial r} \left(r \frac{\partial E_\phi}{\partial r}\right); \; E_\phi = \eta J_\phi . \tag{53}$$

In Equations (44) to (53), lengths are in cm, time in milliseconds, density is in cm^{-3}, temperature and energy are in eV, current density is in amps/cm^2, electric fields are in volts/cm, and magnetic fields are in gauss.

Considerable theoretical work has been done in deriving transport theories for toroidal plasmas. It is still uncertain which theory describes present day experiments and whether or not direct scaling of any existing theory to large plasmas is appropriate. In this analysis, the electron heat conduction coefficient is assumed pseudoclassical[36,37] and the ion heat conduction coefficient is taken as the banana regime of neoclassical theory.[41] The particle confinement time may be estimated by $\tau_p \approx a^2/4D_\perp$. Based on the initial plasma conditions and taking $D_\perp$ to be pseudoclassical, typical particle confinement times are found to be greater than 50 seconds. The time scale for heating the plasma is expected to be on the order of 10 seconds or less so that particle diffusion during the heating phase is negligible. Therefore, the particle diffusion coefficient, $D_\perp$, can be assumed zero for the large plasmas studied here. The plasma density profile changes during heating only as a result of the addition of plasma particles by neutral injection. The transport coefficients used in the numerical simulation are given by

$$\varkappa_i = 0.68\, \varepsilon^{1/2}\, \rho_{i\theta}^2\, n\nu_i \tag{54}$$

$$\varkappa_e = 10\, n\nu_e\, \rho_{e\theta}^2 \tag{55}$$

$$D_\perp \approx 0 \quad . \tag{56}$$

The forms of bremsstrahlung and synchrotron radiation loss terms and the electrical resistivity are those of Rose and Clark,[42] Rosenbluth,[43] and Spitzer,[45] respectively. A reflection coefficient of 0.9 is assumed in the case of synchrotron radiation. Equations (46) and (48) include terms representing the energy deposited in the plasma by alpha particles produced in deuterium-tritium fusion events.

The equations for the model are nonlinear coupled differential equations and require linearization of the transport coefficients. Following linearization, an implicit finite difference method[46] is used to obtain the time dependent radial profiles. Details of the numerical solution method are given by Dory and Widner.[39]

The neutral beam heating phase of reactor startup is assumed to follow initial gas breakdown and the time during which the plasma current rises to its final operating value. During the beam heating phase, the plasma current remains fixed and the core flux is increased to make up for the resistive drop as the plasma temperature increases. Thus, the times to ignition given in the next section refer strictly to the beam heating phase and do not include the current rise time. (The current rise time in tokamak reactors may be long because of the large energy stored in the fields of the ohmic heating and divertor coils.[10])

The analysis here begins with a fully ionized plasma characterized by the following relatively flat radially dependent profiles:

$$T_i(r, t = 0) = T_{i0}(1 - r^2/a^2)^{1/3} + 10 \text{ eV}, \quad T_{i0} = 500 \text{ eV}$$

$$T_e(r, t = 0) = T_{e0}(1 - r^2/a^2)^{1/3} + 10 \text{ eV}, \quad T_{e0} = 500 \text{ eV}$$

$$n(r, t = 0) = n_0(1 - .95\ r^2/a^2)^{1/2}, \quad n_0 = 3 \times 10^{13}/cm^3$$

$$J_\phi(r, t = 0) = J_0(1 - r^2/a^2)^{1/2}, \quad J_0 = 40.2\ amps/cm^2$$

$$E_\phi(r, t = 0) = \eta J_\phi(r, t = 0).$$

The initial temperature profiles are assumed relatively flat because the conceptual reactor, UWMAK-I, is proposed to operate with an axisymmetric, poloidal field divertor. The action of the divertor should mean that a relatively rarefied zone, dominated by atomic processes, will surround the plasma outside the separatrix. The 10 eV temperature is inserted to indicate the presence of this blanket plasma. The initial density profile assumed is also relatively flat and the factor .95 means the density on the edge will be roughly 20 percent of the center line density. The boundary temperature has been varied from 10 eV to 100 eV and both the shape of the density profile and the density of the plasma at the edge have been varied. It is found that the plasma heatup rates are basically not affected by these changes. Note also that absorption of synchrotron radiation by the cold plasma surrounding the hot plasma core is neglected.[47] On the other hand, beam penetration is dependent on the density profile. Actual beam power deposition profiles for different density profiles will be examined below. Finally, the safety factor q(a) is set at 1.75 and the initial profiles are consistent with $q > 1$ at all plasma radii.

The energetic neutral beam injected into the plasma is assumed to be composed of deuterium-tritium neutrals of atomic mass 2.5. A single

equivalent atom beam of zero cross sectional area (pencil beam) is considered. In practice, the required total power would be injected by several neutral beams located around the torus to minimize the disturbance of axisymmetry in the plasma. In this work, aimed at determining the plasma response to neutral beam injection, the pencil beam approximation has been used. Recently, Rome, Callen and Clarke[48] have studied the injected energy density deposition rate profiles which result from finite beams. Using the computer code developed in their work, it is found that the pencil beam approximation is accurate except in the region near the plasma center. For the system studied here, the pencil beam and finite beam give essentially the same results for $r/a \geq 0.15$. In addition, the time required to heat the plasma to ignition is not sensitive to the detailed injected energy profile near $r = 0$ since the toroidal plasma volumes in this region are small.

The neutral beam strength is defined in equivalent amperes by

$$I = P_T/E_b \tag{57}$$

where P_T is the beam power in watts and E_b is the beam particle energy in electron volts. The number of particles injected into the plasma per second, I/e, where e is the electron charge, is accounted for in Equation (44).

The neutral beam particles are ionized in the plasma primarily by electron and ion impact and by charge exchange.[49] The optimum choice for the angle of injection is not clear. However, injection nearly perpendicular to the toroidal field will result in fast ion production on trapped particle orbits. This trapped ion specie may

support trapped particle instabilities and a distributed charge distribution in the plasma which could cause plasma rotation.[33] Therefore, tangential injection has been analyzed. The geometry for neutral beam injection tangent to the center of the cross section is shown on Fig. 22. For a neutral current, I_0, entering the plasma the attenuation of the beam as a function of distance along the injection chord is given by

$$I(s) = I_0 \, e^{-\int_0^s n(s')\sigma_T \, ds'} \tag{58}$$

where

$$\sigma_T = \sigma_{cx} + \sigma_i + \frac{\langle \sigma v \rangle}{v_0} \quad . \tag{59}$$

σ_{cx} is the charge exchange cross section, σ_i is the ion impact cross section, $\frac{\langle \sigma v \rangle}{v_0}$ is the Maxwellian averaged electron impact cross section, v_0 is the neutral particle velocity and s is the distance along the chord. It is assumed that the cross sections are functions of the relative velocity of the colliding species only. For the beam energies examined in this work ($E_b \geq 100$ keV), ion and electron impact ionization are dominant and charge exchange is small. Thus, neutral injection is not a source of warm neutrals as it can be in present injection experiments. Numerical values of the cross sections are given in References 49. and 50. The approximation to the data given by Sweetman[51] and shown on Fig. 23 is used here. In the worst case, equivalent to a 200 keV hydrogen neutral, the error introduced by this fit to the attenuation cross section is 25 percent.

The drift orbits of the fast ions produced as the neutrals are ionized must be considered in determining the energy density deposition

rate in the plasma. It has been shown that ions produced parallel to the magnetic field follow orbits which are approximately circular and centered at $x = x_s$ when projected onto a plane containing the plasma cross section.[1,48] The stagnation distance, x_s, is defined by

$$x_s \approx \frac{qmv_\phi}{zeB_\phi} \tag{60}$$

and for 500 keV injected ions, the center of the orbit is $x_s \approx 7$ cm in a system the size of UWMAK-I. Since x_s is less than 7 cm for injection energies less than 500 keV, this small shift in the orbit center is neglected. Thus, the fast ions resulting from injection are assumed to traverse circular orbits centered at $r = 0$.

The fast ion slowing down time, as for the alpha particles, is short compared with the particle confinement time so that it is assumed that the ions deposit their energy instantaneously over the flux surface on which they are produced. The radial shape of the energy density deposition rate for a particular beam energy is calculated numerically using the attenuation and orbit considerations just outlined and the assumed plasma density profile. In addition, the total beam power has a radial distribution in the plasma. Therefore, the total power deposited is defined as

$$P_T = 2\pi R_0 \int_0^a 2\pi r \, P_0 f(r) dr \quad , \tag{61}$$

where $P(r) = P_0 f(r)$ is the energy density deposition rate profile, P_0 is the power density at $r = 0$, and $f(r)$ is the radial shape factor for a beam of energy E_b. The shape factor $f(r)$ is calculated numerically and is included in Equations (46) and (48) in this manner.

In a large plasma governed by the transport laws assumed, the time scale for rethermalization between plasma electrons and ions is small compared to the plasma heating time. Therefore, the heating times calculated are not sensitive to the exact fraction of the injection energy absorbed by each plasma specie as the fast ions slow down. It has been assumed that 70 percent of the injected energy is absorbed by the electrons in all cases considered.

C. Plasma Heating Due to Neutral Beam Injection and Alpha Particle Production

The characteristics of the reactor size plasma studied here are given in Appendix B. The approach of the plasma toward thermal equilibrium considering only ohmic heating and no beam heating has been calculated for a ten second time interval. The peak ion temperature as a function of time is given on Fig. 24. Using the Spitzer formula for electrical resistivity, ohmic heating alone is not sufficient to ignite the system. Using the notation, $T(r,t)$, note that $T_i(0,\infty)$ is less than 3 keV. Further, since the temperature rise due to ohmic heating is a relatively slow process, there is no advantage in delaying injection heating until the ohmic heating phase has concluded. Therefore, injection heating will begin immediately after the plasma current has been fully established, i.e., $t = 0$ with respect to the heating phase.

The neutral beam energy and power that are required to ignite such a reactor size plasma are now considered. Clearly, the beam must be energetic enough to adequately penetrate the plasma before ionization occurs. On the other hand, the beam energy is bounded from above by

requiring that a large fraction of the injected neutral particles be trapped in the plasma. In large systems, such as UWMAK-I, this maximum energy requirement is really inconsequential since trapping of the injected neutrals is highly efficient.

Since the plasma is quite large in this system, it is ignited at low density, $n_0 = 3 \times 10^{13}$ cm^{-3}, to improve beam penetration. It is assumed that subsequent fueling after ignition can build the plasma density to a desired operating value. In addition to the penetration problem, the stored energy in the hot, dense operating plasma is very high, on the order of 1000 MJ. Therefore, it is advantageous to ignite the system at a lower stored energy. Stix[1] and Gerard, Khallidi, and Marty[52] have come to the same conclusion based on similar considerations. By heating the plasma to a temperature above the ignition temperature, the stored energy will increase further due to thermonuclear power and fueling can then be accomplished by alternate means.[53]

The radial shapes of the power density deposited in the plasma from 100, 350, and 500 keV beams are shown on Fig. 25. The shape factors are independent of the total power in the beams and are normalized to 1.0 at the radius of maximum deposition. The fractions of the 100, 350, 500 keV beams trapped in the plasma are $> .999$, $> .999$, and $> .995$, respectively. The effect of different density profiles for the 350 keV beam is shown on Fig. 26. It is clear that the most concave density profile gives the most peaked power deposition profile. However, the plasma heating rate and the time to ignition are only slightly affected by these profile changes.

Since plasma heating at a density below that desired during the burn is considered, there is interest in both igniting the plasma and perhaps, more importantly, in achieving a prescribed heatup rate to allow for subsequent fueling and density buildup. A rigorous monitor of plasma behavior relevant to ignition and heatup is the plasma stored energy, W, defined as

$$W(t) = \int_0^t (P_\alpha + P_{OH} + P_{INJ} - P_L)dt' . \tag{62}$$

Here P_α, P_{OH}, and P_{INJ} are the powers due to alpha particles, ohmic heating and injection, respectively, and P_L is the total power loss from the plasma volume. The rate of change of the stored energy is

$$\frac{dW(t)}{dt} = P_\alpha + P_{OH} + P_{INJ} - P_L \quad . \tag{63}$$

From Equation (63) note that W will increase without injection if

$$P_\alpha + P_{OH} > P_L \quad . \tag{64}$$

This condition, $P_\alpha + P_{OH} > P_L$, can occur at low temperature when the plasma approaches a thermal equilibrium maintained by ohmic heating. It also occurs at a higher temperature when the power deposition from alpha heating becomes dominant and the plasma ignites. As the plasma approaches the lower temperature equilibrium, the stored energy is increasing, but dW/dt is decreasing so that d^2W/dt^2 is negative. This equilibrium point is thermally stable, i.e., stable against excursions in plasma temperature. On the other hand, if beam heating is used until d^2W/dt^2 becomes positive, the plasma will have reached the higher temperature, thermally unstable, ignition point and will have ignited.

Once d^2W/dt^2 is positive, the plasma will have a positive heatup rate even if beam heating is discontinued. The reason is the second derivative,

$$\frac{d^2W}{dt^2} = \frac{d}{dT}\,(P_{OH} + P_\alpha - P_L)\,\frac{dT}{dt} \quad , \tag{65}$$

can be positive only when P_α is dominant since $\frac{d}{dT}\,(P_{OH} - P_L)$ is negative and $\frac{dT}{dt}$ is positive. Therefore, assuming constant injection power, the ignition condition is

$$\frac{d^2W}{dt^2} > 0 \quad .$$

At the time of ignition, injection can be discontinued and the plasma will heat up at an accelerating rate.

Figure 27 illustrates these points by showing the heating rates resulting from 75 MW of injection for 5 seconds and for three different beam energies. In all cases, the plasma is ignited in less than 5 seconds. Ignition occurs where dW/dt is a minimum. The discontinuities in dW/dt shown on Fig. 27 occur when injection is terminated after 5 seconds and the subsequent increase in stored energy is due to P_{OH} and P_α only since $P_{INJ} = 0$. When the beams are turned off at t = 5 sec, the 500 keV case exhibits the fastest heatup rate, approximately 6.8 MJ/sec. However, the 100 keV beam has been more efficient in heating the plasma than the 350 keV beam. When the beams are turned off, the 100 keV case gives a heating rate of 5.9 MJ/sec compared to 2.3 MJ/sec from the 350 keV beams. The reasons for this difference can be understood by examining the ion temperature profiles on Figs. 28, 29 and 30. Note first that injection of 500 keV beams for 5

seconds produces high ion temperatures in the central zone of the plasma. Therefore, the production rate of alpha particles is also high in this zone and the result is an appreciable total alpha power production. In the 100 keV case, the maximum ion temperatures are lower and occur near the plasma edge. However, the plasma volume associated with the high temperature zone is greater than for the 500 keV beam case. As such, the total alpha power produced is again appreciable. The 350 keV neutral beam is calculated to produce a relatively uniform ion temperature profile. However, the temperature level of approximately 6 keV means the total alpha power produced is, in fact, less than in each of the previous two cases. The result is the low heatup rate of 2.3 MJ/sec once injection is terminated. It is concluded that the plasma heatup rate resulting from injection at constant power for a specific length of time depends on the ion temperature profiles established in the plasma. This in turn is clearly a function of the beam energy.

Turning to another point, Fig. 31 illustrates the effects of using different beam powers at a given beam energy. The calculations were for 10 seconds of neutral beam injection in both cases. For 25 MW of 500 keV beams, the plasma barely ignites and d^2W/dt^2 is positive but small. The heatup rate is thus also small. On the other hand, 50 MW of power produces a heatup rate of approximately 24 MJ/sec. This can be compared to the 75 MW, 500 keV, 5 second injection case shown on Fig. 27 where the heatup rate at the end of injection is 6.8 MJ/sec. A cross comparison of Figs. 27 and 31 indicates, for various beam energies and different beam powers, the time required to ignite the plasma and the heatup rates which result from injection times in the

5 to 10 second range.

Some further comments should be made on the temperature profiles shown on Figs. 28, 29 and 30. In the 100 keV case, shown on Fig. 28, the beam energy is too low to penetrate the plasma appreciably. The injected power is therefore deposited in the outer plasma regions. Yet even with the steep temperature gradients that develop, energy transport from large to small plasma radii is too slow to cause a significant temperature increase at the plasma center. The implication is that for large plasmas operating at low q values, and governed by the transport coefficients assumed here, the plasma energy balance is local. That is, two adjacent volumes of plasma are only weakly coupled energetically. As such, the plasma temperature profile can be expected to follow the injected power profile.

The strongly inverted temperature profiles in the 100 keV beam case are similar to profiles predicted to develop from skin currents and may have adverse effects on plasma confinement. The questions of plasma equilibrium and stability are not investigated here. Rather, the beam energy necessary to produce temperature profiles with $\frac{\partial T}{\partial r} \leq 0$ at all r has been determined. The injection profile for a 350 keV beam does not have a local peak off axis as is seen in Fig. 25, case (b). The temperature response to a 75 MW, 350 keV neutral beam has been computed and the profiles are given on Fig. 29. As with the 100 keV beam, though to a lesser extent, the temperature profiles are locally peaked off axis even though the injected energy density deposition rate is maximum on axis and is monotonically decreasing to r = a. This result is clarified by considering Fig. 32.

Figure 32 shows the 350 keV injection case renormalized on a power deposited per plasma particle basis. Since the plasma density decreases monotonically with radius, the 350 keV beam produces a heating rate (as opposed to an energy density deposition rate) which is a maximum on axis, but is also locally peaked near the plasma boundary. Therefore, even a constant power density input can result in preferential heating off axis because the plasma density decreases with radius.

A 500 keV beam does yield plasma temperature profiles in this reactor size plasma that are not inverted. Yet this energy is less than the approximately 1 MeV beams previously suggested to achieve adequate penetration in a somewhat smaller toroidal plasma.[49] A lower beam energy is acceptable here for three reasons: 1) a low density startup is used, (3×10^{13} cm^{-3} vs. 3×10^{14} cm^{-3} as used in Reference 49.); 2) the density profile is included in the calculation; and 3) the variation with radius of the plasma volume per radial increment along the tangential injection path shown on Fig. 22 is included. The temperature response to 75 MW of 500 keV beam particles is shown in Fig. 30. Again, injection heating is discontinued in the calculations after 5 seconds.

The use of 75 MW of neutral beam power gives examples of fast plasma heating and thus rapid startups. Since the burn time for reactors may be long (approximately 5400 seconds for the reactor studied in Reference 10.), a slower startup is acceptable. A slower startup may also be desirable since there is a trade-off between the time to ignition and the power required. Figure 33 shows the power required for ignition as a function of the time to ignition using 500 keV beams.

Even a long startup (for example, the 15 MW case) requires only about 10 seconds. Depending on the additional time required to increase the density and temperature to operating conditions after ignition, the time for ignition can be shortened by increasing the beam power.

D. Implications of Results for Other Devices

This work has concentrated on the neutral beam heating of the large, power producing conceptual reactor, UWMAK-I, outlined in Appendix B. Further, the reasons that the neutral beam energy and power required to ignite the plasma depend directly on the detailed plasma characteristics and profile shapes have been indicated. To determine how these results scale with system size, a system with a plasma radius of 2 meters, a major radius of 5.2 meters and otherwise identical to the reference conceptual design, UWMAK-I, in toroidal field strength, safety factor, profile shapes, and so on, was analyzed. To obtain the same injected power deposition profile as in the 500 keV case studied above, a/λ_0 must be the same in both cases. a/λ_0 is the ratio of plasma radius to the mean free path of the injected neutrals at the peak plasma density (cf. Fig. 23). The required beam energy in the 2 meter system is approximately 200 keV. Figure 34 shows the power required to ignite this smaller system as a function of the time to ignition using a 200 keV neutral beam. In both the case of UWMAK-I and the system with a 2 meter plasma radius, the beam energy required may be reduced in two ways. First, for calculational convenience, it was assumed that the injected neutral has an atomic mass of 2.5. The total attenuation cross section for the neutral beam is a function of the relative velocity of the beam

particles and the background plasma. For the same relative velocity, the beam energy required varies linearly with mass. Therefore, the minimum energy required is reduced by 20 percent if a pure deuterium neutral beam is used. Second, as pointed out in Reference 48., the beam can be injected inside the geometric center of the plasma cross section, which results in a shorter chord length to the plasma center. Changing the injection angle requires consideration of the finite size of the beam to be certain the beam does not intersect the torus inner wall. Also, additional analysis of the orbits of ions produced at large pitch angles is required.

E. Conclusions

The analysis reported in the preceding sections, based on pseudo-classical scaling for the electron conductivity and neoclassical scaling for the ion conductivity, indicates that large tokamak plasmas can be ignited at low density ($\sim 3 \times 10^{13}$ particles/cm^3) using moderate levels of neutral beam power and beam energies of several hundred keV. For a reactor size plasma with a minor radius of 5 meters and characteristic parameters as listed in Appendix B, a 500 keV beam is adequate to provide the injected power deposition and heating rate profiles that ignite the plasma and yield non-inverted temperature profiles. Lower beam energies can also yield injected power deposition profiles that are peaked on axis. However, the heating rate in the plasma causes local maxima to occur in the temperature profiles in the outer zones of the plasma. This is found in the analysis of smaller systems as well. The maxima develop because the injected power deposited per plasma particle depends on the density profile. For a scaled down machine with

a = 200 cm and the same aspect ratio, 200 keV gives results similar to the 500 keV beam in the larger system.

A low density startup is used because beam penetration is enhanced while plasma losses are reduced. Therefore, a large system can be ignited in reasonably short times. For example, in the conceptual UWMAK-I system studied here, power levels on the order of 50 MW give ignition times in the 2 to 10 second range. In smaller feasibility or reactor size plasmas, such as the a = 200 cm system, approximately 10 MW of beam power is sufficient to ignite the system in about 2 seconds with 200 keV beams.

The times to ignite reactor size plasmas using a given beam power are found to be about the same where beam energies are in the range from 100 keV to 500 keV (A_i = 2.5). However, the final heatup rate of the plasma is sensitive to beam energy when a given power is injected for a fixed length of time. In particular, it was found that lower energy, less penetrating neutral beams can actually produce faster plasma heating rates in some cases.

Finally, note that the time scale for heat conduction using pseudoclassical and/or neoclassical transport coefficients is long in a large plasma compared with heating times of several seconds. As such, thermal diffusion does not effectively suppress the local maxima in the temperature profiles which are reported here. For the same reason, adjacent volumes of plasma are found to be very weakly coupled, from an energy viewpoint, so that electron and ion temperatures are approximately equal throughout the beam heating phase.

V. SUMMARY

Detailed conclusions derived from this work were presented at the end of each chapter in the text. This summary includes an abbreviated collection of those results and conclusions.

The analysis of the details of 3.5 MeV alpha particle orbits in a tokamak showed that, due to finite gyro-radius effects, alpha particle drift orbits can deviate substantially from their corresponding flux surfaces. In cases where the plasma current is greater than 10 MA, the usual small gyro-radius expansion procedure can be used to treat the orbit effects. Using the orbit model and procedures developed, alpha particle containment characteristics, momentum input profiles and their implications and electrostatic charging which results from alpha losses were computed. For a constant plasma current profile, numerical results for the fraction of alpha particles contained by various size systems show that reactor size plasmas ($I \geq 10$ MA) provide very efficient containment. Feasibility size plasmas ($I = 2$-5 MA) contain $\gtrsim$ 75 percent of the alpha particles produced depending on the precise parameter profiles assumed. Alpha containment improves with increased aspect ratio and more steeply peaked plasma current density profiles as well as increased plasma current.

The alpha particle loss analysis showed a preferential loss of initially counterstreaming ($\vec{v}_{\|} \cdot \vec{J} < 0$) particles which implies a net momentum input to the background plasma. The fast alpha particle distribution functions for particles contained by the system were constructed by integrating the alpha source along orbit characteristics numerically. The alpha particle heating profiles and momentum input

profiles were obtained from the distribution functions.

The heating profile for the I = 2 MA case was found to be reduced in magnitude and broadened radially compared to the alpha source strength and radial dependence assumed. These results reflect the large gyro-orbit effects which lead to large orbit excursions, significant particle loss from the system and the broadened profile for contained alphas. These effects are less pronounced for I = 5 MA and when I $\geq$ 10 MA they can be neglected and heating and production profiles can be assumed identical to a high degree of accuracy.

The alpha particles represent a momentum source to the background plasma. The momentum input profiles found are such as to drive inhomogeneities in the toroidal flow velocity imparted to the background particles. The inhomogeneities occur on a given flux surface and from flux surface to flux surface. On a given flux surface, the action of parallel ion viscosity is sufficiently rapid so that the relaxation mechanism limits the maximum velocity inhomogeneities to acceptable levels relative to known instability thresholds. Similarly, the radial shear flow pattern buildup is of no immediate concern since hundreds of seconds are required before toroidal flow velocity inhomogeneities approach known stability thresholds.

There is one problem area that was not analyzed in detail here, but is recommended for further consideration. The loss of an alpha particle from the system results in an electrostatic charge of magnitude (-2e) to the background plasma. Since the alpha energy is 3.5 MeV the electrostatic potential buildup will affect the background particles before the alpha orbits are altered in general. For

feasibility plasmas (I = 2-5 MA) potential buildup rates of hundreds of kilovolts per second are typical. As such, plasma potentials greater than the electron temperature occur after ~ 100 milliseconds of operation. In high current devices, where the fraction of alpha particles contained approaches 1.0, this problem will not occur. However, the potential buildup problem is extremely sensitive to the alpha containment properties of a system and it is recommended that further consideration be given to the plasma response to this source of potential.

Using the alpha particle energy deposition rate profile results and similar energy deposition rate profiles determined from a separate model for neutral beam injection, the ignition phase of startup for a large tokamak plasma was studied. It was found that large plasmas can be ignited at low density (~ 3×10^{13} cm^{-3}) using moderate levels of neutral beam power and beam energies of several hundred kilovolts. For the University of Wisconsin UWMAK-I conceptual reactor (a = 5 meters), power levels on the order of 50 MW give ignition times in the 2 to 10 second range. A beam energy of 500 keV is adequate to provide injected power deposition and heating rate profiles that ignite the plasma and yield temperature profiles such that $\frac{\partial T}{\partial r} \leq 0$ at all r. Lower beam energies (~ 100 to 350 keV) ignite the plasma in approximately the same time for the same injected power, but local maxima occur in the temperature profiles in the outer zones of plasma. Although the energy density deposition rate profiles are peaked on axis and decrease monotonically with radius for some lower energy cases, the corresponding plasma heating profiles depend on the energy deposited per background

plasma particle which in turn can lead to a local maxima in the resulting temperature profiles.

The times required to ignite reactor size plasmas using a given beam power are found to be about the same where beam energies are in the range from 100 to 500 keV ($A_i \approx 2.5$). The final heatup rate of the plasma, however, is sensitive to beam energy when a given power is injected for a fixed length of time. In fact, it was found that lower energy, less penetrating neutral beams can actually produce faster plasma heating rates in some cases. This effect demonstrates the importance of assessing the plasma response to neutral beam injection.

APPENDIX A

Details of τ_b Singularities

In Chapter III the integrability of singularities which exist in the integrand of the τ_b integral were briefly discussed. Here it is illustrated in more detail under what conditions non-integrable ($\tau_b \Longrightarrow \infty$) singularities are possible.

Throughout the discussions of trapped particles the conventional definition of a trapped particle was used, i.e., a particle for which $v_{||} = 0$ at some point along the particle orbit. In the case of the zero Larmour radius approximation, the point at which $v_{||} = 0$ defines the banana tip or turning point of the orbit. Thus, when $v_{||}$ reverses sign, physically the particle reverses its direction and returns along its previous path.

In systems where finite gyro-radius effects cannot be neglected, a distinction must be made between the $v_{||} = 0$ point and the orbit turning point. On Fig. A-1 this difference is shown. The figure shows two alpha particle orbits, both originating at x/a = 0.5, y/a = 0.0 with pitch angles of Cos χ = 0.43 and 0.45. Initially $v_{||} > 0$ in both cases. For the Cos χ = 0.43 orbit, $v_{||} = 0$ at the point along the orbit marked by x. Note, however, a finite path length is required for the orbit to turn and change direction in the cross section view. Since the drift velocity is not zero when $v_{||} = 0$, the guiding center motion continues and the particle moves approximately vertically. However, as $v_{||}$ increases, but now in the counterstreaming direction, the motion along the field line and the drift motion are oppositely directed. If $v_{||}$

becomes large enough to dominate the guiding center motion before the particle crosses the horizontal axis, the turning point shown on Fig. A-1 develops. If, on the other hand, $v_{||}$ does not increase appreciably after the $v_{||} = 0$ point, the drift motion continues to dominate the overall particle motion and no turning point occurs. Detail A on Fig. A-1 shows the $v_{||} = 0$ points by x for several different orbits characterized by initial pitch angle, Cos χ. For Cos $\chi = 0.431$, $v_{||} = 0$ at the point shown, but note that no turning point develops. As Cos χ decreases, or the pitch angle itself increases, both a $v_{||} = 0$ and a turning point occur.

In the case of zero Larmour radius, the $v_{||} = 0$ and turning points are identical. For the pitch angle which results in a turning point location exactly on the horizontal axis, a barely trapped particle orbit occurs which physically marks the boundary in pitch angle space between trapped-untrapped particle orbits. It is this precise orbit which yields a logarithmic singularity in the τ_b integral so that $\tau_b \Longrightarrow \infty$.

The equivalent situation arises in finite Larmour radius cases if the turning point occurs on the horizontal axis. Physically, the drift motion and motion along the field line cancel precisely at such a point so that the particle approaches it for an infinite time. Mathematically, consider the orbit equation,

$$y^2(x) = C - x^2 - P\sqrt{(x - x_T)(x + A)} \quad ,$$

and assume that the turning point occurs on the x-axis at x_p. Near the turning point,

$$x = x_p - \Delta \quad ,$$

and using an expansion process the same as that in Chapter III, except here $y(x_p) \cong 0$,

$$y(x) = \sqrt{\Delta}\left[2x_p + \frac{P}{2}\frac{2x_p - x_T + A}{\sqrt{(x_p - x_T)(x_p + A)}}\right]^{1/2} + 0(\Delta) \cdots$$

Since the τ_b integrand is proportional to $1/y(x)$ and $1/\sqrt{\Delta}$ is integrable, the occurrence of a non-integrable singularity requires the coefficient of $\sqrt{\Delta}$ to be zero, i.e.,

$$2x_p = -\frac{P}{2}\frac{2x_p - x_T + A}{\sqrt{(x_p - x_T)(x_p + A)}} \quad . \tag{A1}$$

Finally, it will be shown that this condition occurs when the drift motion and motion along the field line cancel exactly. This is possible only when $y/a = 0.0$ since the direction of the drift velocity is $\pm$ y. For a particle with $v_{\|} < 0$, which is the case for the particles shown on detail A near $y/a = 0.0$, motion along the field line is in the downward direction. Drift motion is upward. Thus, when

$$\frac{m}{2eB_{\phi_0}R_0}\left(v_{\|}^2 + \frac{v_{\perp}^2}{2}\right) = \frac{|v_{\|}|B_\theta(r)}{B_{\phi_0}} \quad , \tag{A2}$$

the two motions are equal and in opposite directions. Since

$$P = \frac{2qv}{\Omega a} = \left(\frac{2v}{a}\right)\left(\frac{1}{A}\frac{B_{\phi_0}}{B_\theta(a)}\right)\left(\frac{m}{2eB_{\phi_0}}\right) \quad ,$$

and

$$v^2 = v_{\|}^2 + v_{\perp}^2 \quad ,$$

Equation (A2) yields

$$\frac{P}{4}\left(\frac{v_{\|}^2}{v^2} + \frac{v^2}{v^2}\right) = \frac{|v_{\|}|}{v} \quad r \quad , \tag{A3}$$

where all lengths are relative to the plasma radius, a. From the conservation of μ,

$$v^2(A + x_T) = (v^2 - v_{\|}^2)(A + x) \quad ,$$

so that Equation (A3) becomes

$$\frac{P}{4}\left(2 - \frac{A + x_T}{A + x}\right) = \sqrt{1 - \frac{A + x_T}{A + x}} \quad r \quad .$$

Upon rearranging the terms of this equation,

$$\frac{P}{2} \frac{2x + A - x_T}{\sqrt{(A + x)(x - x_T)}} = 2r \quad . \tag{A4}$$

It was assumed that the two motions cancel when $v_{\|} < 0$ (counterstreaming portion of the orbit) so that the point where the cancellation occurs must be for $x < 0$. Thus, in Equation (A4), $r = -x$ so that r will be positive as required. Changing variable x to x_p results in the final form of Equation (A4) given by

$$2x_p = -\frac{P}{2} \frac{2x_p - x_T + A}{\sqrt{(x_p - x_T)(x_p + A)}} \quad , \tag{A5}$$

which is identical to Equation (A1).

This exercise indicates that when the turning point, not the $v_{\|} = 0$ point, is located exactly on the horizontal axis, a non-integrable singularity occurs. Figure A-2 shows the initially trapped orbit for the same spatial conditions as above, but in a device where

I = 5 MA. In this case, although $v_{||} = 0$ at x_T along the orbit, no turning points occur due to the high drift velocities and location of x_T. Equation (A5) cannot be satisfied for any initial pitch angle conditions by costreaming particles produced at x/a = 0.5, y/a = 0.0, I = 5 MA. This is consistent with Fig. 13 which shows finite bounce times for all I = 5 MA costreaming particles.

In summary, $\tau_b \Longrightarrow \infty$ is the result of an orbit turning point which is located on the horizontal mid-plane of the plasma cross section. At this point guiding center motion along the field line and drift motion can cancel exactly. Whether or not such a point develops depends on the location of the $v_{||} = 0$ point, x_T, and the plasma current, I, which is related to the magnitude of the drift speed. From Equation (A5), assuming $x_T \approx x_p$, the requirement for a non-integrable singularity is approximately

$$P \leq \frac{4|x_T|\sqrt{x_p - x_T}}{\sqrt{(A - x_T)}} \quad . \tag{A6}$$

From Fig. A-1,

$$(x_p - x_T) \approx 0.02 \quad ,$$

and estimates of what minimum plasma current levels yield non-integrable singularities for costreaming particles as a function of x_T can be made. Results are shown in Table A-1.

TABLE A-1

Approximate Current Level Required for $\tau_b \Longrightarrow \infty$ vs. x_T

(Costreaming Particles)

x_T	P	I (MA)
0	0	∞
-.1	.03	23
-.2	.06	11
-.3	.09	7.6
-.4	.11	5.7
-.5	.15	4.5

These results agree with Figs. A-1 and A-2. From Fig. A-1, I = 10 MA, $x_T \approx -0.3$ and a non-integrable singularity occurs as it should since $10 > 7.6$ MA. From Fig. A-2, I = 5 MA, $x_T \approx -0.15$ and only integrable singularities occur since the $\tau_b \Longrightarrow \infty$ requirement in this case is $I \geq 17$ MA whereas the actual current is I = 5 MA.

APPENDIX B

Characteristics of the University of Wisconsin Conceptual Fusion Reactor UWMAK-I

This appendix lists a more inclusive, though by no means complete, set of parameters characterizing the UWMAK-I conceptual tokamak fusion reactor studied at the University of Wisconsin.[10] In particular, the discussion is limited primarily to those parameters that describe the plasma and magnets.

The primary operating characteristics of UWMAK-I are:

Power	5000 MW(th); 1500 MW(e)
Fuel Cycle	(D-T), Li
Plasma Radius	5 m
Major Radius	13 m
Divertor	Poloidal, Double Neutral Point
Coolant	Lithium
Structural Material	316 Stainless Steel
Neutron Wall Loading	1.25 MW/m^2
Toroidal Magnetic Field	B_ϕ = 38.2 kG on axis
	B_ϕ^{max} = 86.6 kG at magnet
Magnets	Superconductor, NbTi
	Stabilizer, Cu
Power Cycle	Li-Steam

The main plasma characteristics which describe UWMAK-I during the beam heating phase of startup are:

Plasma Density	3×10^{13} cm^{-3} on axis
Safety Factor	$q(a) = 1.75$
	$q(0) > 1$
Plasma Current	I = 21 MA

The plasma characteristics which describe UWMAK-I during the operating phase are:

Poloidal Beta	$\beta_\theta = 1.08$
Toroidal Beta	$\beta_\phi = 0.05$
Safety Factor	$q(a) = 1.75$; $q(0) > 1$
Toroidal Magnetic Field	38.2 kG on axis
Plasma Current	21 MA
Ion Temperature	11 keV
Electron Temperature	11 keV
(D+T) Ion Density	0.8×10^{14}/cm^3
Alpha Density	0.03×10^{14}/cm^3
Particle Confinement Time	14 seconds
Fractional Burnup	7.2%
Burn Time	90 minutes

UWMAK-I is designed to operate with a poloidal, double-neutral point divertor which produces a low density, essentially insulating zone, around the plasma. As such, the temperature profile during the burn time is expected to be relatively flat, whereas the density profile has been taken as $n(r) = n_0(1 - .99\ r^2/a^2)^{1/2}$. Further design details are given in Reference 10.

REFERENCES

1. T. H. Stix, Plasma Physics 14, (1972) 367.
2. R. Dei-Cas, et al., "The Neutral Injection Heating into the Fontenay-aux-Roses Tokamak," Paper E9, Third Intl. Symposium on Toroidal Plasma Confinement, Max-Planck Institut fur Plasma Physik, Garching (1973).
3. L. D. Stewart, et al., "Neutral Beam Injection Heating of ORMAK," Paper E12, Third Intl. Symposium on Toroidal Plasma Confinement, Max-Planck Institut fur Plasma Physik, Garching (1973).
4. D. Aldcroft, et al., Nucl. Fusion 13, (1973) 393.
5. K. Bol, et al., Proc. Sixth European Conf. on Controlled Fusion and Plasma Physics, Moscow, (1973), Vol. II (to be published).
6. J. Sheffield, et al., Ibid.
7. C. F. Barnett, et al., Ibid.
8. P. N. Haubenreich and M. Roberts, editors, "ORMAK F/BX, A Tokamak Fusion Test Reactor," Oak Ridge National Laboratory Report, ORNL-TM-4634, (June 1974).
9. A similar fusion test reactor conceptual design study including high energy neutral beams was performed by Princeton Plasma Physics Laboratory/Westinghouse Electric Corporation, (June 1974).
10. B. Badger, et al., "Wisconsin Tokamak Reactor Design UWMAK-I," University of Wisconsin Fusion Design Memo 68, Nucl. Eng. Dept., University of Wisconsin, Madison (November 1973), Vol. I.
11. S. A. Morozov and L. S. Solovyev, Dokl. Akad. Nauk. SSSR 128, (1959) 506. [Translation: Soviet Phys. Dokl. 4, (1960) 1031.]

REFERENCES (Continued)

12. J. D. Callen, private communication.

13. J. D. Callen and R. A. Dory, Phys. Fluids 15, (1972) 1523. (Additional references are cited herein.)

14. V. D. Shafranov, Reviews of Plasma Physics, edited by M. A. Leontovich, Consultants Bureau, New York (1966), Vol. 2, p. 103.

15. Georg Knorr, Phys. Fluids 8, (1965) 1334.

16. A. A. Galeev and R. Z. Sagdeev, Soviet Physics JETP 26, (1968) 233.

17. B. B. Kadomtsev and O. P. Pogutse, Nucl. Fusion 11, (1971) 67.

18. Note that $P \approx 2x_s/a$ where x_s is the stagnation distance often used in neutral injection work. See J. A. Rome, et al., Nucl. Fusion 14, (1974) 141.

19. D. L. Jassby and H. P. Furth, "Fusion-Reaction-Injected and Neutral-Beam-Injected Suprathermal Ions in the Tokamak," Princeton Plasma Physics Tech. Memo TM-271, (January 1974).

20. D. G. McAlees, J. D. Callen, J. A. Rome, "Simulation of Alpha-Particle Effects in a Burning D-T Plasma with Fast Ions," Oak Ridge National Laboratory ORMAK F/BX Design Memo No. 22 (January 1974).

21. Plasma perturbations due to neutral beam injection are similar to those expected from alpha particles. See J. D. Callen, et al., "The Theory of Neutral Beam Injection into a Tokamak," Paper E14, Third Intl. Symposium on Toroidal Plasma Confinement, Max-Planck Institut fur Plasma Physik, Garching (1973).

22. J. G. Cordey and M. J. Houghton, Nucl. Fusion 13, (1973) 215.

23. S. T. Butler and M. J. Buckingham, Physical Review 126, (1962) 1.

REFERENCES (Continued)

24. C. L. Hedrick, private communication.

25. Handbook of Mathematical Functions, AMS 55, edited by M. Abramowitz and I. A. Stegun, U. S. Dept. of Commerce, National Bureau of Standards Applied Mathematics, Series 55.

26. P. C. Clemmow and J. P. Dougherty, Electrodynamics of Particles and Plasmas, Addison-Wesley Publishing Co., (1969) Chapter 7.

27. J. D. Callen, unpublished notes on the use of the method of characteristics as applied to neutral beam injection problems.

28. G. I. Bell and S. Glasstone, Nuclear Reactor Theory, Van Nostrand Reinhold Co., New York (1970). This reference provides a physical interpretation of the method of characteristics as applied to solving the neutron transport equation.

29. R. D. Hazeltine, Plasma Physics 15, (1973) 77.

30. J. A. Rome, et al., Proc. of Theoretical Aspects of Cont. Thermonuclear Research, Berkeley, California (1974) 75.

31. J. A. Rome, et al., to be published.

32. See for example: M. N. Rosenbluth, et al., Plasma Physics and Cont. Fusion Research, IAEA, Vienna (1971) 495; J. D. Callen, et al., Paper E14, Third Intl. Symposium on Toroidal Plasma Confinement, Max-Planck Institut fur Plasma Physik, Garching (1973); M. N. Rosenbluth, Bull. Am. Phys. Soc. 18, (1973) 1337; D. J. Sigmar and J. F. Clarke, Oak Ridge National Laboratory Report, ORNL-TM-4606, (June 1974).

33. M. N. Rosenbluth, et al., Plasma Physics and Cont. Fusion Research, IAEA, Vienna (1971) 495.

REFERENCES (Continued)

34. P. J. Catto, et al., Phys. Fluids 16, (1973) 1719.

35. T. E. Stringer, Plasma Physics 16, (1974) 651. In this reference alpha particle orbits and heating profile broadening are treated in less detail. Also, D. G. McAlees and H. K. Forsen, Bull. Am. Phys. Soc. 18, (1973) 1305 discussed alpha particle orbit details and finite gyro-radius effects previously.

36. S. Yoshikawa, Phys. Fluids 13, (1970) 2300.

37. L. A. Artsimovich, Soviet Physics JETP Ltrs. 13, (1971) 70.

38. The computer simulation model used herein was developed from the model discussed in references 39. and 40.

39. R. A. Dory and M. M. Widner, Bull. Am. Phys. Soc. 11, (1970) 1418. Also see Oak Ridge National Laboratory Report, ORNL-TM-3498, (July 1971).

40. J. T. Hogan and R. A. Dory, Proc. Fifth European Conf. on Controlled Fusion, Grenoble (1972), Vol.I , p. 40.

41. M. N. Rosenbluth, R. D. Hazeltine and F. L. Hinton, Phys. Fluids 15, (1972) 116.

42. D. J. Rose and M. Clark, Jr., Plasmas and Controlled Fusion, second revised printing, M.I.T. Press, Cambridge, Mass. (1965).

43. M. N. Rosenbluth, Nucl. Fusion 10, (1970) 340.

44. D. J. Sigmar and G. Joyce, Nucl. Fusion 11, (1971) 447.

45. L. Spitzer, Jr., Physics of Fully Ionized Gases, second revised edition, Interscience Publishers, New York (1967).

46. R. D. Richtmyer and K. W. Morton, Difference Methods for Initial Value Problems, second revised edition, Interscience Publishers,

REFERENCES (Continued)

New York (1967).

47. H. K. Forsen and J. C. Sprott, Nucl. Fusion 12,(1972) 126.

48. J. A. Rome, et al., Nucl. Fusion 14,(1974) 141.

49. A. C. Rivere, Nucl. Fusion 13, (1971) 367.

50. W. Lotz, Astrophys. Journal, Suppl. No. 129, XIV (1967) 207.

51. D. R. Sweetman, Nucl. Fusion 13,(1973) 157.

52. J. P. Girard, et al., Nucl. Fusion 13,(1973) 685.

53. For example, using pellet injection to increase density to a desired operating value. See S. L. Gralnick, Nucl. Fusion 13, (1973) 703.

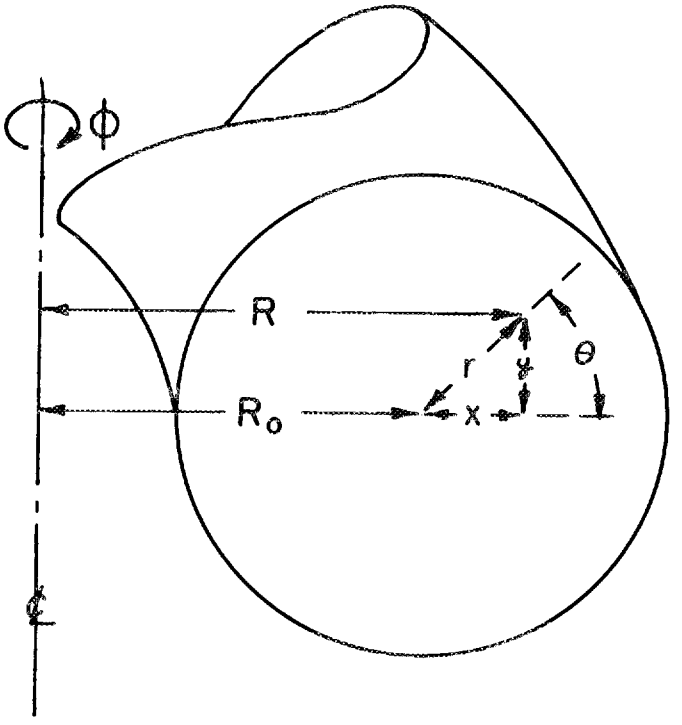

PLASMA CROSS SECTION VIEW
SHOWING COORDINATES

Figure 1

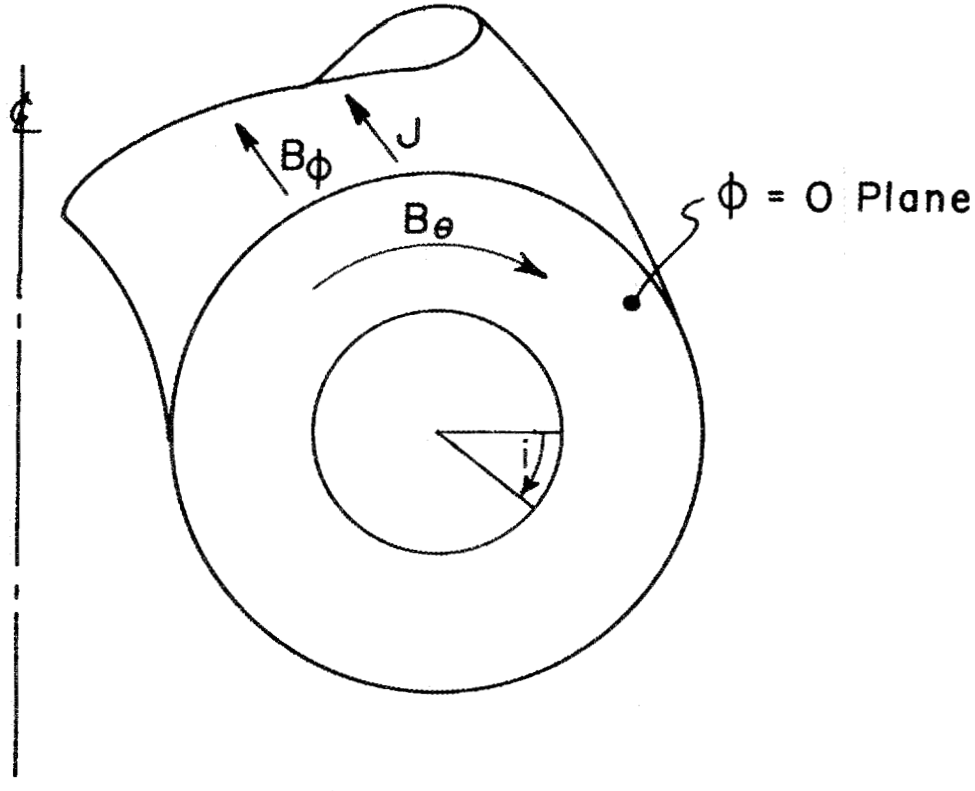

PLASMA CROSS SECTION VIEW
SHOWING PREFERRED FIELD DIRECTIONS

Figure 2

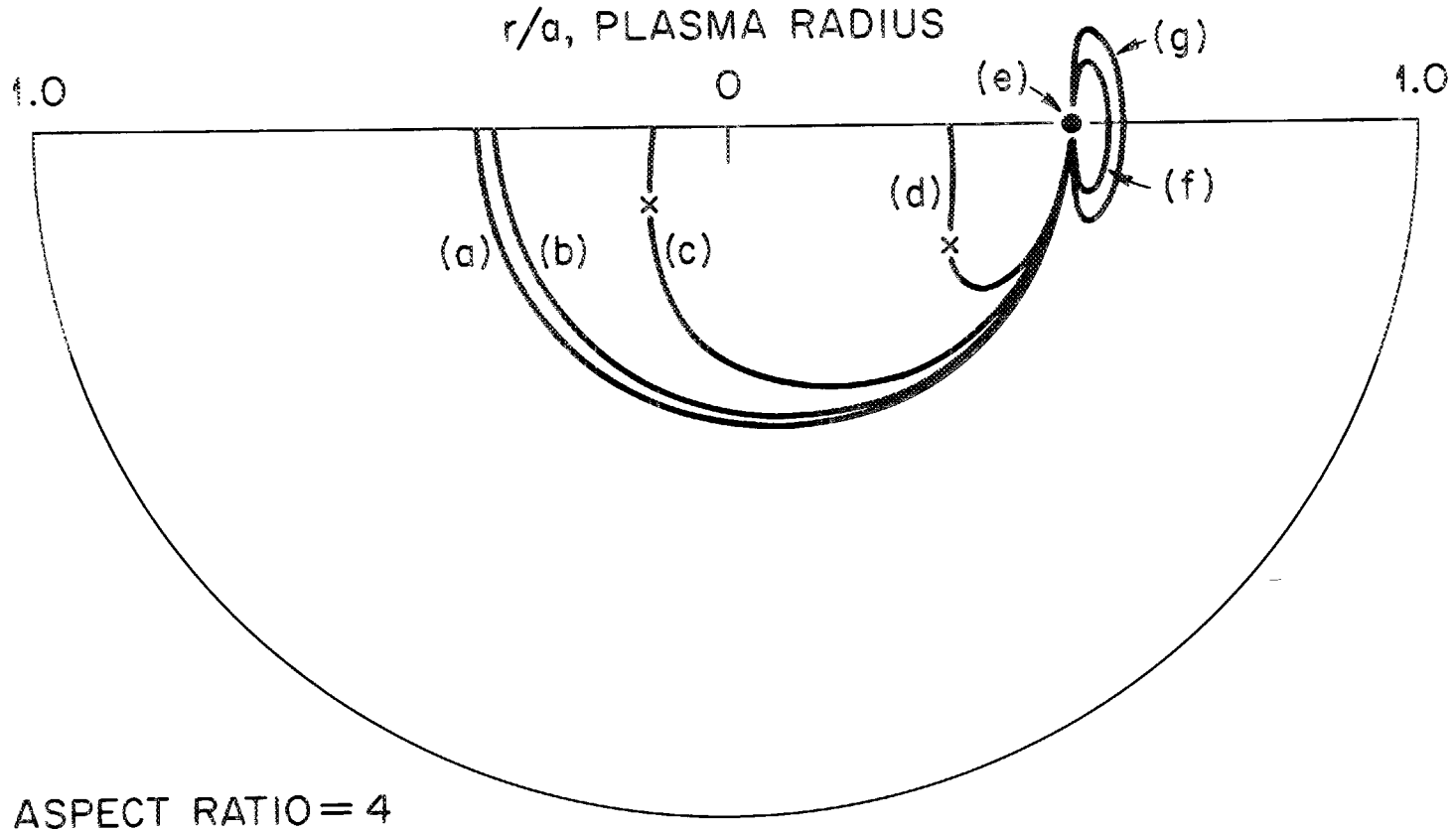

Plasma Cross Section.

Figure 3

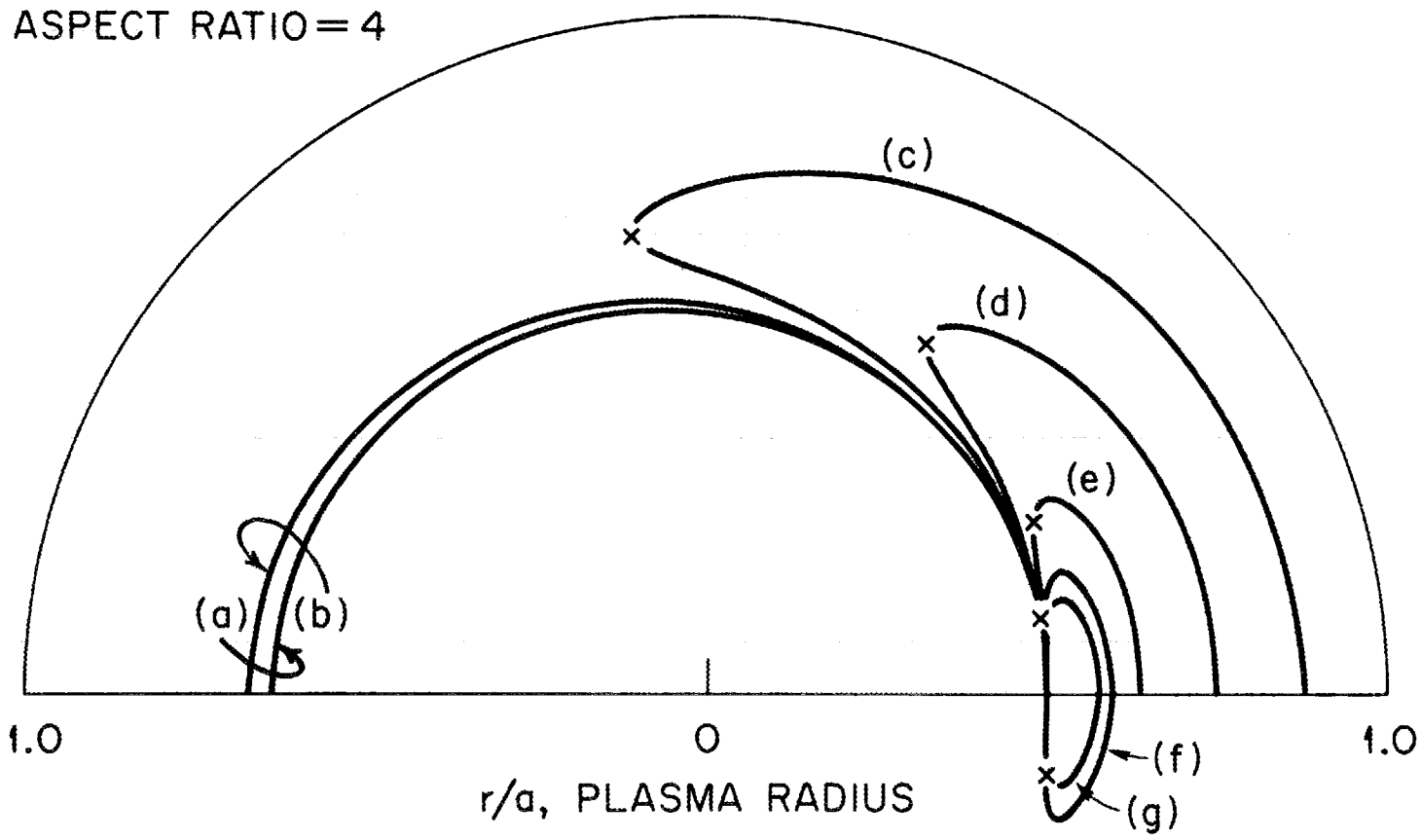

Plasma Cross Section.

Figure 4

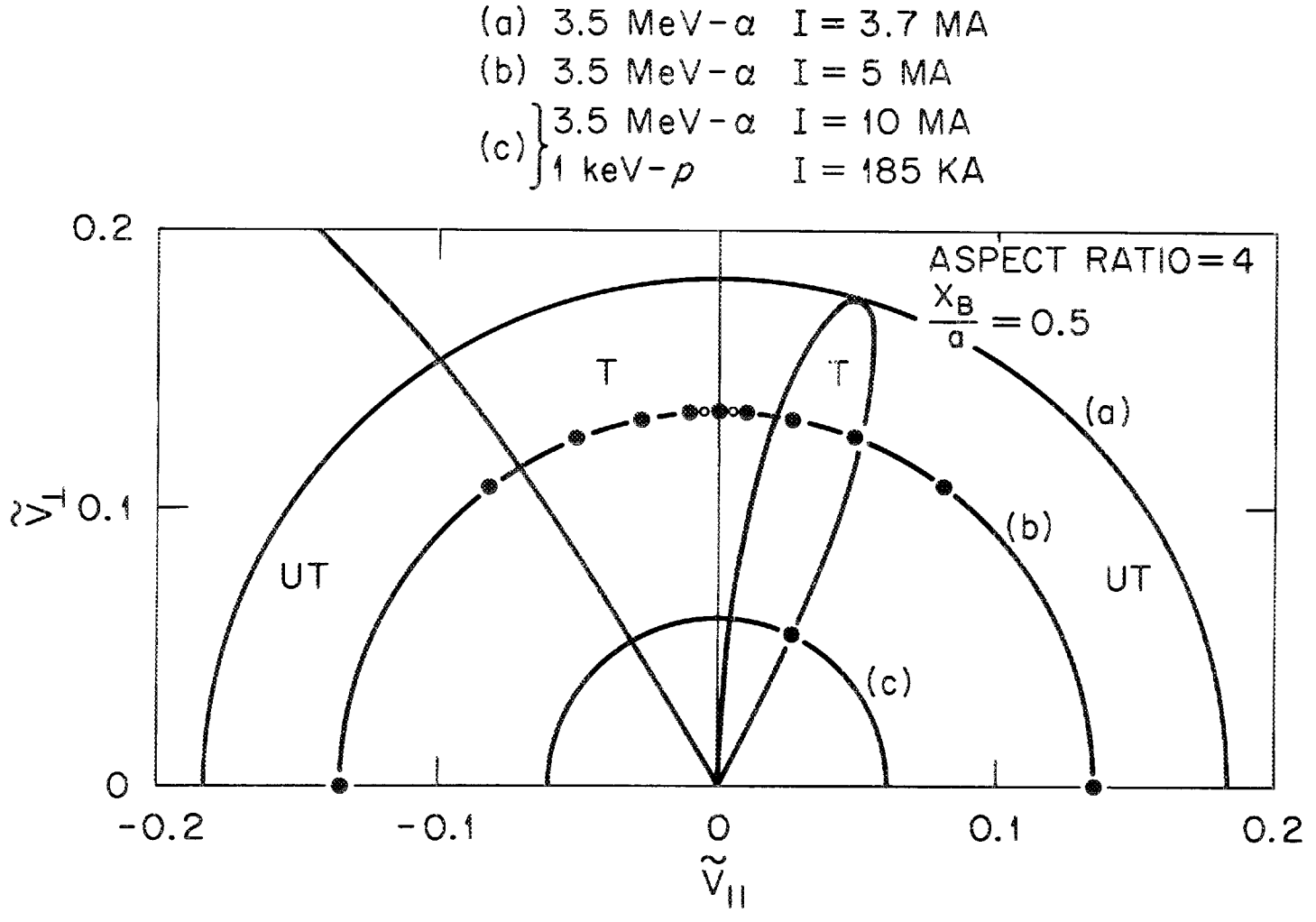
(a) 3.5 MeV-α I = 3.7 MA
(b) 3.5 MeV-α I = 5 MA
(c) 3.5 MeV-α I = 10 MA
(c) 1 keV-p I = 185 KA
ASPECT RATIO=4
$\frac{X_B}{a} = 0.5$
T
T
(a)
(b)
(c)
UT
UT
0.2
0.1
0
-0.2
-0.1
0
0.1
0.2
$\tilde{V}_\perp$
$\tilde{V}_{||}$

Figure 5

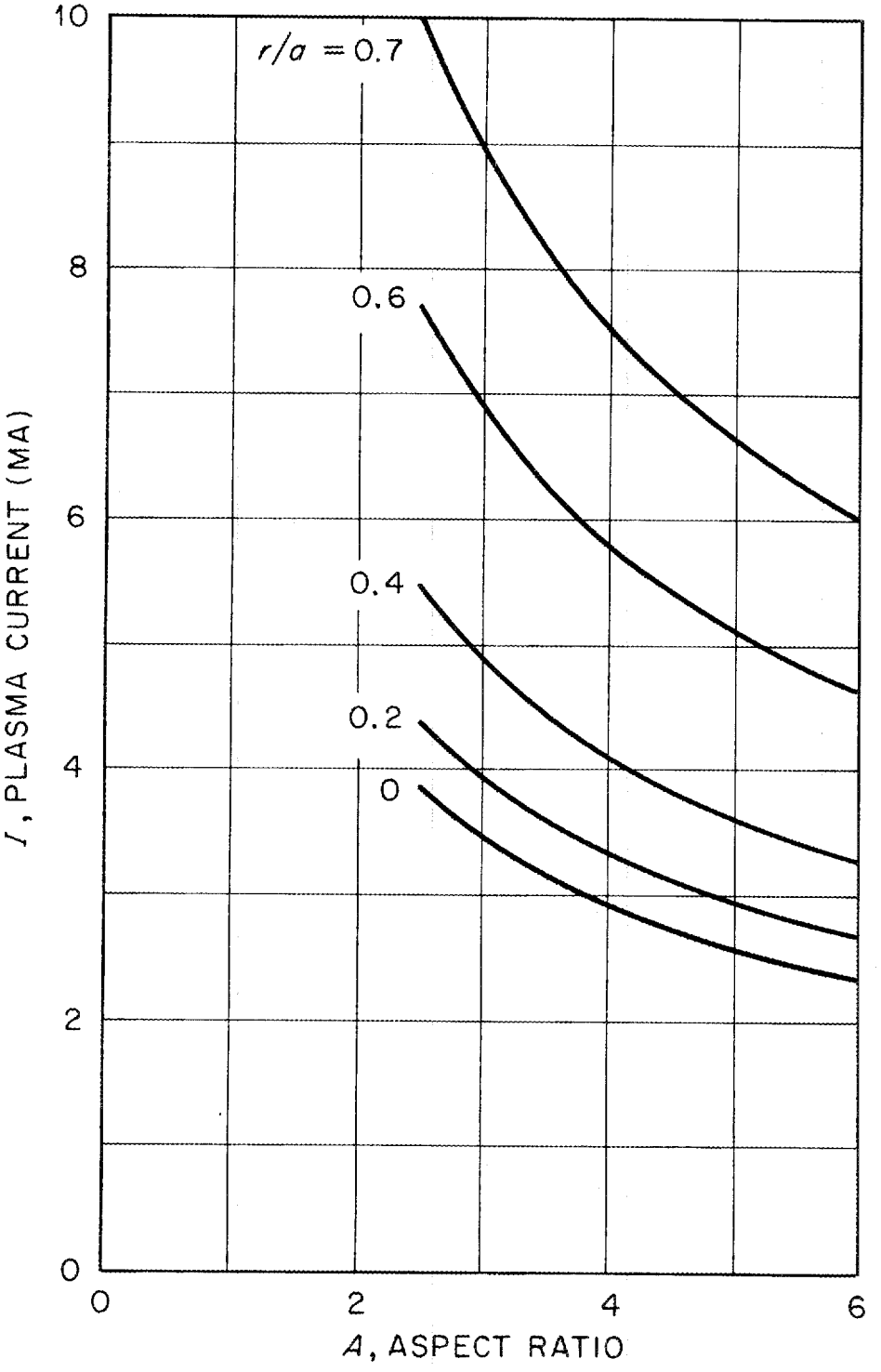
10
8
6
4
2
0
r/a = 0.7
0.6
0.4
0.2
0
0
2
4
6
I, PLASMA CURRENT (MA)
A, ASPECT RATIO

Figure 6

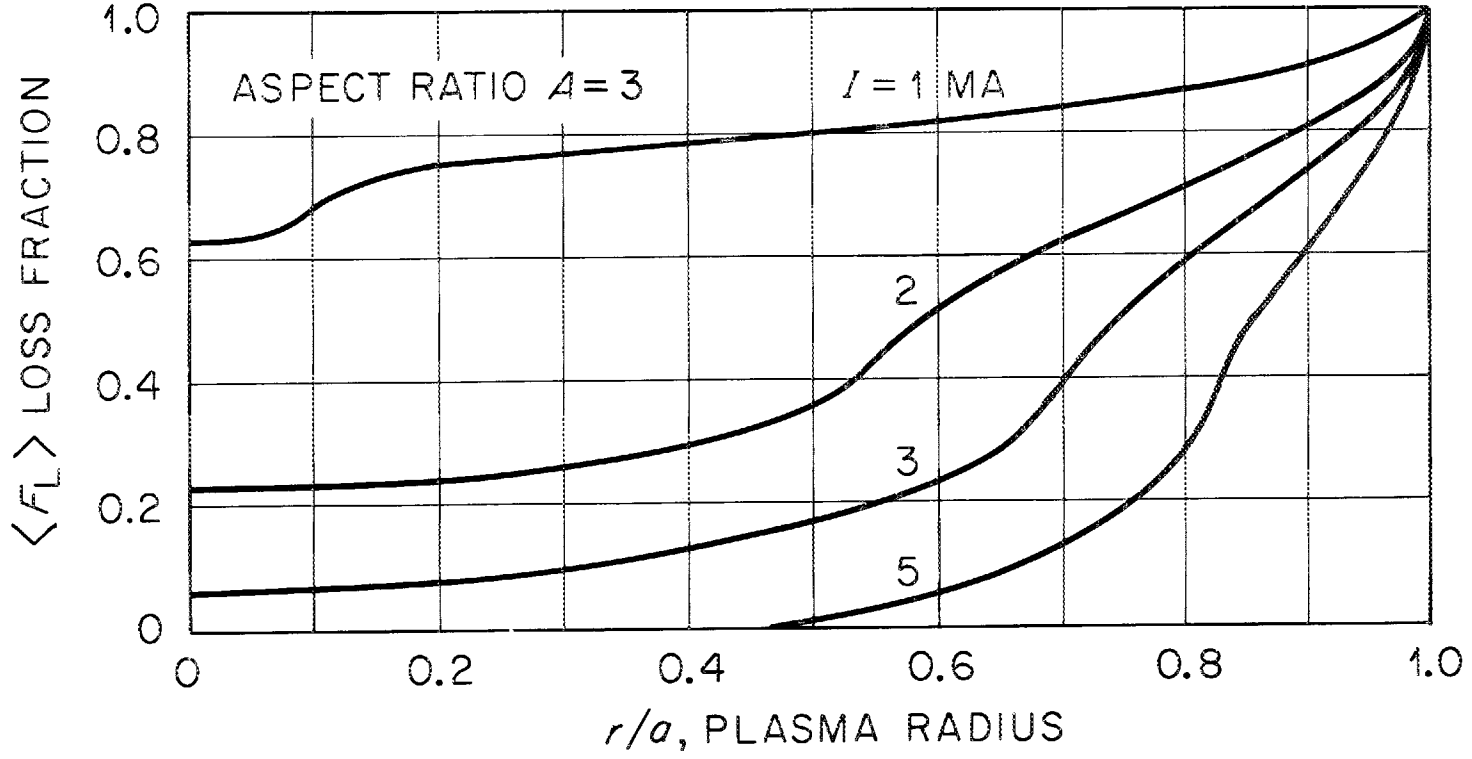
ASPECT RATIO A = 3
I = 1 MA
2
3
5
1.0
0.8
0.6
0.4
0.2
0
0
0.2
0.4
0.6
0.8
1.0
⟨F_L⟩ LOSS FRACTION
r/a, PLASMA RADIUS

Figure 7

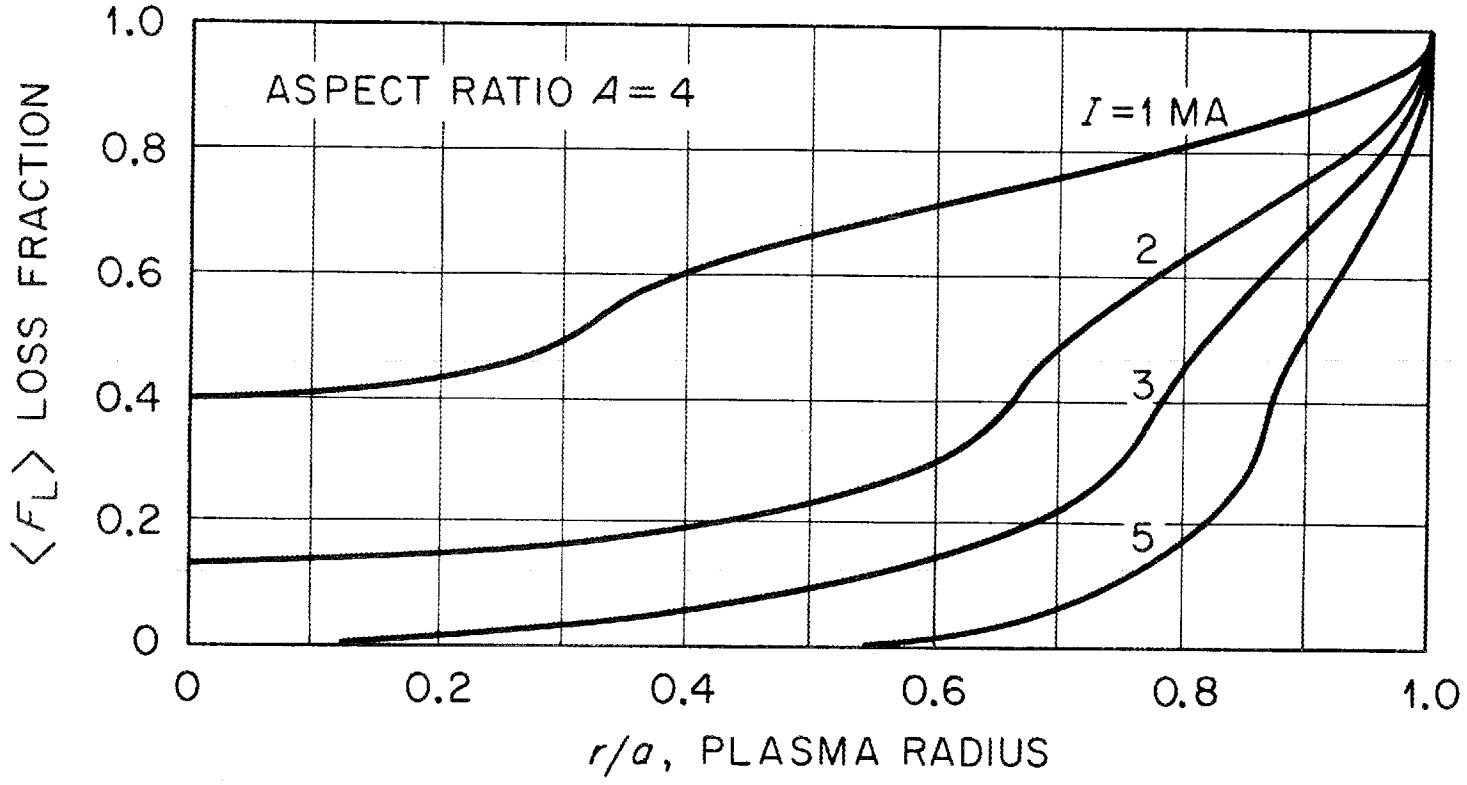
ASPECT RATIO A = 4
I = 1 MA
2
3
5
⟨F_L⟩ LOSS FRACTION
1.0
0.8
0.6
0.4
0.2
0
0
0.2
0.4
0.6
0.8
1.0
r/a, PLASMA RADIUS

Figure 8

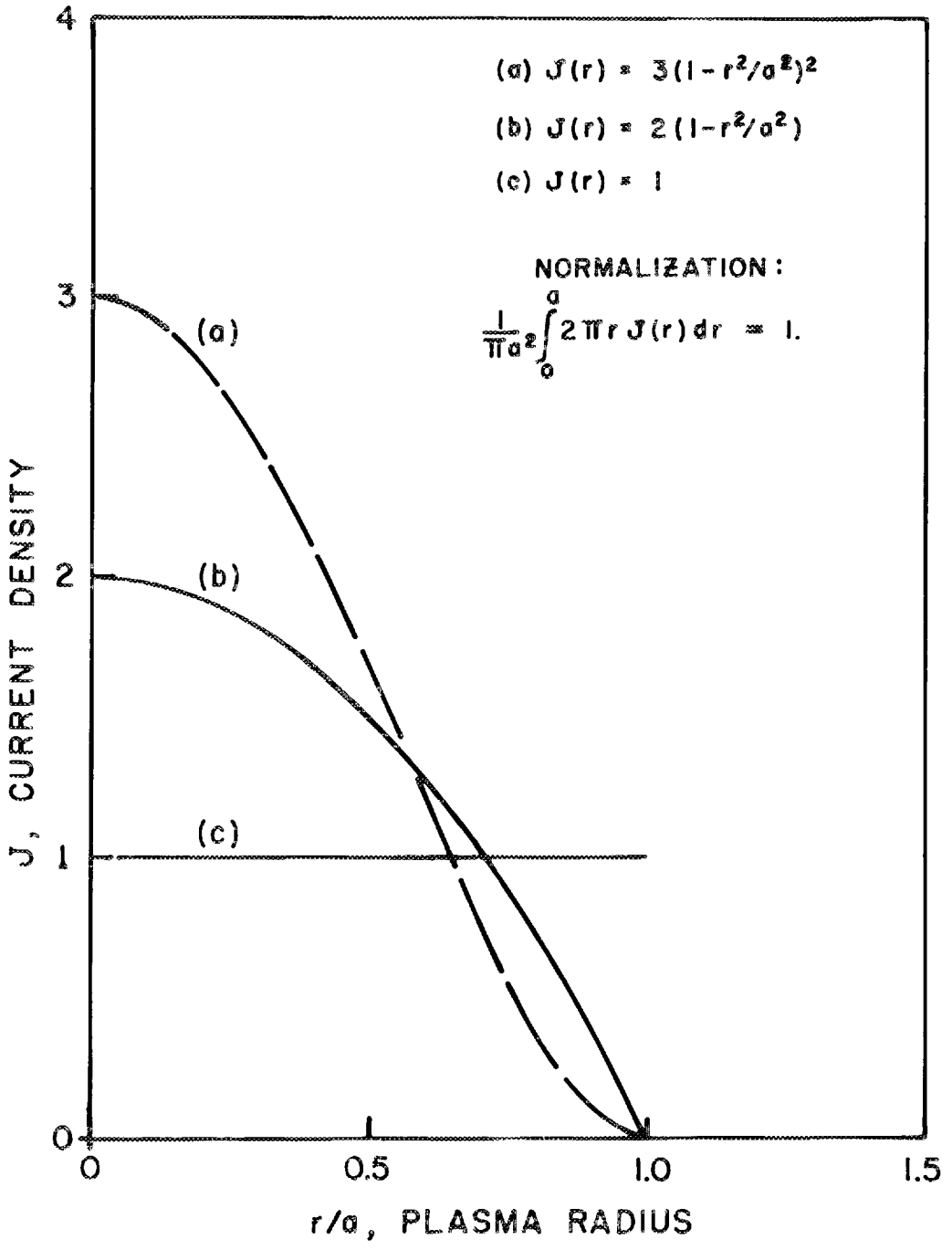
(a) J(r) = 3(1-r²/a²)²
(b) J(r) = 2(1-r²/a²)
(c) J(r) = 1
NORMALIZATION:
$\frac{1}{\pi a^2}\int_0^a 2\pi r J(r)\,dr = 1.$
(a)
(b)
(c)
J, CURRENT DENSITY
r/a, PLASMA RADIUS
0
1
2
3
4
0
0.5
1.0
1.5

Figure 9

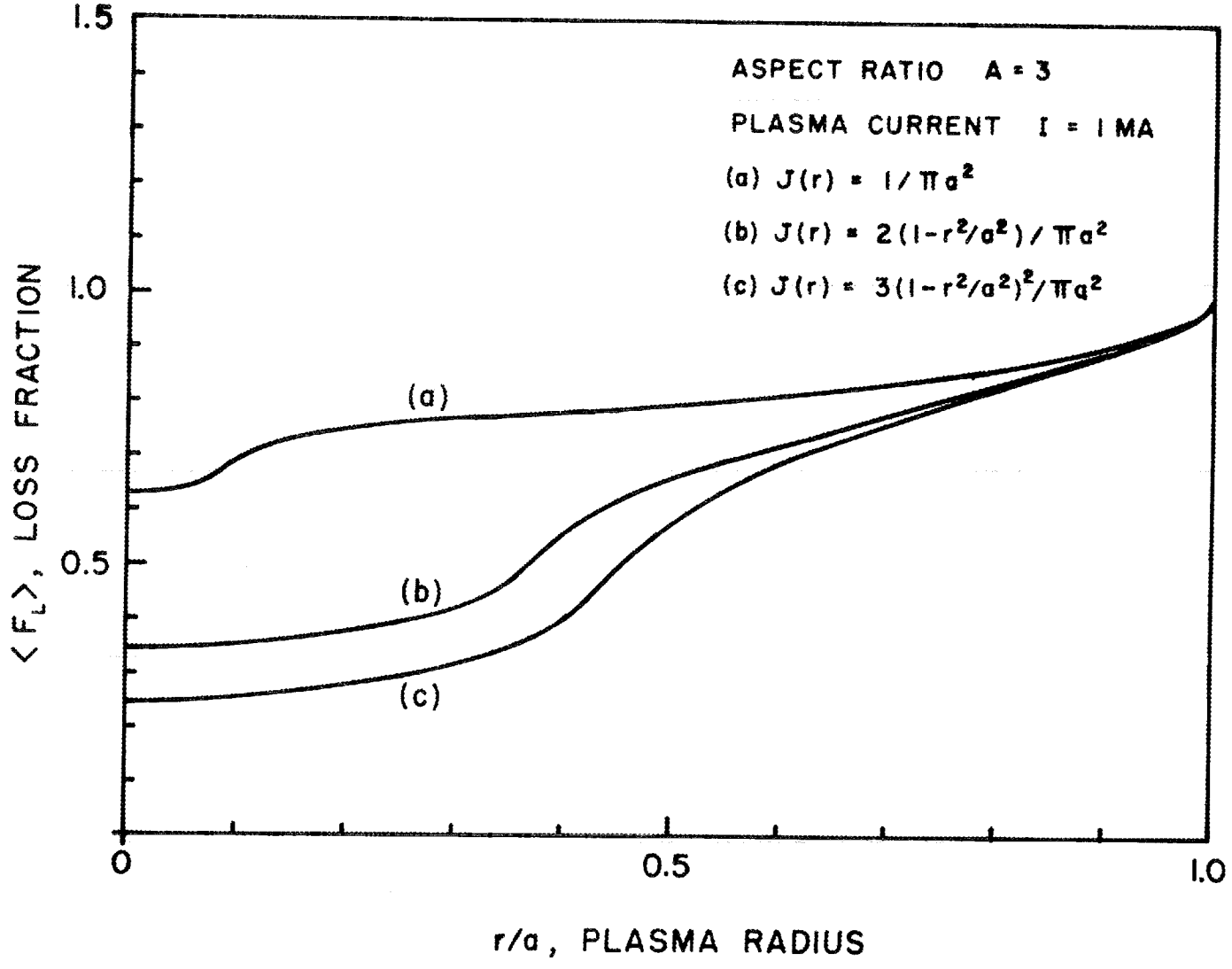
ASPECT RATIO A = 3
PLASMA CURRENT I = 1 MA
(a) J(r) = 1/πa²
(b) J(r) = 2(1-r²/a²)/πa²
(c) J(r) = 3(1-r²/a²)²/πa²
(a)
(b)
(c)
1.5
1.0
0.5
0
0.5
1.0
<F_L>, LOSS FRACTION
r/a, PLASMA RADIUS

Figure 10

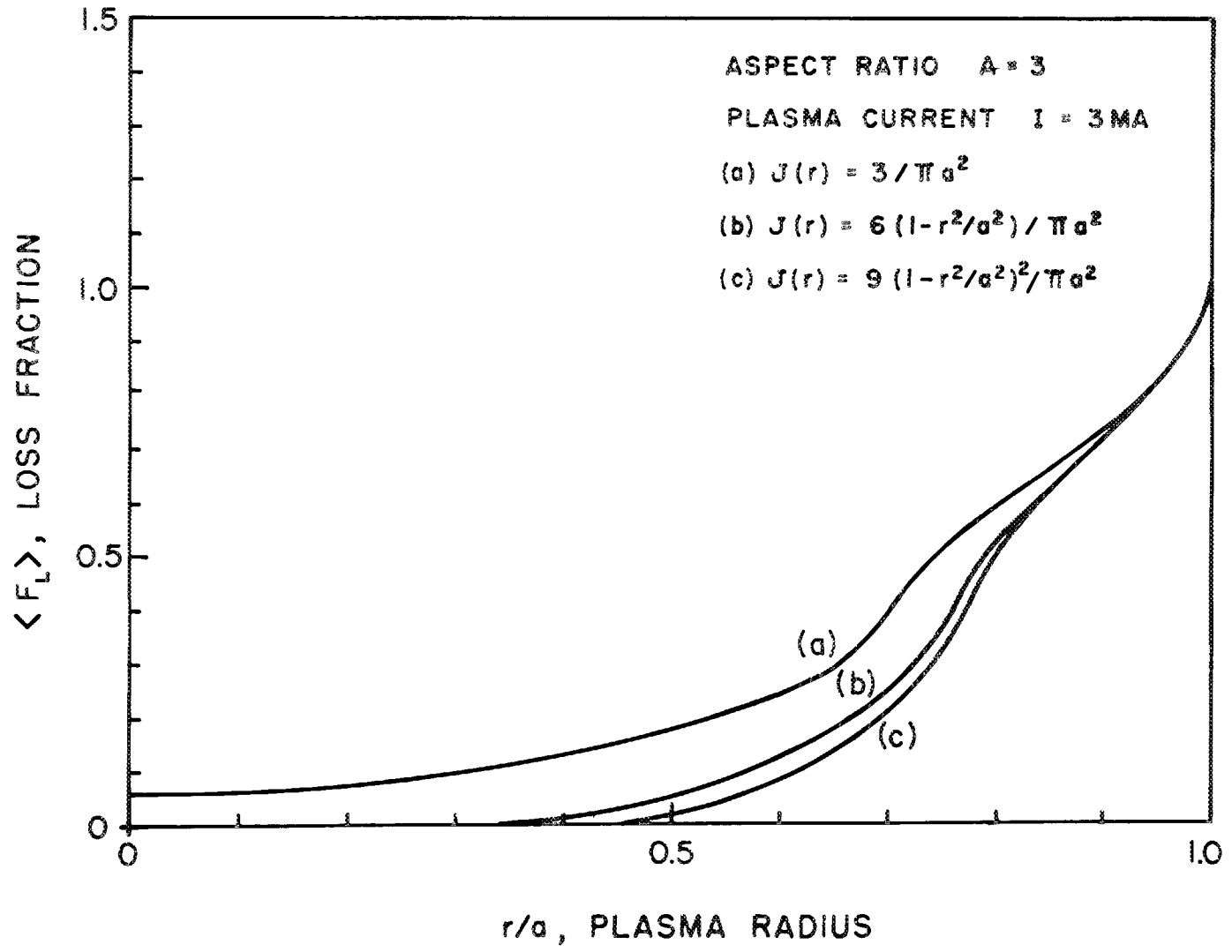
ASPECT RATIO A = 3
PLASMA CURRENT I = 3MA
(a) J(r) = 3/πa²
(b) J(r) = 6(1-r²/a²)/πa²
(c) J(r) = 9(1-r²/a²)²/πa²
(a)
(b)
(c)
1.5
1.0
0.5
0
0
0.5
1.0
<F_L>, LOSS FRACTION
r/a, PLASMA RADIUS

Figure 11

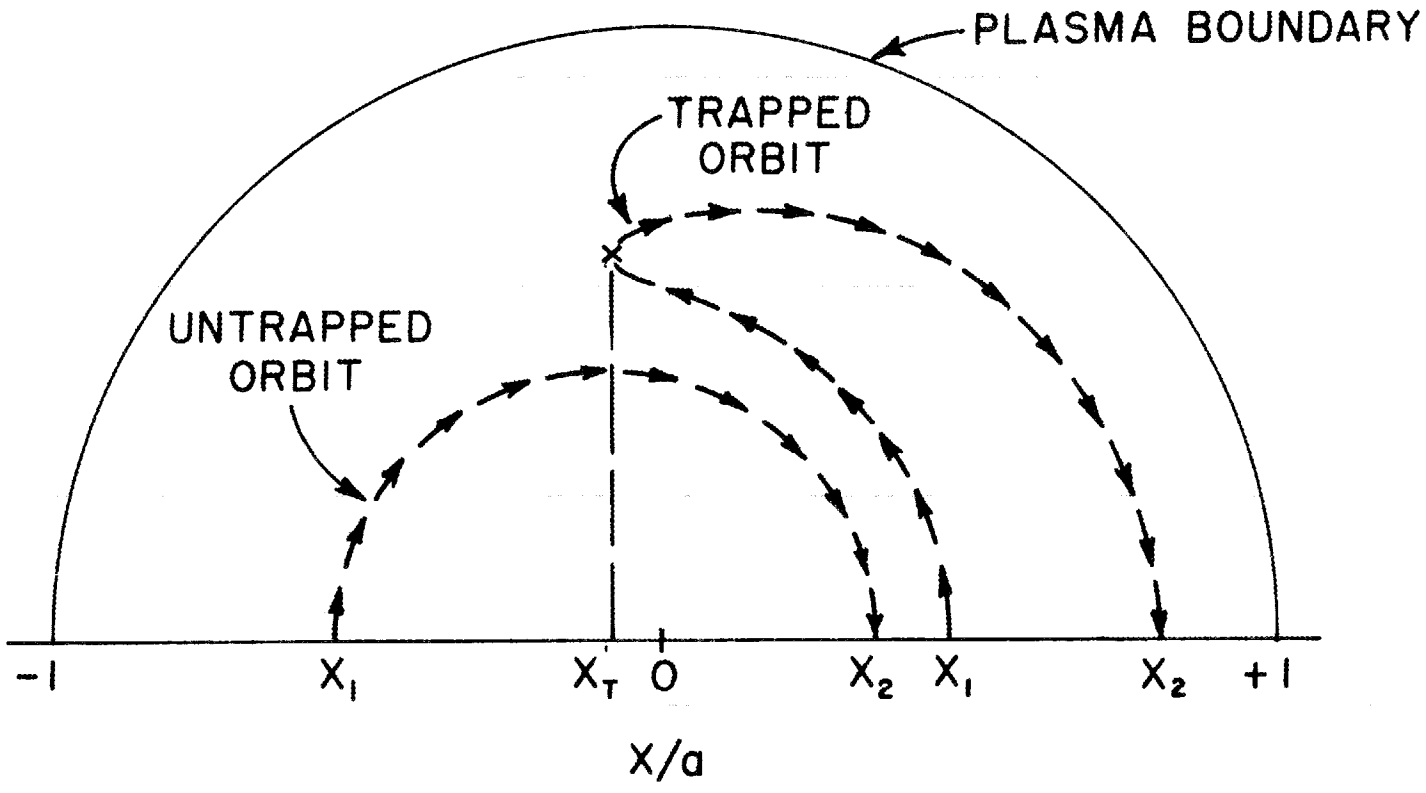

PLASMA CROSS SECTION
(TYPICAL INTEGRATION PATHS)

Figure 12

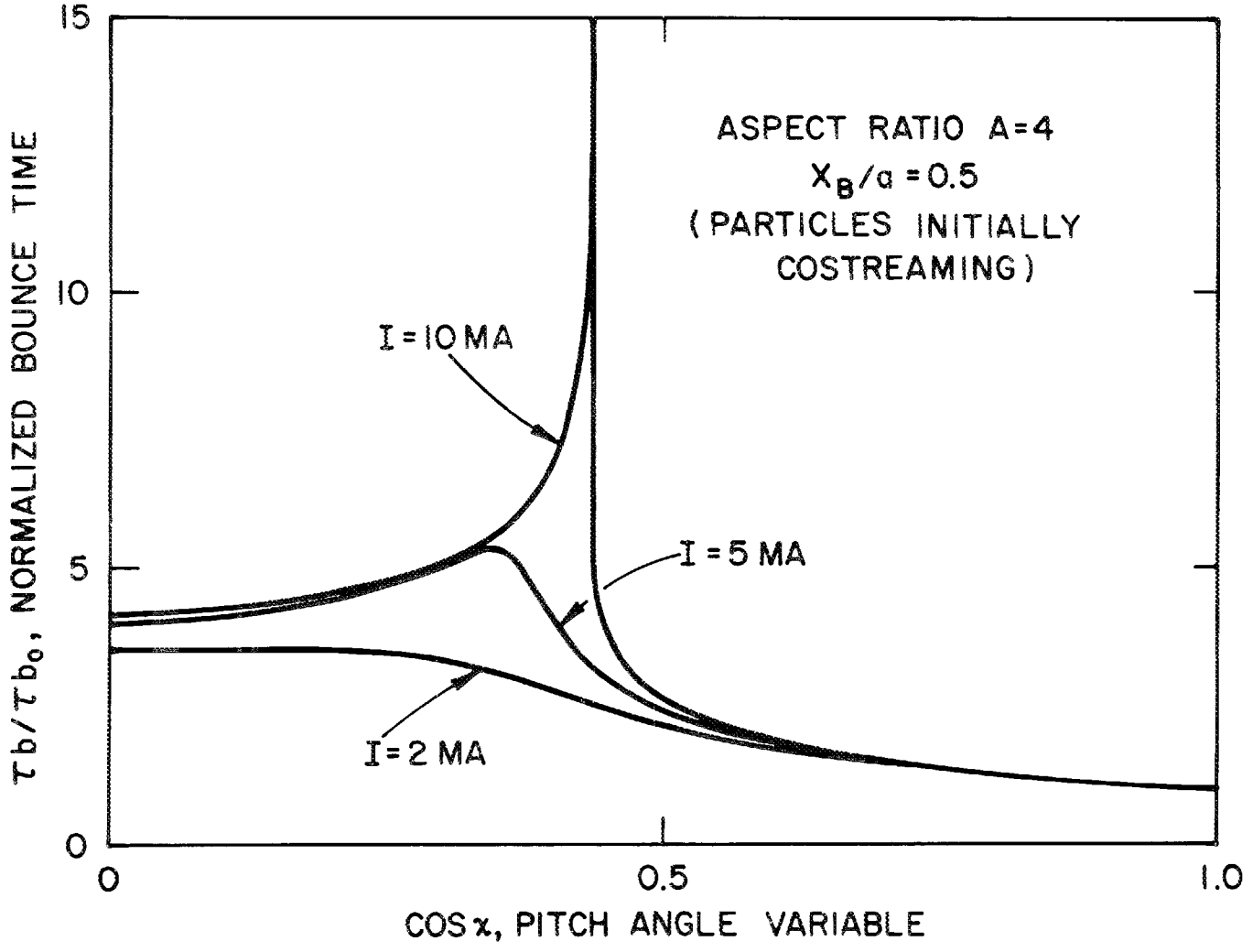
15
10
5
0
0
0.5
1.0
ASPECT RATIO A=4
$X_B/a = 0.5$
(PARTICLES INITIALLY COSTREAMING)
I = 10 MA
I = 5 MA
I = 2 MA
$\tau b/\tau b_o$, NORMALIZED BOUNCE TIME
COS χ, PITCH ANGLE VARIABLE

Figure 13

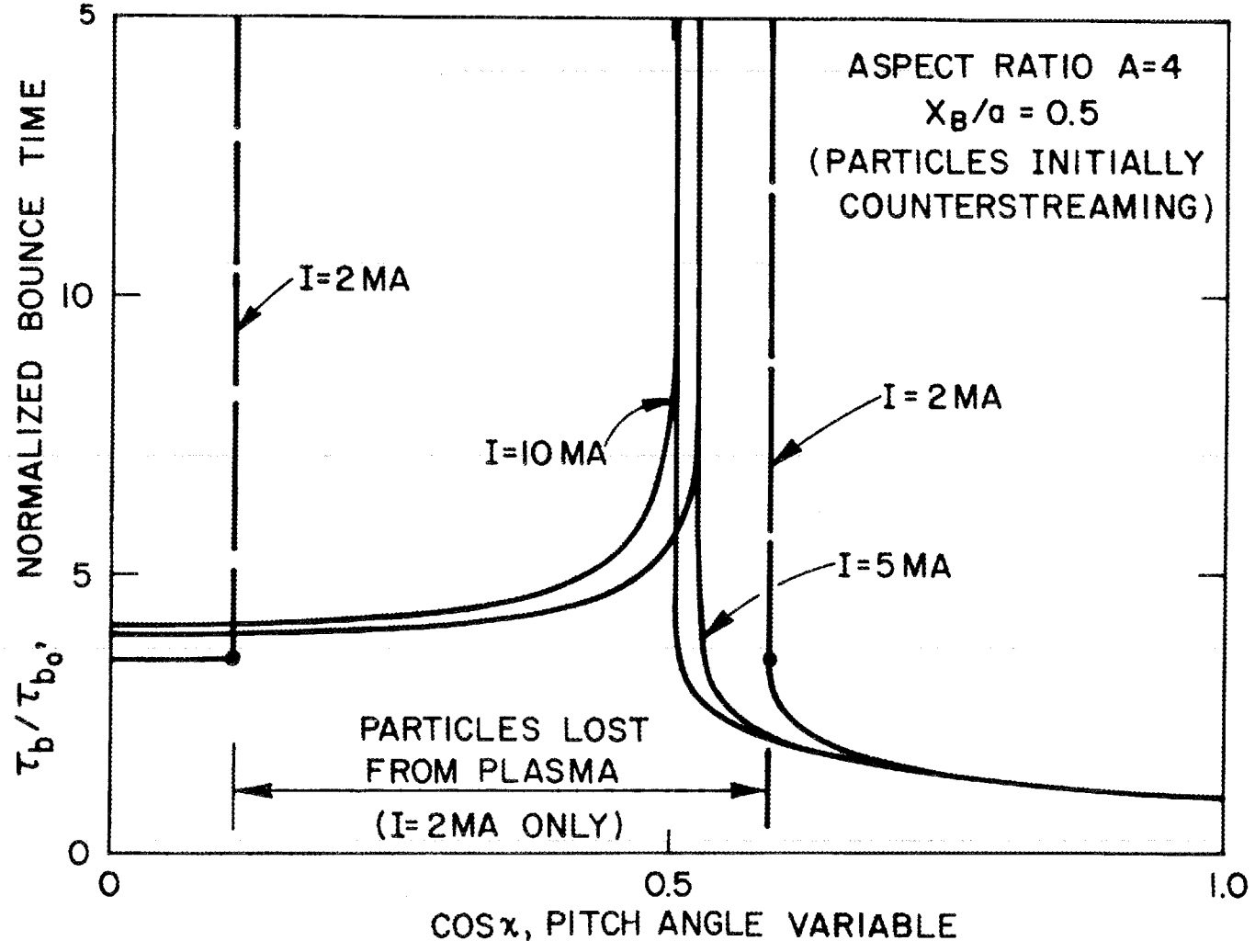
ASPECT RATIO A=4
$X_B/a = 0.5$
(PARTICLES INITIALLY COUNTERSTREAMING)
I=2 MA
I=10 MA
I = 2 MA
I=5 MA
PARTICLES LOST FROM PLASMA
(I=2MA ONLY)
NORMALIZED BOUNCE TIME
τ_b/τ_{b_o},
COSχ, PITCH ANGLE VARIABLE
0
5
10
0.5
1.0

Figure 14

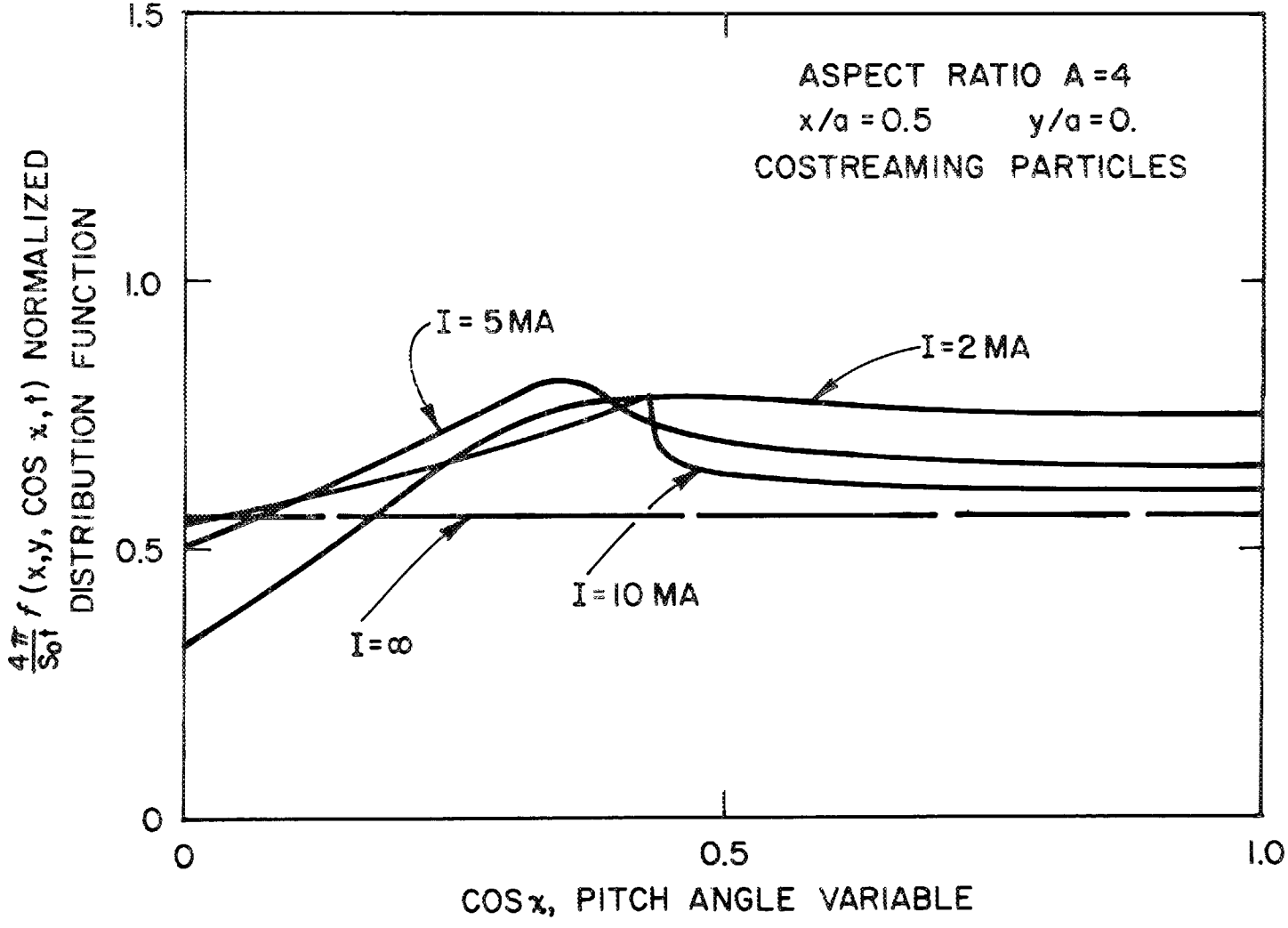
ASPECT RATIO A=4
x/a = 0.5 y/a = 0.
COSTREAMING PARTICLES
I = 5 MA
I = 2 MA
I = 10 MA
I = ∞
1.5
1.0
0.5
0
0
0.5
1.0
$\frac{4\pi}{S_0 t} f(x,y,\cos\chi,t)$ NORMALIZED DISTRIBUTION FUNCTION
COS χ, PITCH ANGLE VARIABLE

Figure 15

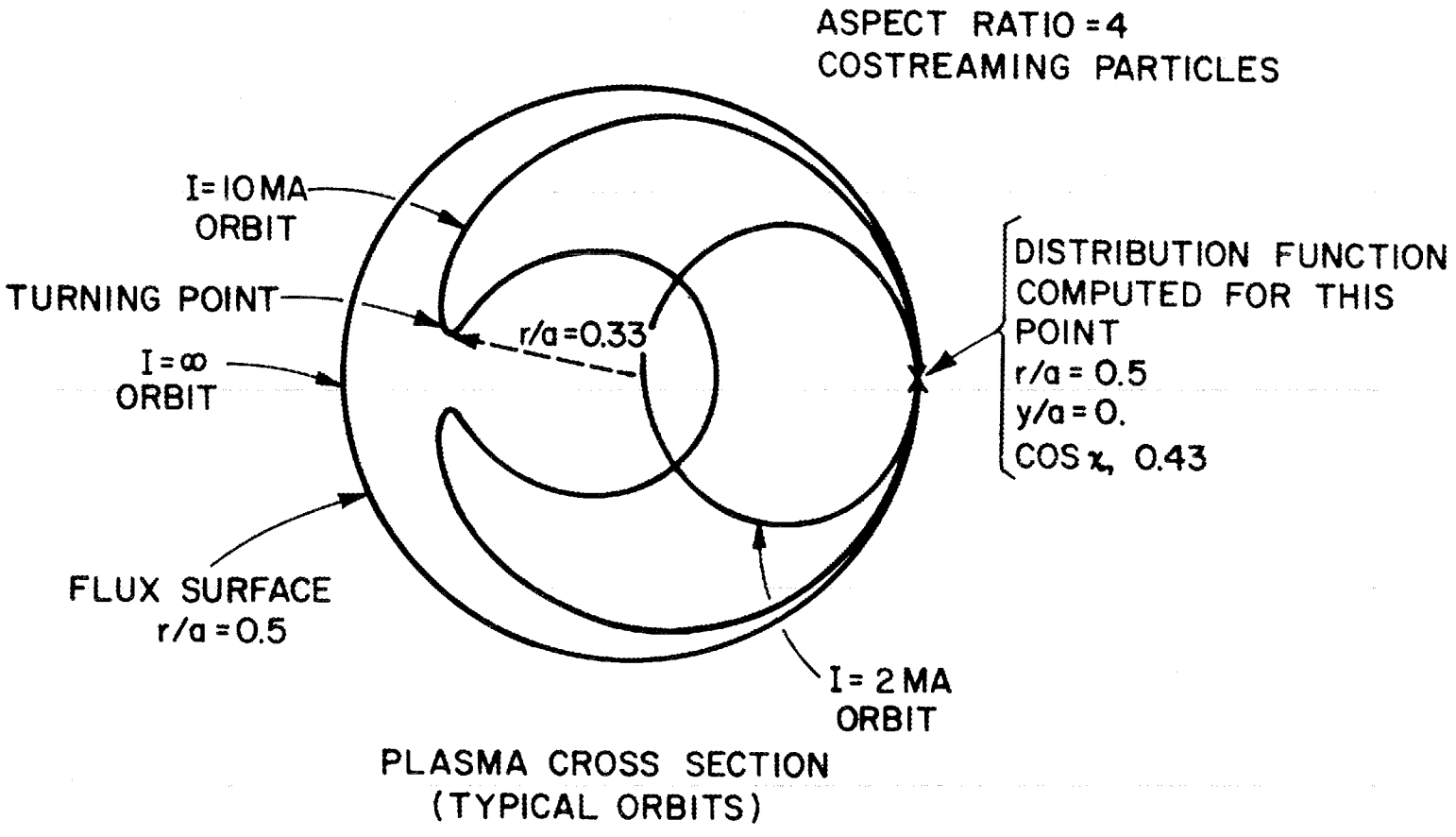
ASPECT RATIO = 4
COSTREAMING PARTICLES
I = 10 MA
ORBIT
TURNING POINT
I = ∞
ORBIT
r/a = 0.33
DISTRIBUTION FUNCTION
COMPUTED FOR THIS
POINT
r/a = 0.5
y/a = 0.
COS χ, 0.43
FLUX SURFACE
r/a = 0.5
I = 2 MA
ORBIT
PLASMA CROSS SECTION
(TYPICAL ORBITS)

Figure 16

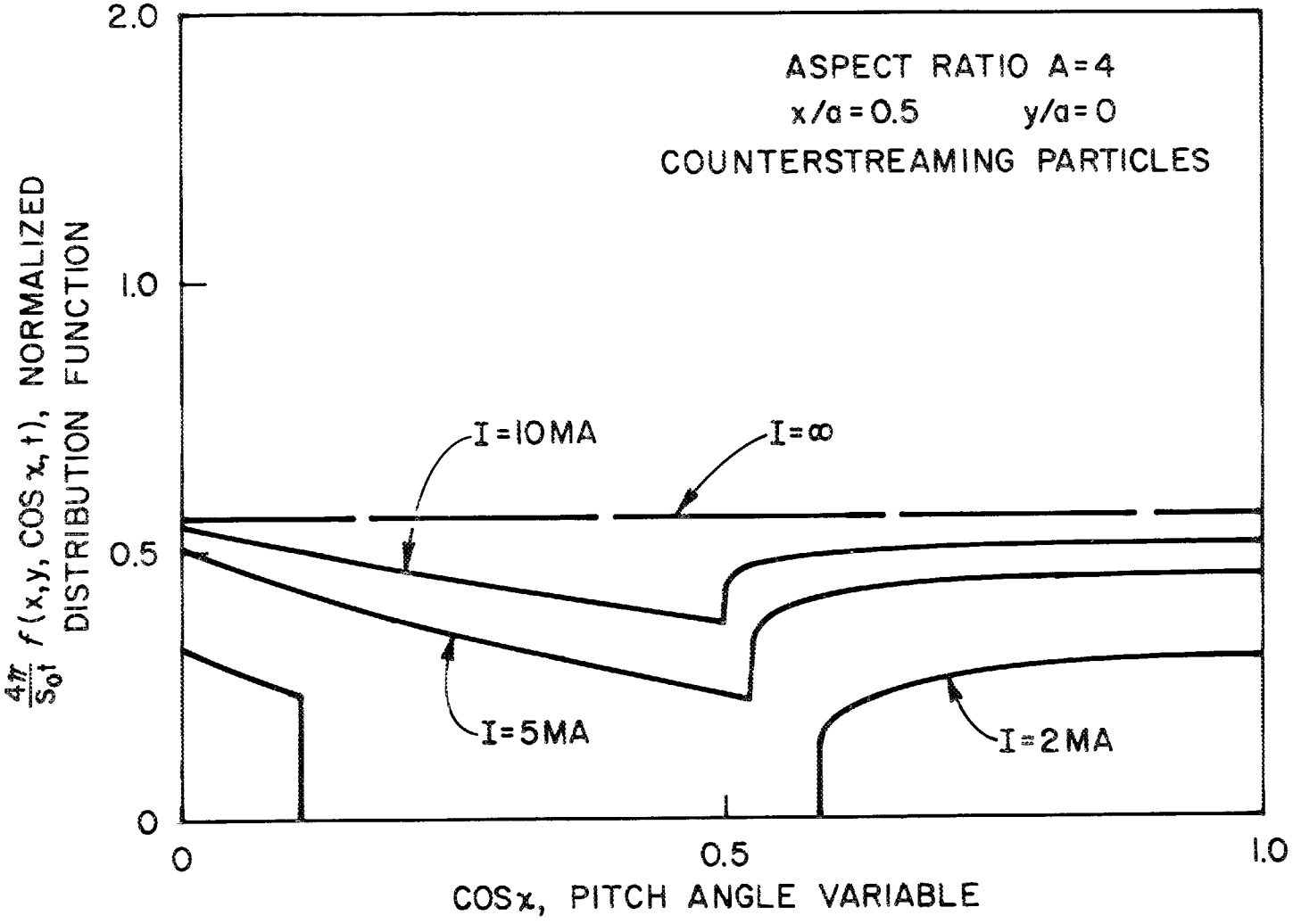
ASPECT RATIO A=4
x/a=0.5 y/a=0
COUNTERSTREAMING PARTICLES
I=10MA
I=∞
I=5MA
I=2MA
2.0
1.0
0.5
0
0
0.5
1.0
$\frac{4\pi}{S_0 t} f(x,y,\cos\chi,t)$, NORMALIZED DISTRIBUTION FUNCTION
COSχ, PITCH ANGLE VARIABLE

Figure 17

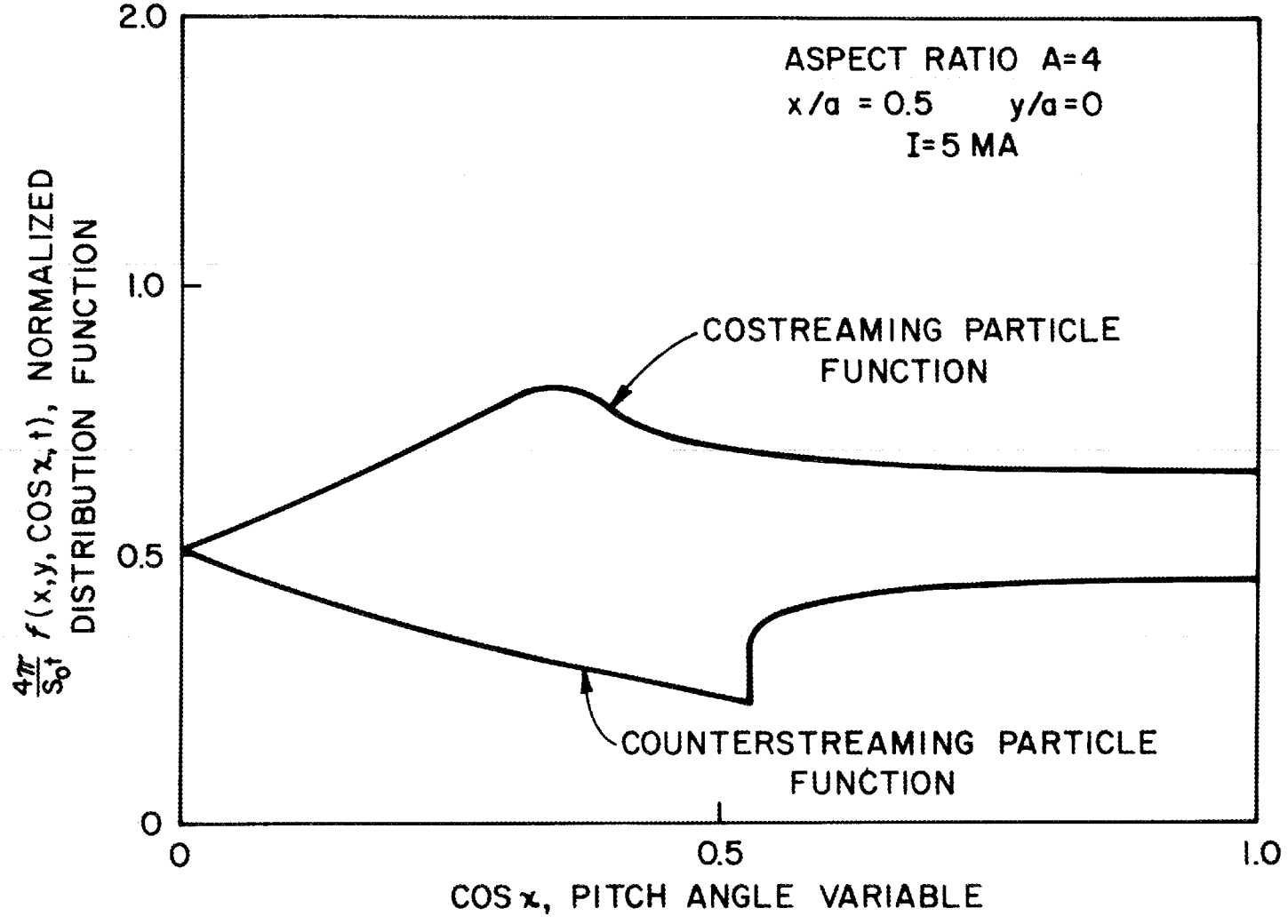
ASPECT RATIO A=4
x/a = 0.5 y/a=0
I=5 MA
COSTREAMING PARTICLE FUNCTION
COUNTERSTREAMING PARTICLE FUNCTION
2.0
1.0
0.5
0
0
0.5
1.0
$\frac{4\pi}{S_0 t} f(x,y,\cos\chi,t)$, NORMALIZED DISTRIBUTION FUNCTION
COS χ, PITCH ANGLE VARIABLE

Figure 18

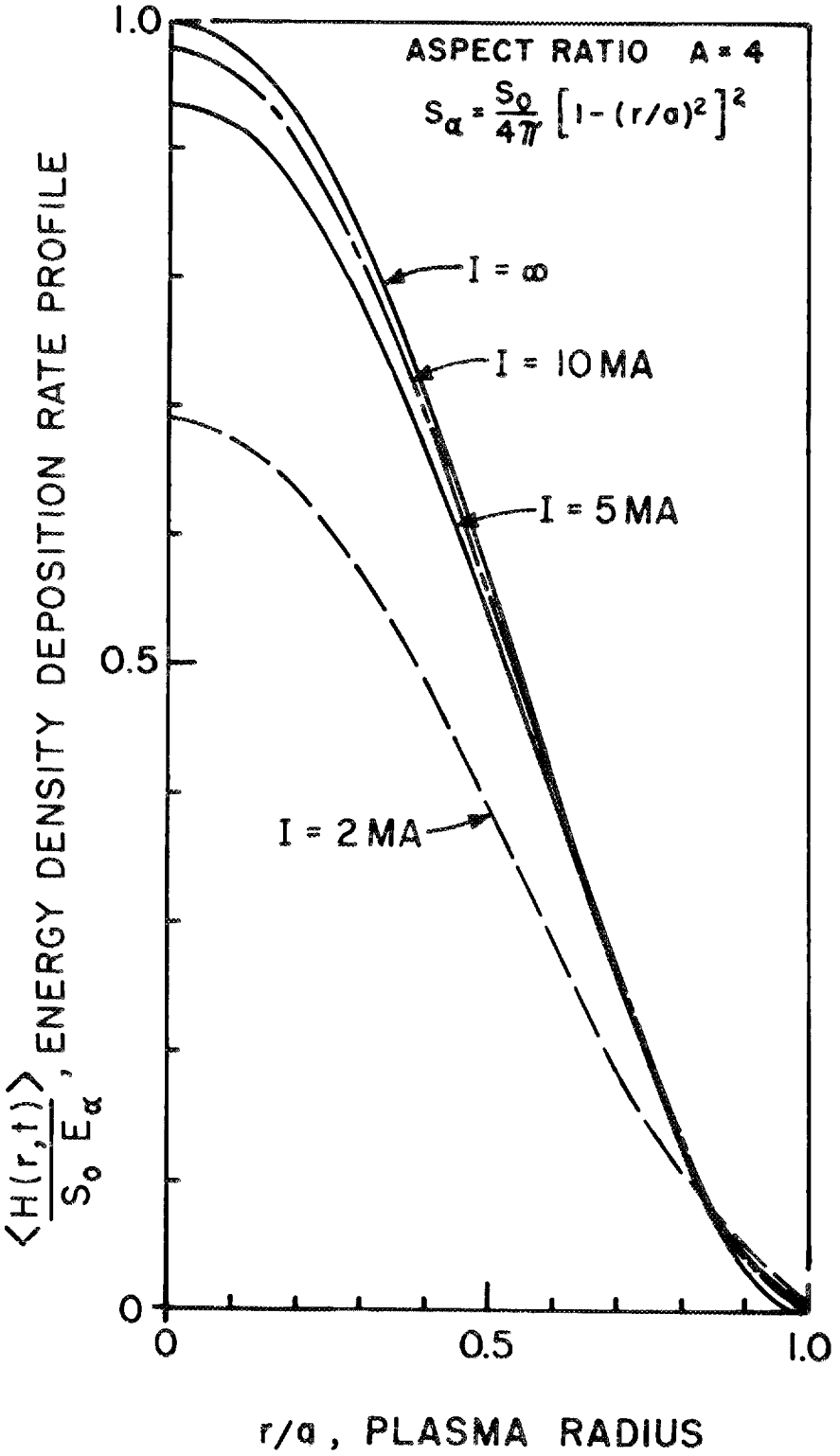
ASPECT RATIO A = 4
$S_\alpha = \frac{S_0}{4\pi}\left[1-(r/a)^2\right]^2$
I = ∞
I = 10 MA
I = 5 MA
I = 2 MA
1.0
0.5
0
0
0.5
1.0
$\frac{\langle H(r,t)\rangle}{S_0 E_\alpha}$, ENERGY DENSITY DEPOSITION RATE PROFILE
r/a, PLASMA RADIUS

Figure 19

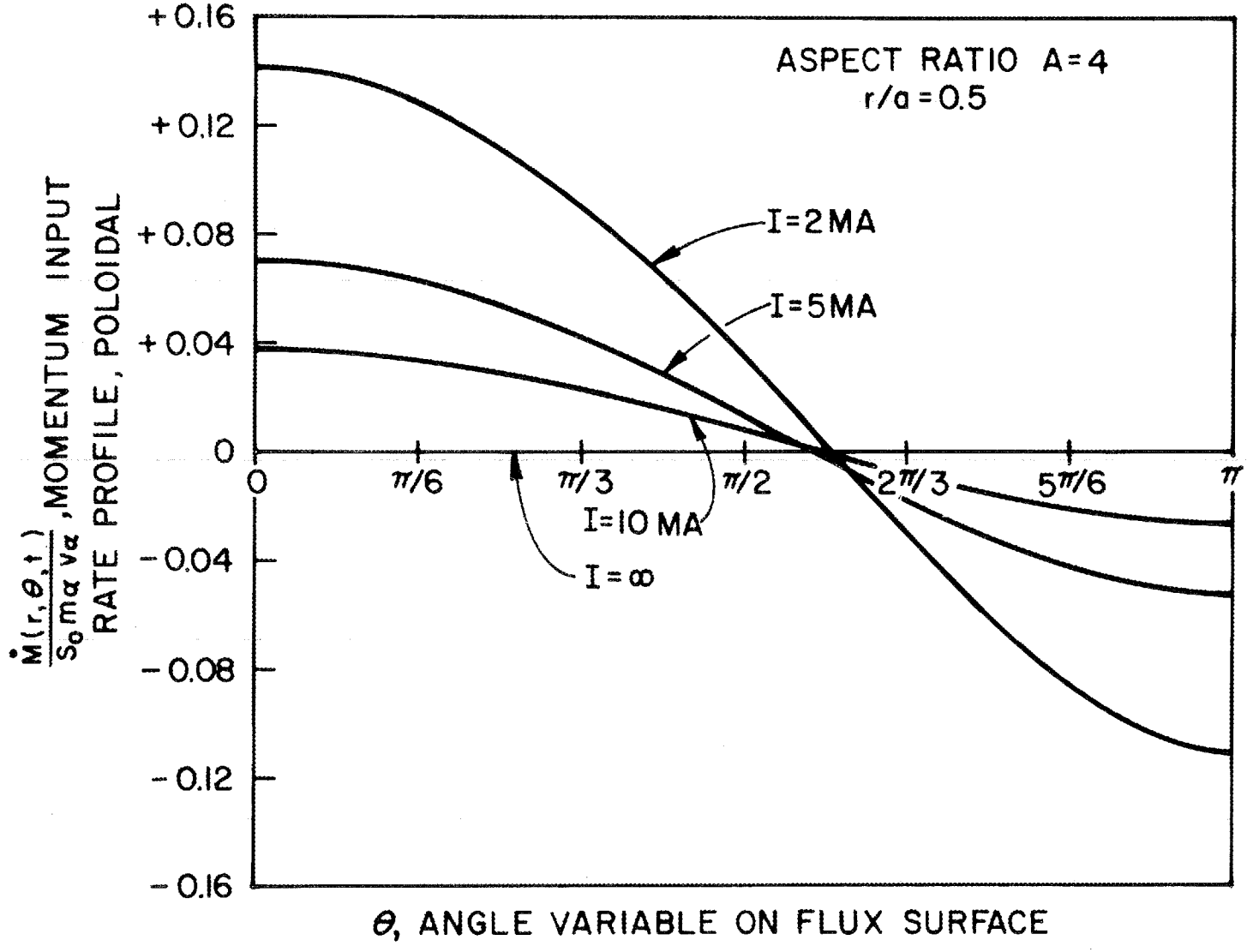
ASPECT RATIO A=4
r/a=0.5
I=2MA
I=5MA
I=10 MA
I=∞
+0.16
+0.12
+0.08
+0.04
0
-0.04
-0.08
-0.12
-0.16
0
π/6
π/3
π/2
2π/3
5π/6
π
$\frac{\dot{M}(r,\theta,t)}{S_0 m_\alpha v_\alpha}$, MOMENTUM INPUT RATE PROFILE, POLOIDAL
θ, ANGLE VARIABLE ON FLUX SURFACE

Figure 20

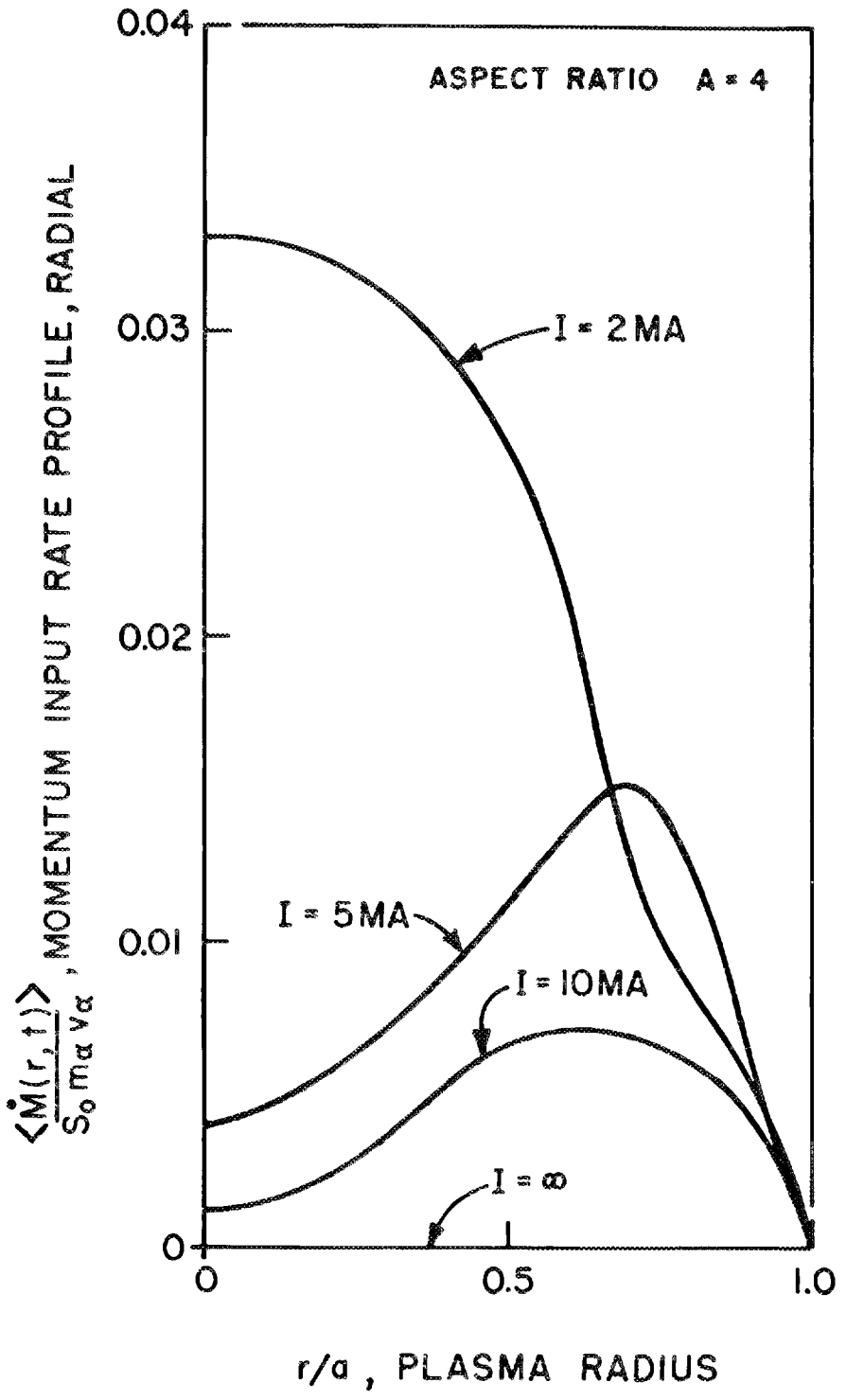
ASPECT RATIO A = 4
I = 2MA
I = 5MA
I = 10MA
I = ∞
0.04
0.03
0.02
0.01
0
0
0.5
1.0
$\frac{\langle \dot{M}(r,t) \rangle}{S_o m_\alpha v_\alpha}$, MOMENTUM INPUT RATE PROFILE, RADIAL
r/a , PLASMA RADIUS

Figure 21

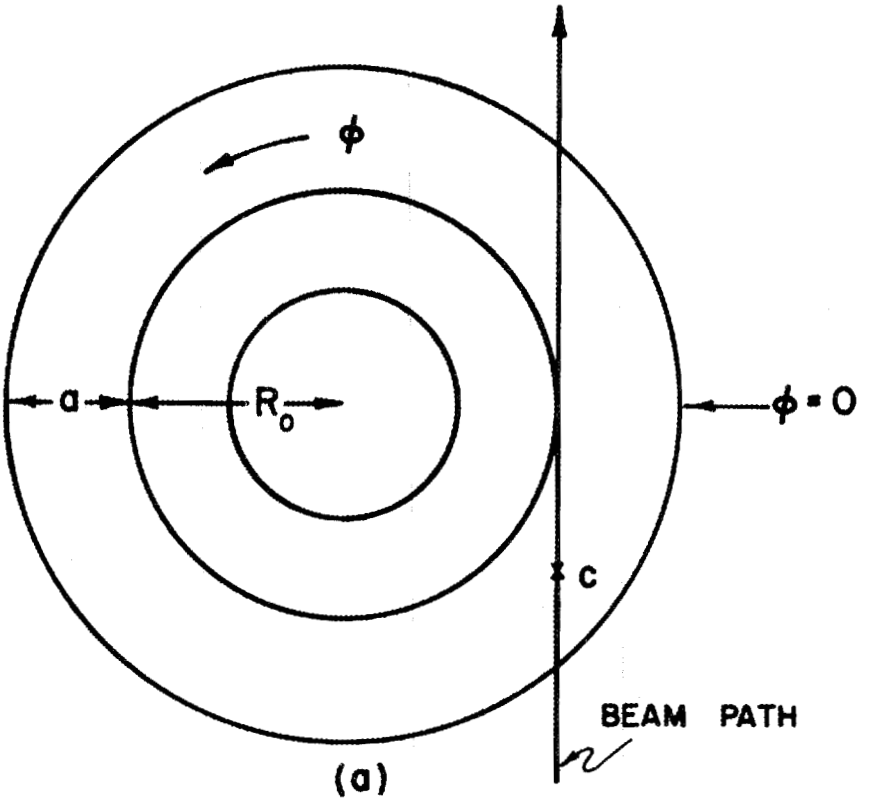

(a)

TOP VIEW OF PLASMA

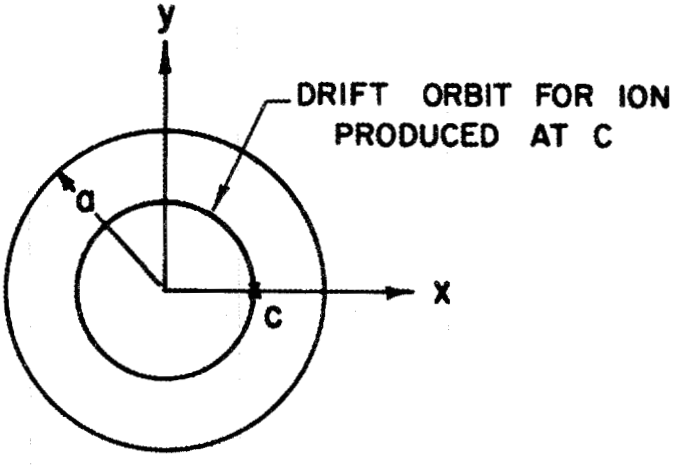

(b)

CROSS SECTION VIEW OF PLASMA

Figure 22

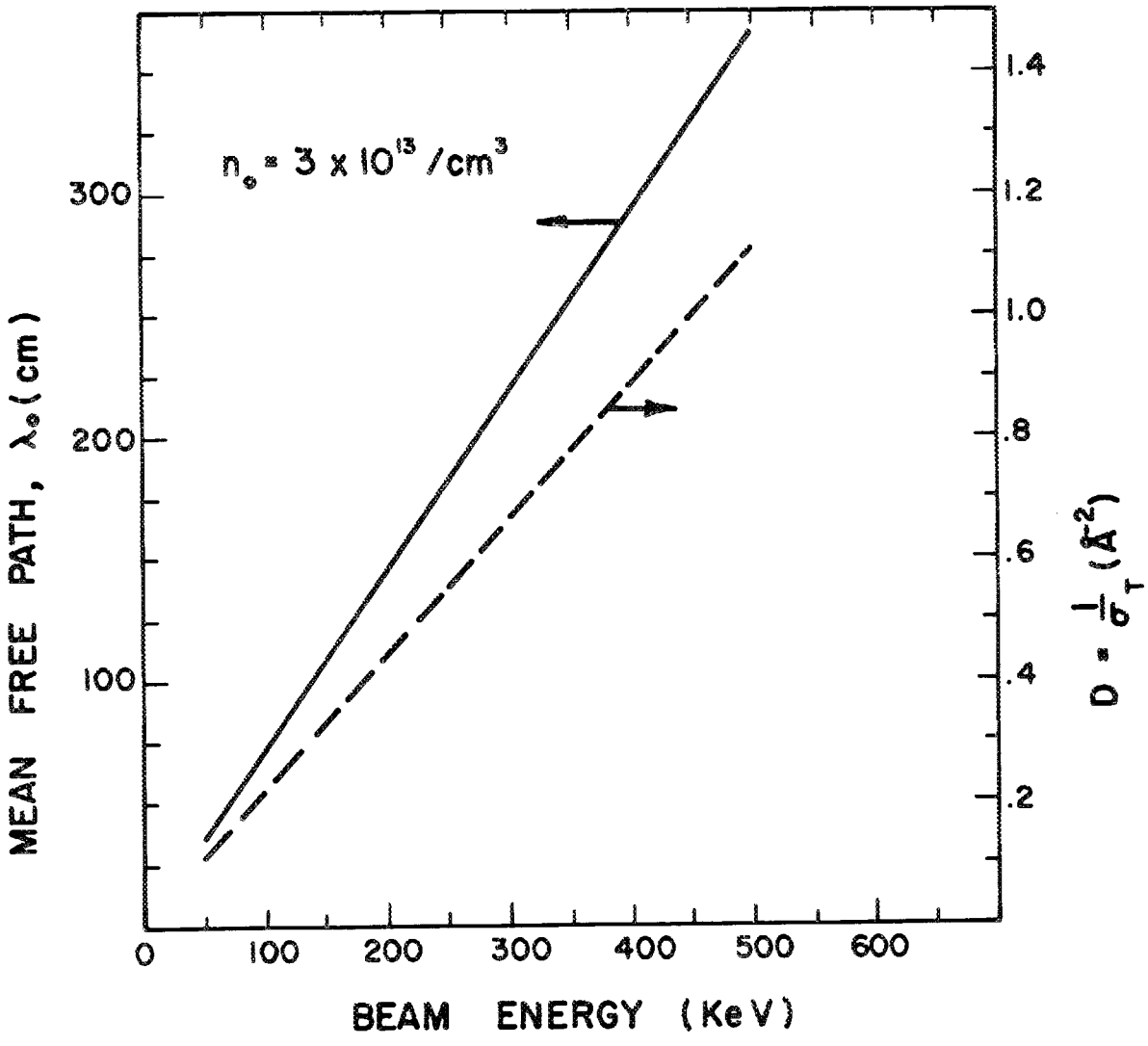
$n_o = 3 \times 10^{13}/cm^3$
MEAN FREE PATH, λ_o (cm)
300
200
100
0
100
200
300
400
500
600
BEAM ENERGY (KeV)
1.4
1.2
1.0
.8
.6
.4
.2
$D = \frac{1}{\sigma_T}$ ($Å^2$)

Figure 23

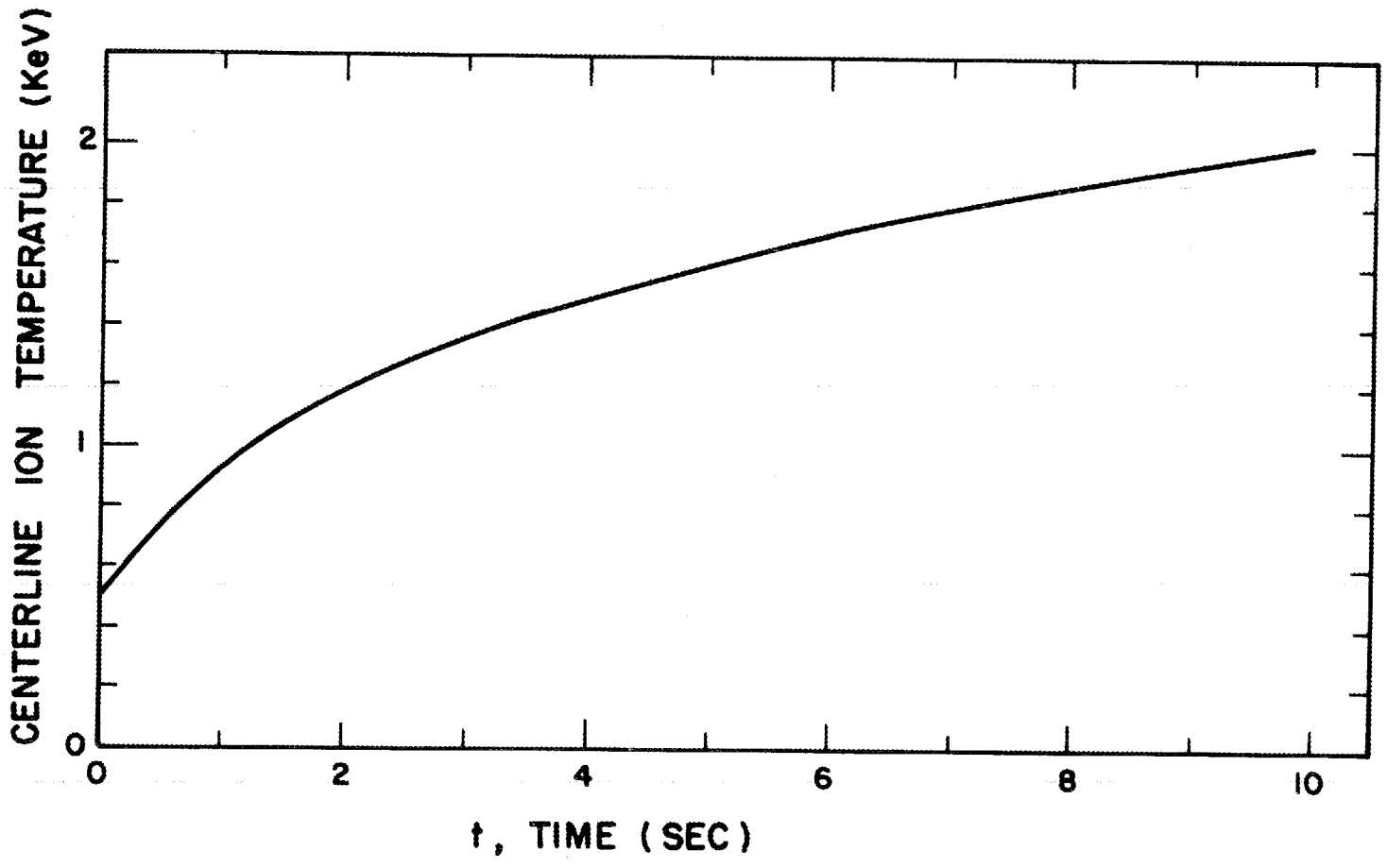

Figure 24

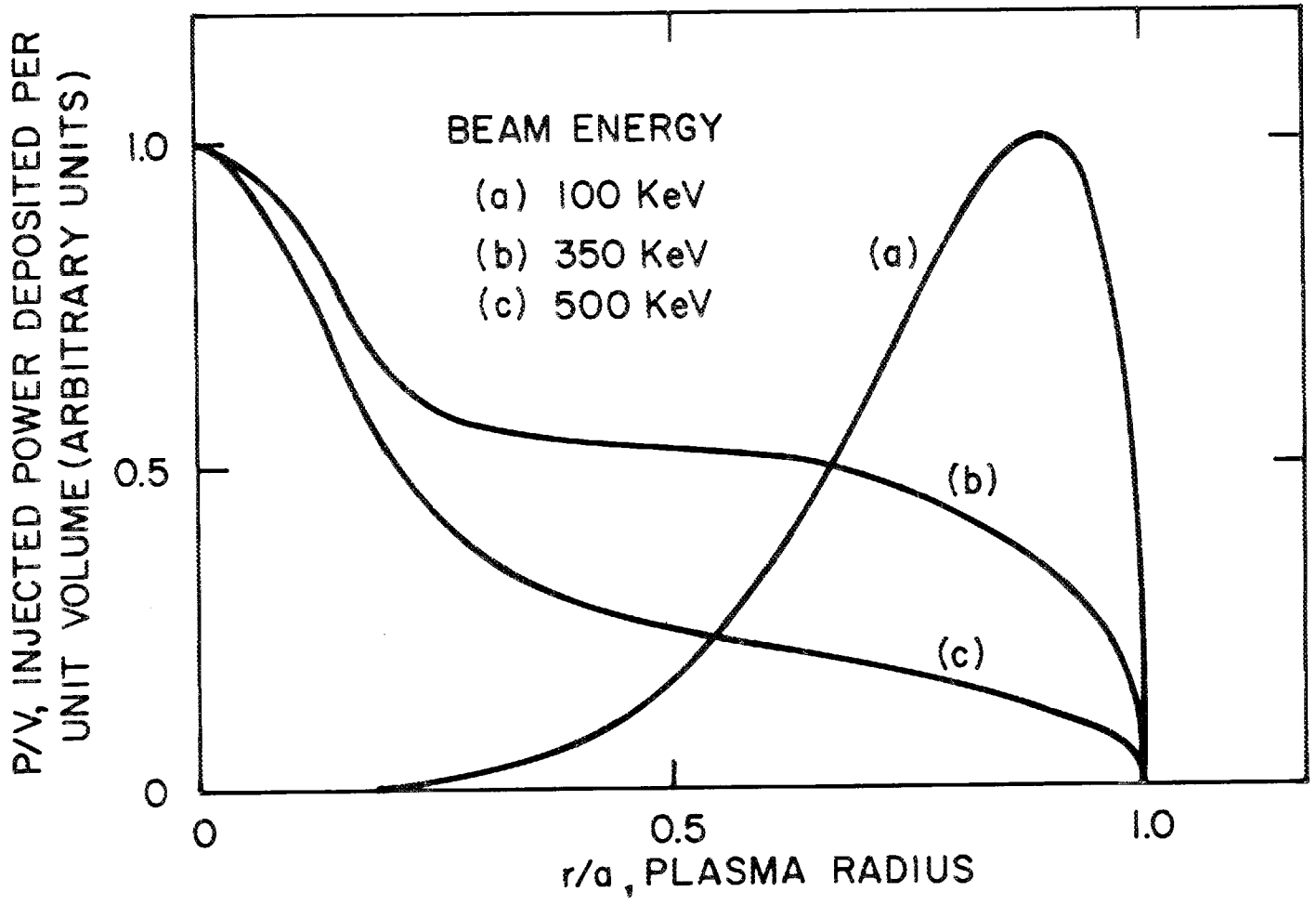
P/V, INJECTED POWER DEPOSITED PER UNIT VOLUME (ARBITRARY UNITS)
1.0
0.5
0
BEAM ENERGY
(a) 100 KeV
(b) 350 KeV
(c) 500 KeV
(a)
(b)
(c)
0
0.5
1.0
r/a, PLASMA RADIUS

Figure 25

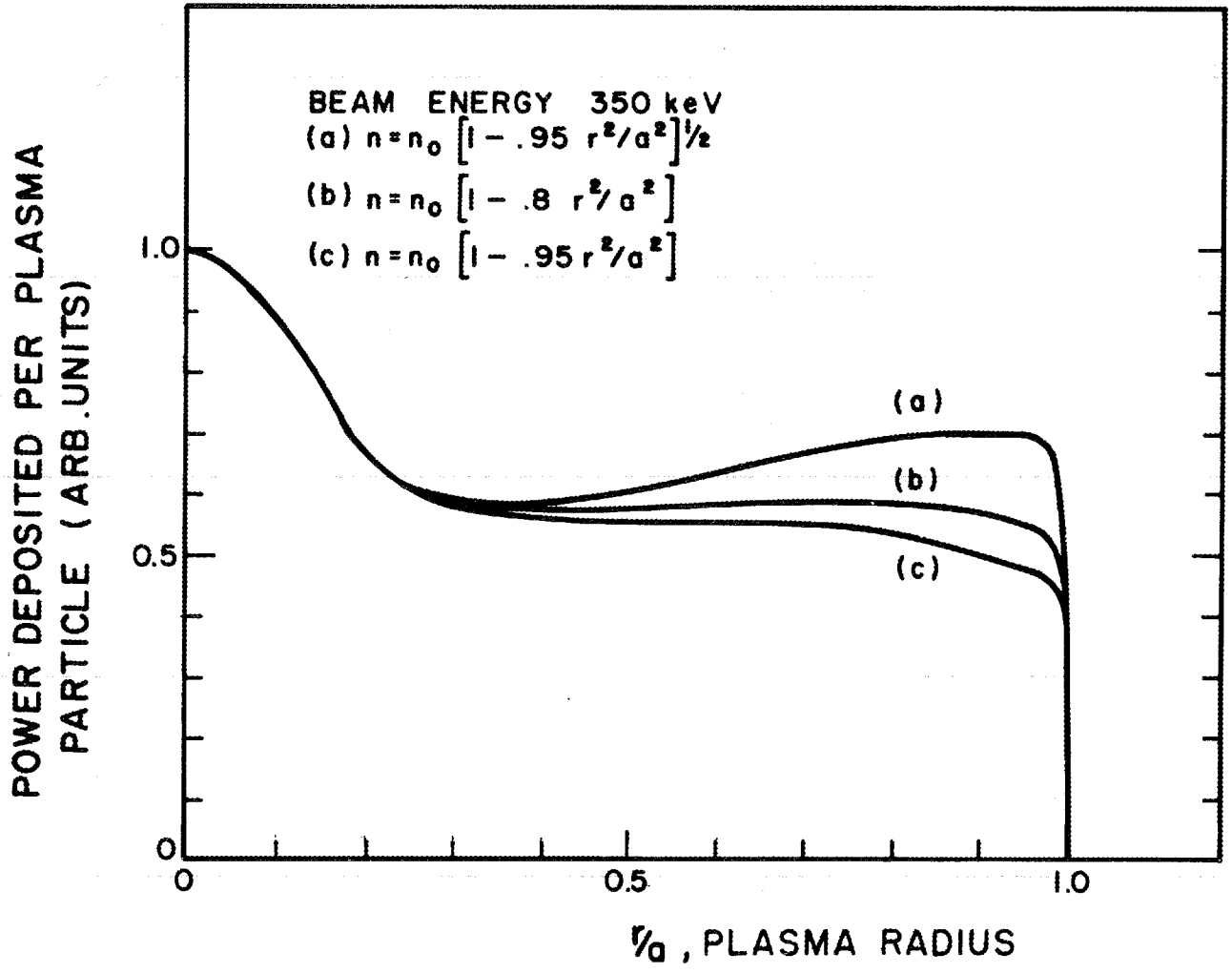
BEAM ENERGY 350 keV
(a) n = n0 [1 − .95 r²/a²]½
(b) n = n0 [1 − .8 r²/a²]
(c) n = n0 [1 − .95 r²/a²]
POWER DEPOSITED PER PLASMA PARTICLE (ARB. UNITS)
1.0
0.5
0
0
0.5
1.0
(a)
(b)
(c)
r/a , PLASMA RADIUS

Figure 26

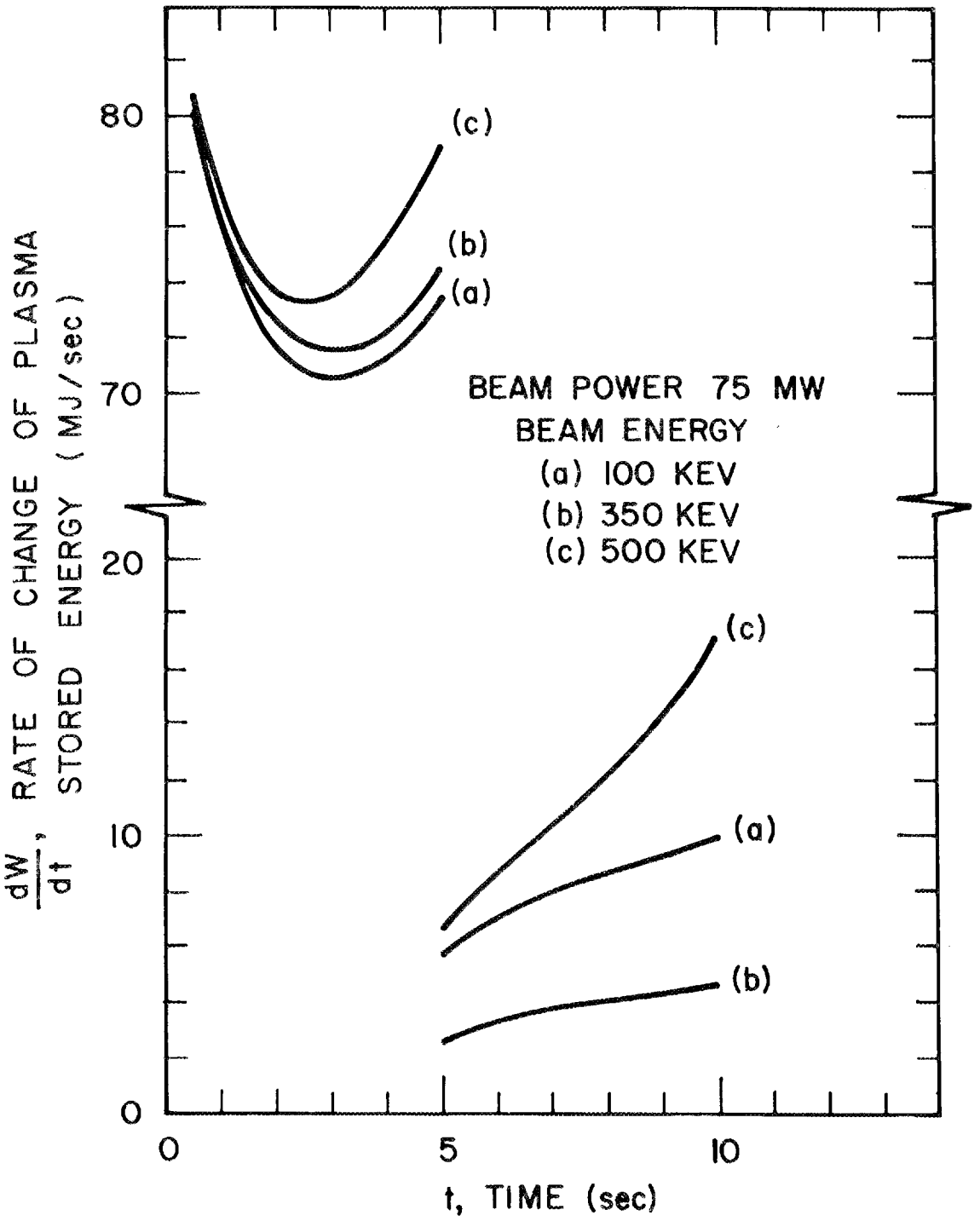
80
70
20
10
0
0
5
10
(c)
(b)
(a)
BEAM POWER 75 MW
BEAM ENERGY
(a) 100 KEV
(b) 350 KEV
(c) 500 KEV
(c)
(a)
(b)
dW/dt, RATE OF CHANGE OF PLASMA STORED ENERGY (MJ/sec)
t, TIME (sec)

Figure 27

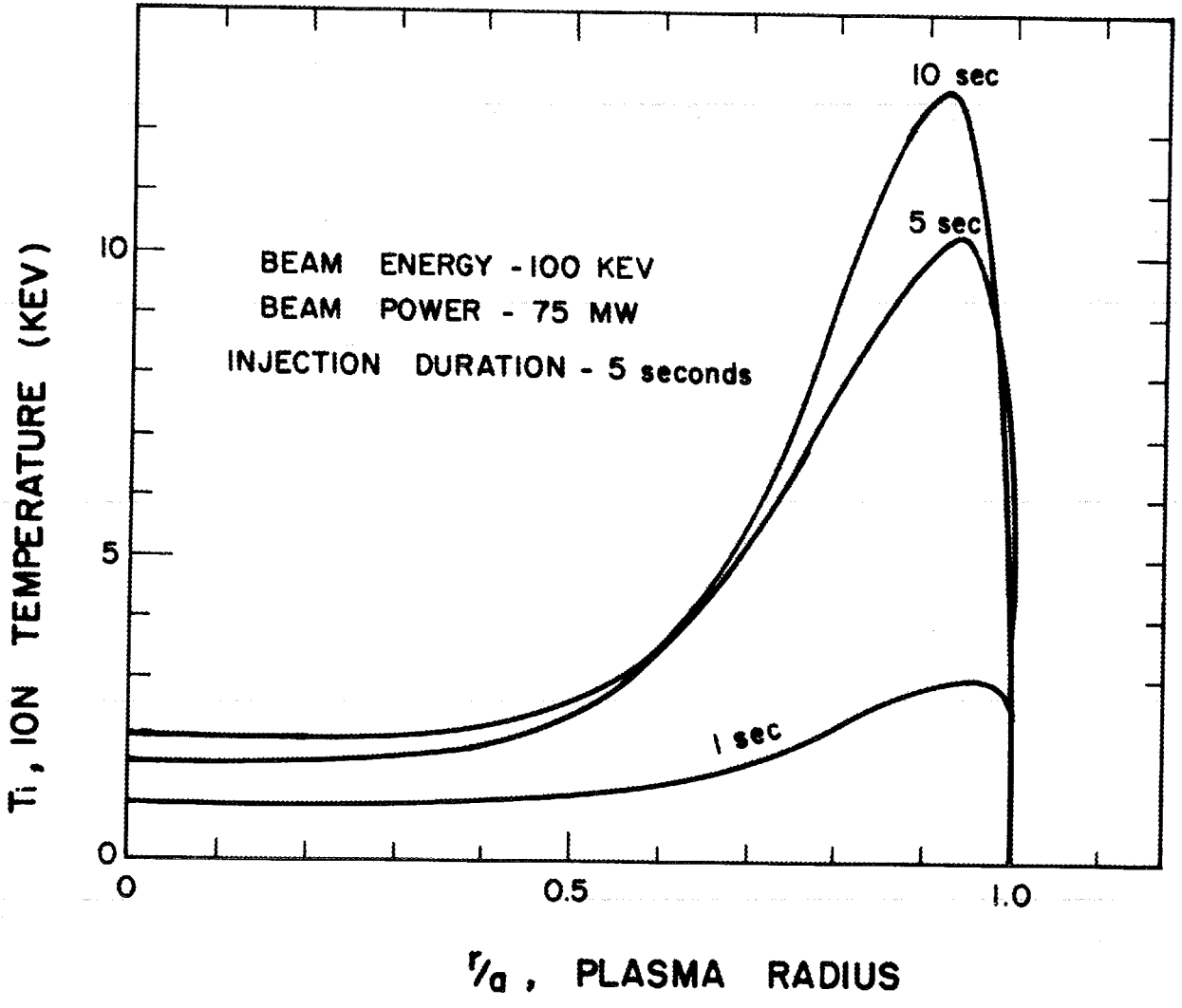
10 sec
5 sec
1 sec
BEAM ENERGY - 100 KEV
BEAM POWER - 75 MW
INJECTION DURATION - 5 seconds
Ti, ION TEMPERATURE (KEV)
10
5
0
0
0.5
1.0
r/a, PLASMA RADIUS

Figure 28

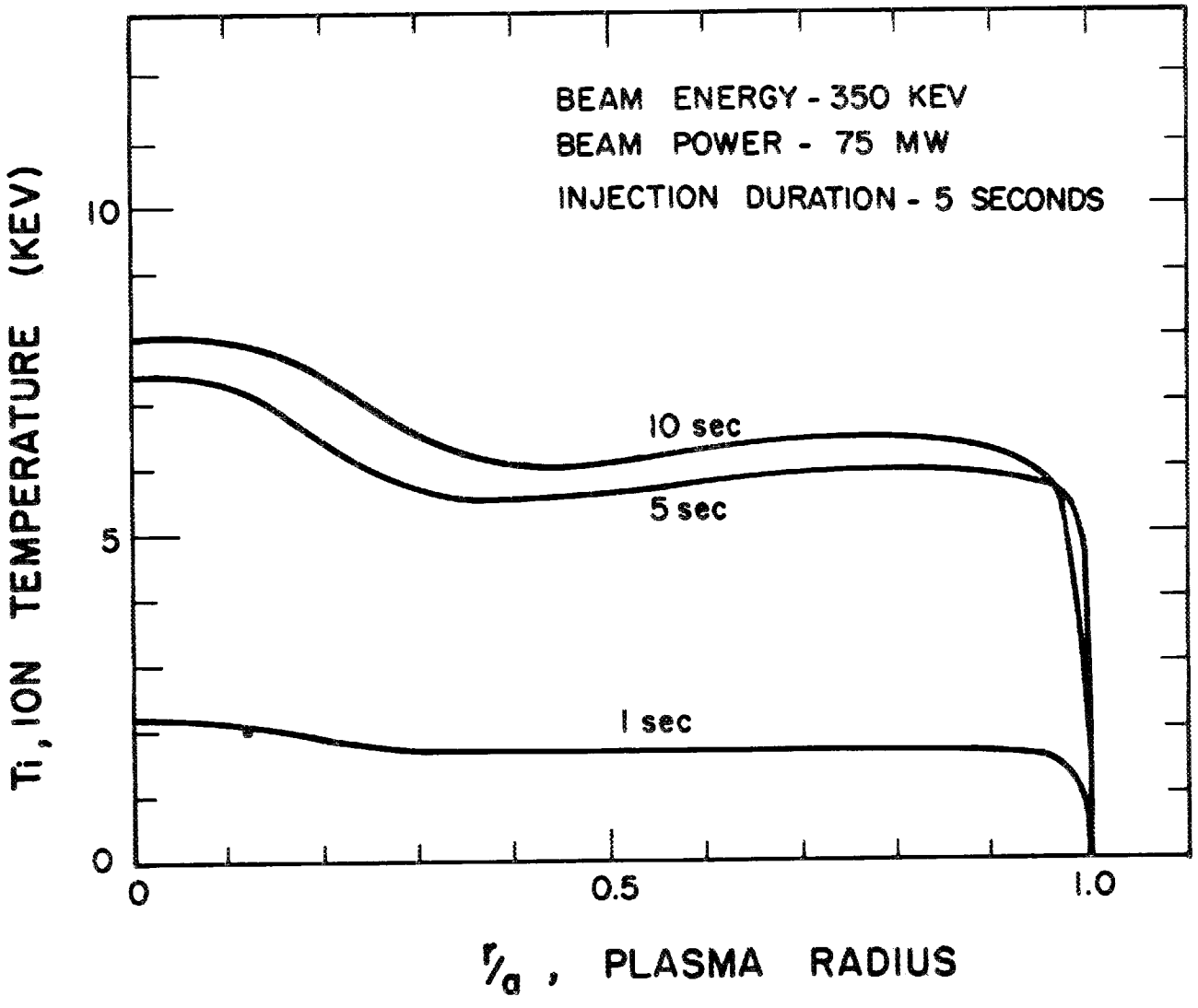
BEAM ENERGY - 350 KEV
BEAM POWER - 75 MW
INJECTION DURATION - 5 SECONDS
10 sec
5 sec
1 sec
Ti, ION TEMPERATURE (KEV)
10
5
0
0
0.5
1.0
r/a , PLASMA RADIUS

Figure 29

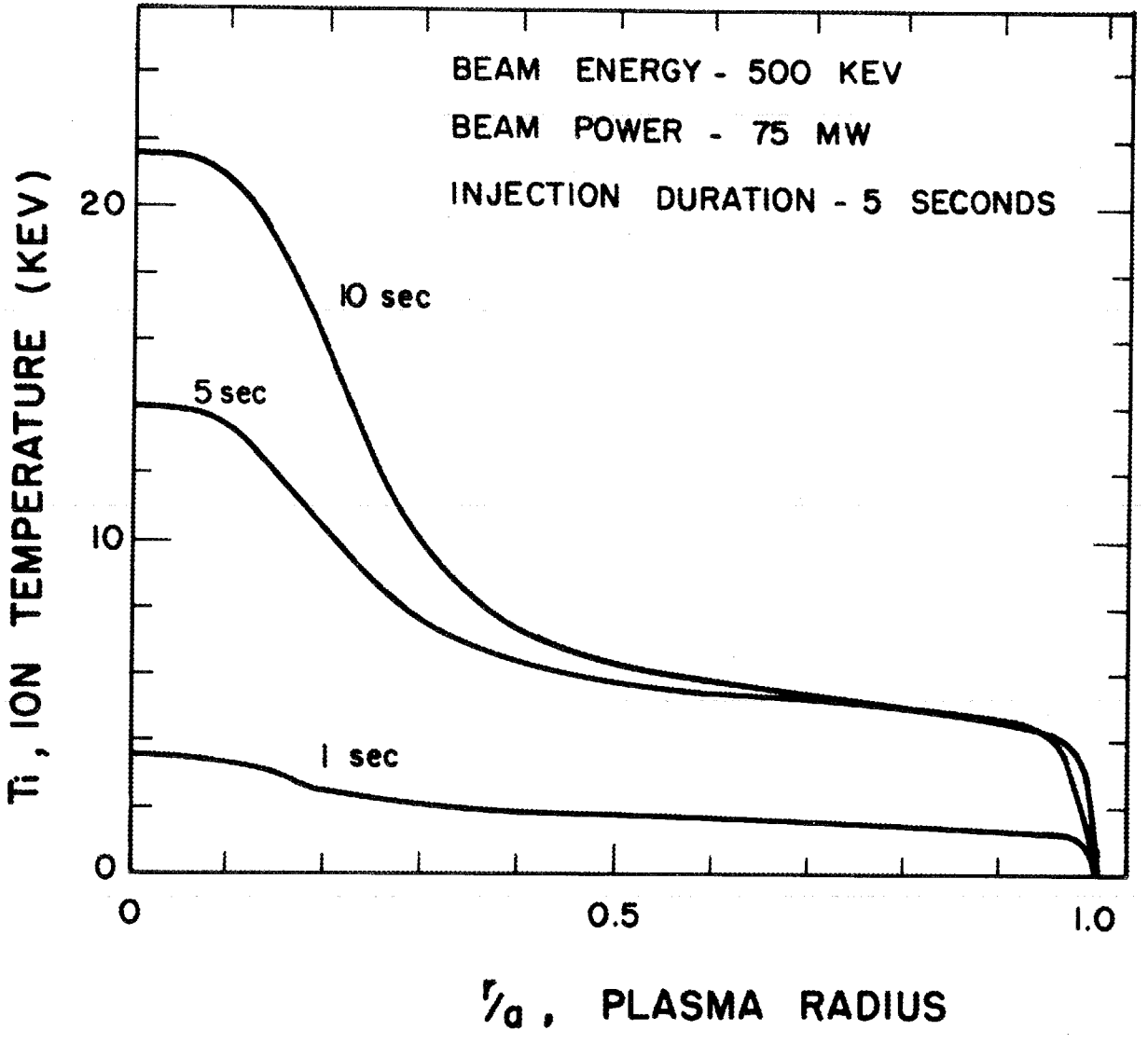
BEAM ENERGY - 500 KEV
BEAM POWER - 75 MW
INJECTION DURATION - 5 SECONDS
10 sec
5 sec
1 sec
Ti, ION TEMPERATURE (KEV)
20
10
0
0
0.5
1.0
r/a, PLASMA RADIUS

Figure 30

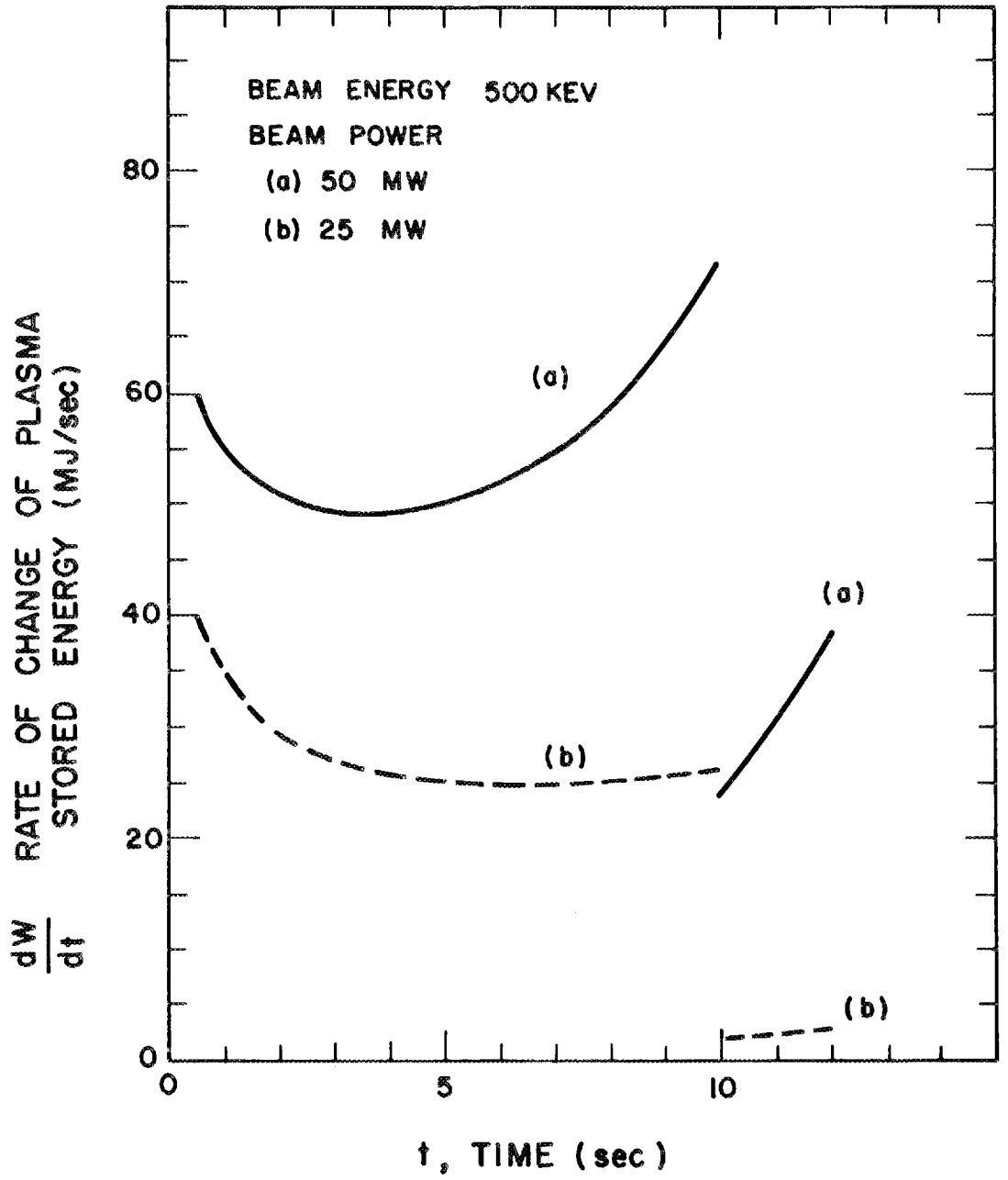
BEAM ENERGY 500 KEV
BEAM POWER
(a) 50 MW
(b) 25 MW
(a)
(b)
(a)
(b)
80
60
40
20
0
0
5
10
dW/dt RATE OF CHANGE OF PLASMA STORED ENERGY (MJ/sec)
t, TIME (sec)

Figure 31

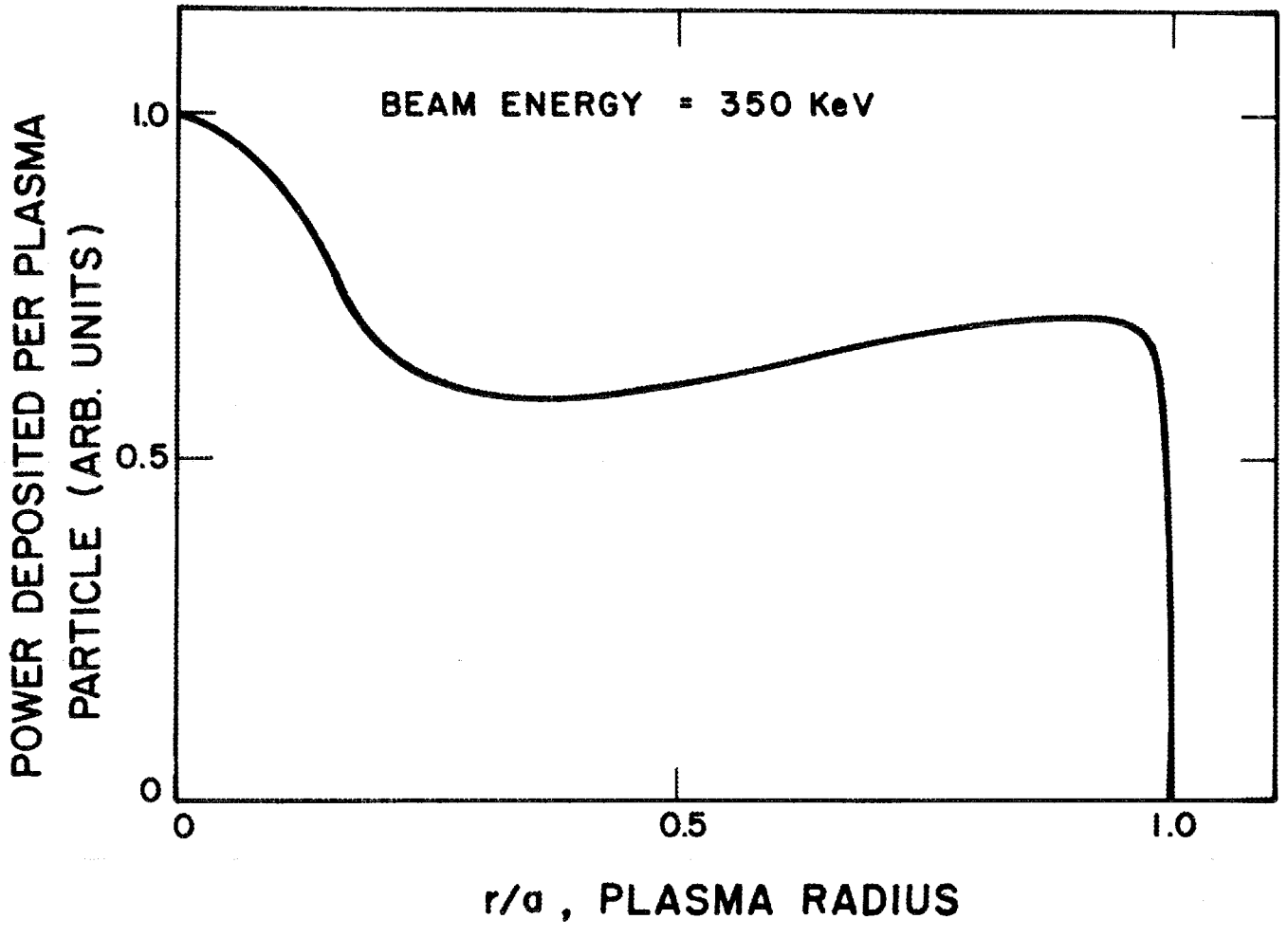
BEAM ENERGY = 350 KeV
POWER DEPOSITED PER PLASMA PARTICLE (ARB. UNITS)
1.0
0.5
0
0
0.5
1.0
r/a , PLASMA RADIUS

Figure 32

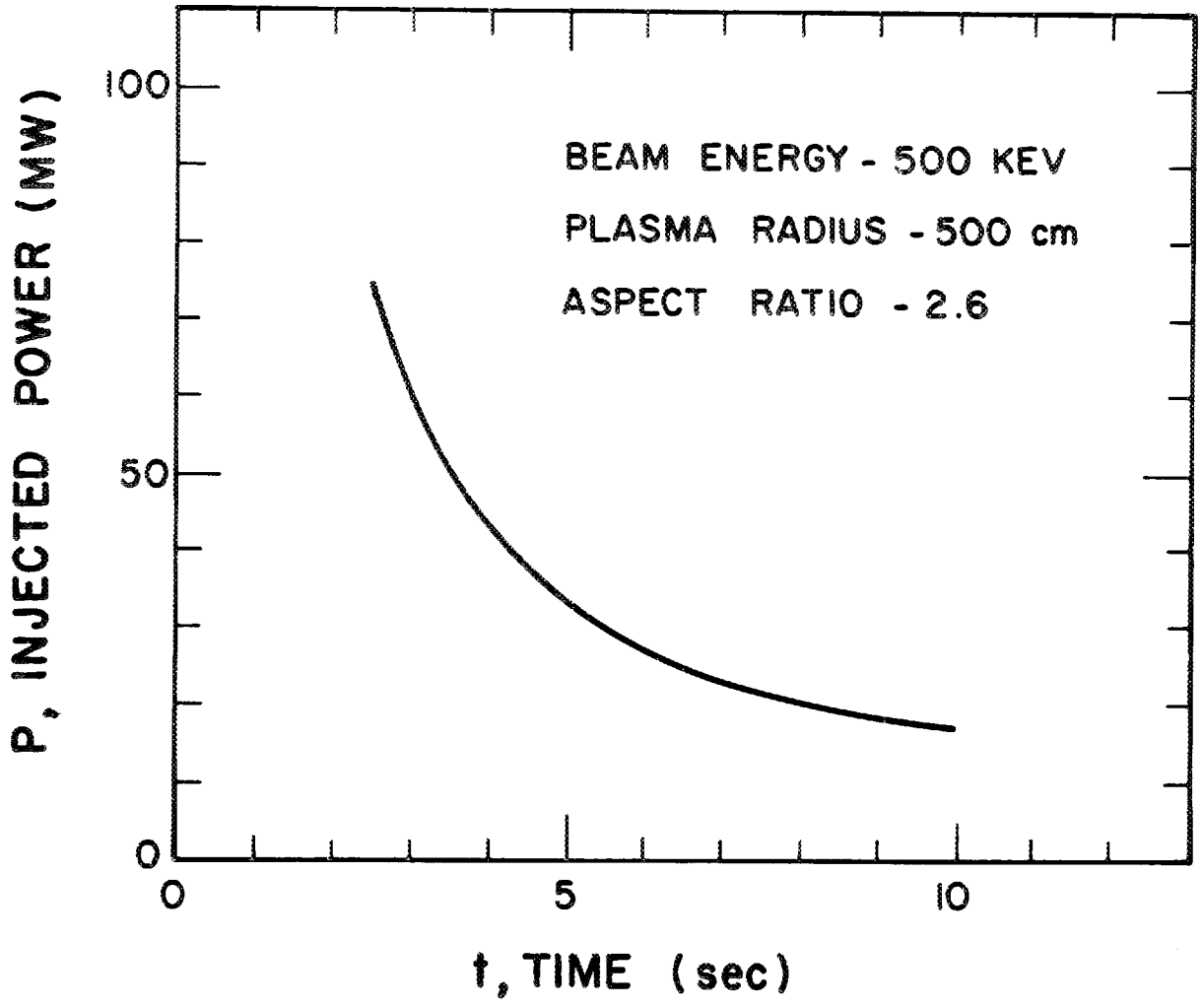
P, INJECTED POWER (MW)
100
50
0
0
5
10
t, TIME (sec)
BEAM ENERGY - 500 KEV
PLASMA RADIUS - 500 cm
ASPECT RATIO - 2.6

Figure 33

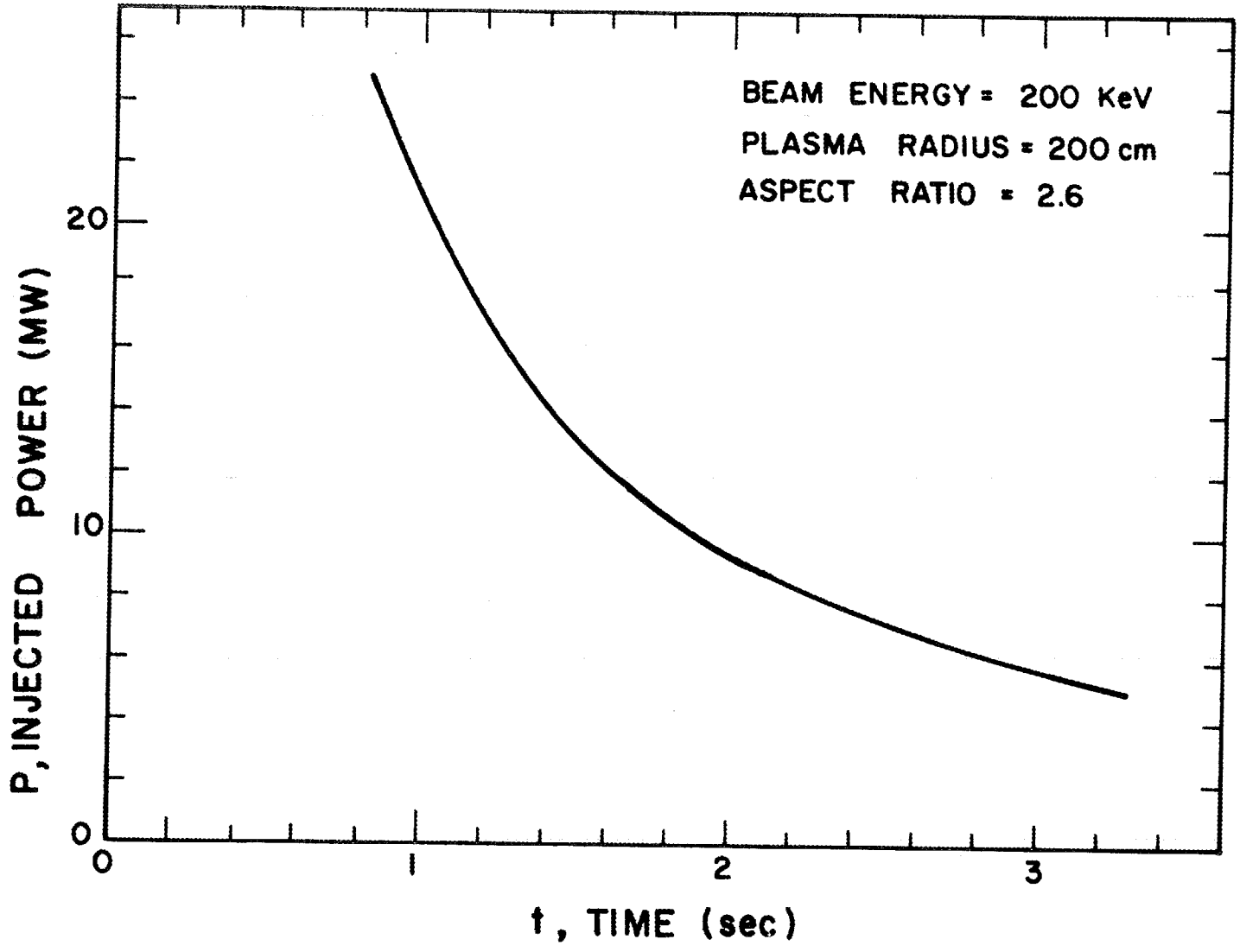
BEAM ENERGY = 200 KeV
PLASMA RADIUS = 200 cm
ASPECT RATIO = 2.6
P, INJECTED POWER (MW)
0
10
20
0
1
2
3
t, TIME (sec)

Figure 34

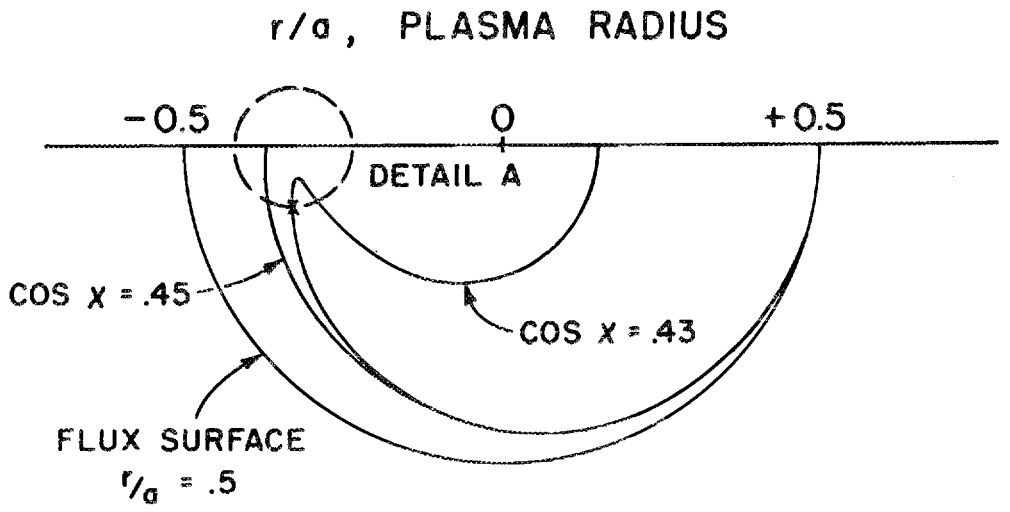
r/a, PLASMA RADIUS
-0.5
0
+0.5
DETAIL A
COS X = .45
COS X = .43
FLUX SURFACE
r/a = .5

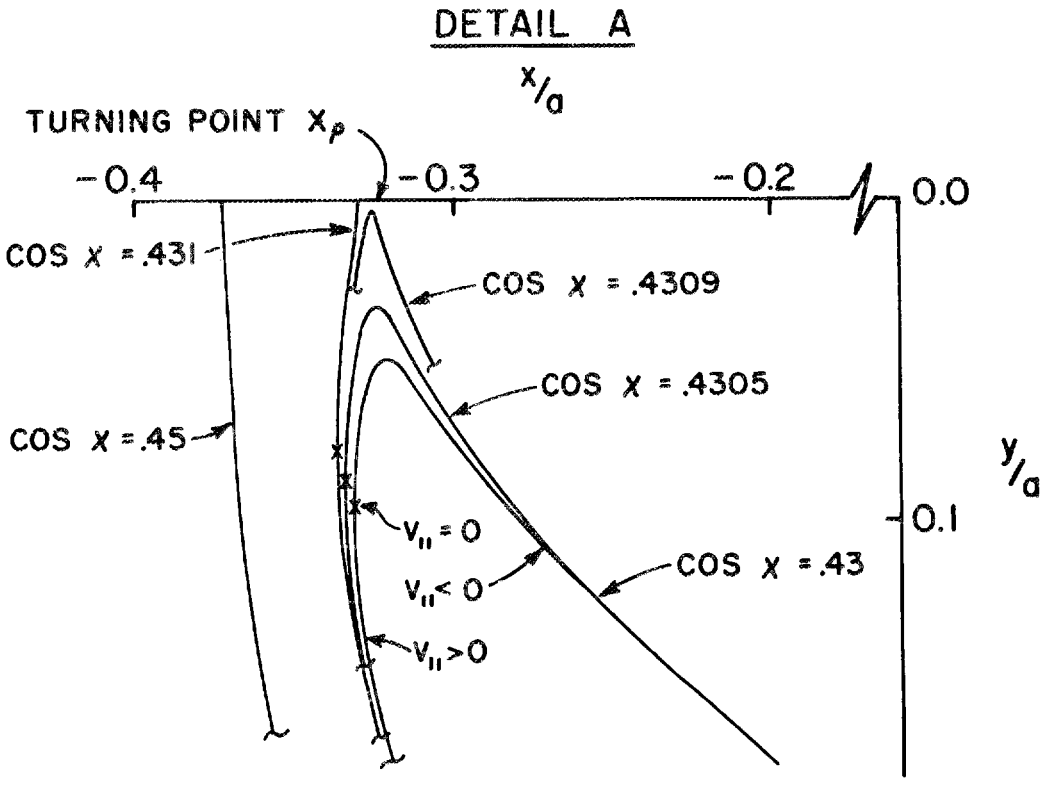
DETAIL A
x/a
TURNING POINT X_p
-0.4
-0.3
-0.2
0.0
COS X = .431
COS X = .4309
COS X = .4305
COS X = .45
$V_{\parallel} = 0$
$V_{\parallel} < 0$
$V_{\parallel} > 0$
COS X = .43
-0.1
y/a

Figure A-1

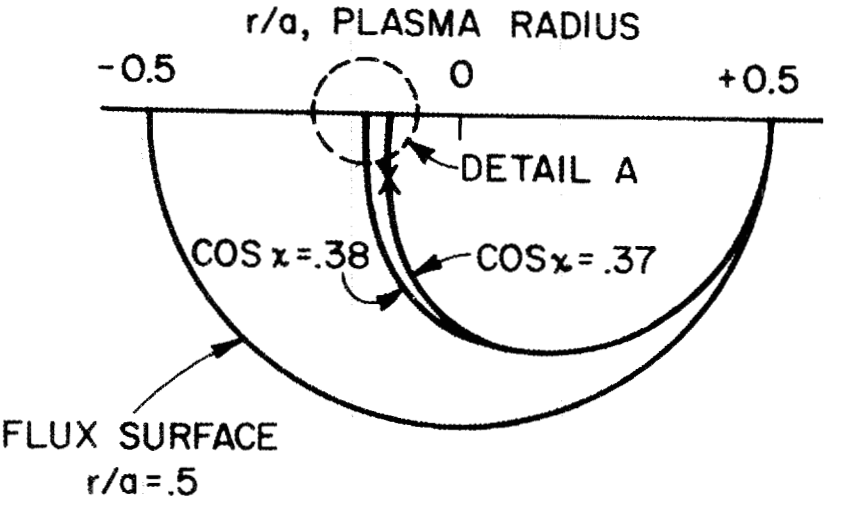
r/a, PLASMA RADIUS
-0.5
0
+0.5
DETAIL A
COS x = .38
COS x = .37
FLUX SURFACE
r/a = .5

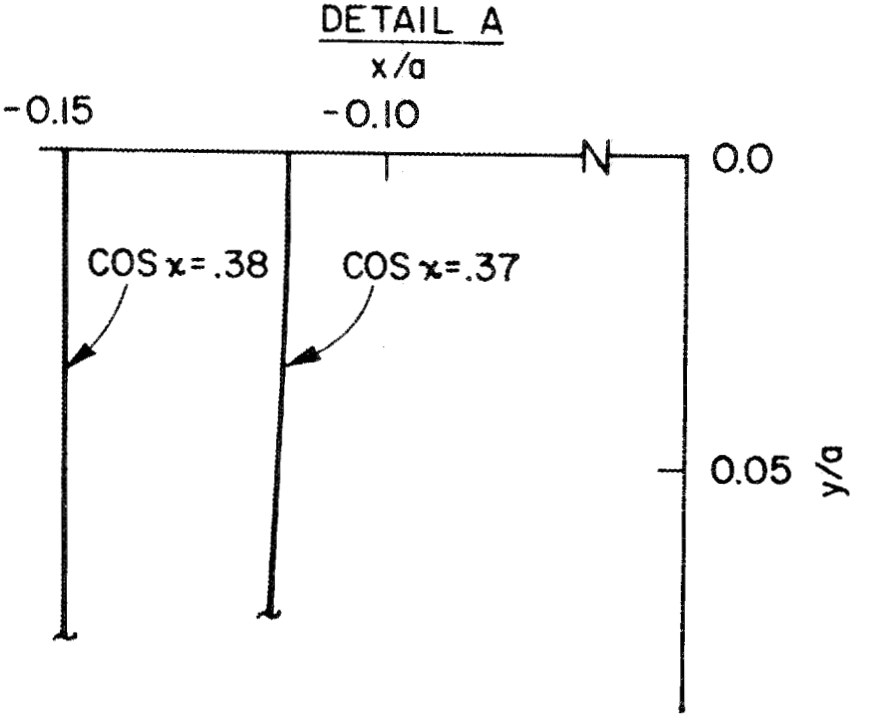
DETAIL A
x/a
-0.15
-0.10
0.0
COS x = .38
COS x = .37
0.05
y/a

Figure A-2